# Computational Study of Magnetic, Magnetoelectric and Electronic Properties of Some Quantum Many-Body Systems

A Thesis

Submitted for the Degree of

**Doctor of Philosophy**

In the Faculty of Science

by

**Abhiroop Lahiri**


Chemistry & Physics of Materials Unit

Jawaharlal Nehru Centre for Advanced Scientific Research,
Bangalore-560064

November 2020

*Dedicated to*

*my mentors*

*Anjan Kumar Lahiri,*

*Mandira Lahiri,*

*Udayaditya Bhattacharyya and*

*Partha Pratim Roy*

## DECLARATION

I hereby declare that the matter embodied in the thesis entitled "**Computational Study of Magnetic, Magnetoelectric and Electronic Properties of Some Quantum Many-Body Systems**" is the result of investigations carried out by me at the Chemistry and Physics of Materials Unit, Jawaharlal Nehru Centre for Advanced Scientific Research, Bangalore, India under the supervision of Prof. Swapan K. Pati and that it has not been submitted elsewhere for the award of any degree or diploma.

In keeping with the general practice in reporting scientific observations, due acknowledgement has been made whenever the work described is based on the findings of other investigators.

Abhiroop Lahiri

## CERTIFICATE

I hereby certify that the matter embodied in this thesis entitled "**Computational Study of Magnetic, Magnetoelectric and Electronic Properties of Some Quantum Many-Body Systems**" has been carried out by Mr. Abhiroop Lahiri at the Chemistry and Physics of Materials Unit, Jawaharlal Nehru Centre for Advanced Scientific Research, Bangalore, India under my supervision and that it has not been submitted elsewhere for the award of any degree or diploma.

Prof. Swapan K. Pati
(Research Supervisor)

# Acknowledgements

Very few people have achieved something in their life without the support of anyone. My father Dr. Anjan Kumar Lahiri and mother Mrs. Mandira Lahiri have been a tremendous source of support to me. They have always been there for me in every situation whatsoever, and encouraged me regardless of my emotions. They have helped me at every second to become what I am now.

I can't express in words how I am thankful to both the guide and the 'person' Prof. Swapan K. Pati. Not only has he guided me in my research, but also, he has always taken care of me like a parent even when I am 1200 miles away from my own parents. He has helped me to understand every concept and given me the courage to delve deep into the vast sea of Condensed Matter Physics. I also express my heartfelt thanks to Dr. Anusooya Pati who has cared for me like my mother.

I am very grateful to my course instructors besides my supervisor, namely, Prof. S. Balasubramanian, Prof. M. Eswaramoorthy , Prof. A. Sunderasan, Prof. K.S Narayan, Prof.N. Chandrabhas, Prof. Rajesh Ganapathy, Prof. Ranjan Datta, Prof. Tapas Maji, Prof. S. Rajaram , Prof. G.U. Kulkarni, Prof. S.M. Shivaprasad, Prof. U.V. Waghmare, Prof. Shobhana Narasimhan, Prof. Subir Das

Prof. Aloknath Chakrabarti (IISc) , Prof. Andal Narayanan (RRI) and Prof. Urbasi Sinha (RRI). The knowledge acquired from them has been my foundation for research. I sincerely thank all the CPMU and TSU faculty members who have not only guided me through the coursework but also helped shape my ideas.

I wish to thank Prof. C.N.R. Rao for providing the perfect place and ambience for research.

I am very thankful to Prof. Rajiv Singh for giving me an opportunity to work with him, at UC Davis and for our numerous fruitful discussions on several concepts and ideas.

I wish to thank my past and present labmates Dr. Pralok, Dr. Chaitanya, Dr. Somananda, Dr. Pallavi, Dr . Dibyajyoti, Dr. Bradraj, Dr. Swastika, Dr. Arkamita, Dr. Shubhajit, Dr. Madhuri, Dr. Siam, Dr.Navamani, Dr. Sandhya, Dr. Sylvia, Neha, Nisheal, Madhulika , Raju, Pallavi, Ashvini, Ganesh, Supriti, Bidhan, Anita, Dr. Paramita and Dr. Shazia and Arnab and for their company.

I wish to thank all the members of Complab, Academic Office and Admin Staff and Dhanwantari for catering to various needs.

It has been a really enjoyable stay in the Students Residence at JNCASR. The ambience is perfect. Several creative ideas have emerged during the morning tea an looking at the greenery from the balcony outside. I really cherish the frequent *addas* we had in the hostel. I thank Hostel Office and all the Housekeeping Staff for catering to our physical as well as aesthetic needs.

I thank my CPMU batchmates Nikita and Priyank for creating cherishable memories. I thank all the friends I made during my stay here - Aishwarya, Dibyashree, Srimayee, Arka, Rana, Sandip, Swaity, Mahan, Krishnendu, Sourav and many others with whom I have shared light-hearted moments. I wish to thank specially Madhulika and Shubhajit for being my partners in music which has always been the ‘oxygen’ for my survival. I am thankful to Sourjyadeep for being a great friend and ‘lockdown’ partner during our stay in the hostel at the time of

the COVID-19 pandemic.

I heartily thank Uday Mama for making me realize my slightest analytical skills, however small they may be. I express my gratitude to Mr. Partha Pratim Roy who has taught and motivated and inspired me at every moment in my journey of science till now.

I am indebted to my Guruji, Pandit Ajoy Chakraborty, for his constant guidance for 13 years and making music an integral part of my life, without which I could not have made the smallest achievement.

I acknowledge everyone who believed in me and egged me on to pursue my passion. It is surely a wonderful privilege to be a researcher of Condensed Matter Physics and I am grateful to be on this fascinating journey.

# Contents

# List of Figures

# 1 Introduction

Understanding the physics of interacting quantum many-body systems has gained immense attention in recent years as this governs the behavior of a huge variety of materials, such as, quantum magnetic materials, organic conductors[1] and charge transfer systems[2], multiferroics[3] and magnetoelectrics[4], conventional as well as high-$T_c$ superconductors[5], superfluids[6], Kondo lattices[7], Quantum Hall systems[8] and many more. Such strongly correlated materials have potential applications in a range of phenomena, from electronic, energy and memory devices to spin and quantum computing.

Systems in which electrons can wander almost freely, or, in other words, have a large kinetic energy with respect to the Coulomb interactions between them, can be dealt with the formalism of single particle quantum mechanics. However, interactions cannot always be neglected. For instance, in a class of f-electron systems, called *heavy fermion* systems,[9,10] in which the effective mass of the electrons are higher than their rest mass by several orders of magnitude. Thus, they are no longer freely moving individual electrons as electronic correlations become prominent. Still, many such interacting systems can be explained in the limits of *Fermi Liquid Theory*[11,12], in which the collective behaviour of such heavy electrons resemble that of non-interacting fermions with renormalized heavier masses.

However, there is a class of systems called, Mott insulators[13], which cannot be explained in the limits of Fermi liquid Theory, as the properties of those are solely determined by the relative strength of electronic correlations. Many of the exotic phenomena, like high $T_c$ superconductivity, charge and spin density waves, Umklapp processes[14] and charge and spin dynamics occur due to explicit electronic correlations.

Furthermore, when the dimension is reduced to 1D or quasi-1D, long-range correlations between electrons become stronger[15]. This makes it very difficult to solve the Schrödinger equation for these systems. Many such systems do not have a definite order in 1D. But these correlations are the key to all kinds of exotic phases[16,17], like, different types of spin-ordered patterns, fractional quantum Hall effects, superconducting and superfluid phases, etc. Moreover, due to the electronic correlations, systems may show the exotic many-body localized phase[18] which persists even at finite temperature.

With advances in experiments in recent years, cold atoms in optical lattices[19–21] have been an ideal experimental platform to visualize the different models proposed regarding interacting quantum many-body systems. Ultracold atoms are trapped in the electromagnetic fields of arrays of counter-propagating laser beams, thus mimicking a lattice. Such systems allow the tunability of every parameter by controlling the laser pulse widths, trapping depth, constructive and destructive interference, Feshbach resonance etc., thus making these systems very versatile.

To understand the physics of quantum many-body systems, different model Hamiltonians have been introduced. One of the first models was proposed by Warner Heisenberg in 1928[22] to understand the underlying mechanism of ferromagnets, in which, localized spins interact among each other to give a long range order. An exact solution for the ground state of the Heisenberg model was given by Hans Bethe using his famous ansatz[23]. After the prediction of Mott insulators by Sir Neville Mott in 1949, there have been several attempts to understand the

mechanism behind them. In 1962, the celebrated Hubbard model for interacting fermions was proposed by John Hubbard[24]. Soon after that, an exact solution for the 1-dimensional case was given by Lieb and Wu[25]. Since that time, the Hubbard Model has been an ideal model Hamiltonian to understand a variety of phenomena, like various correlated insulators to high-$T_c$ superconductivity. The Heisenberg model has been derived in the strong repulsion limit of the Hubbard model using second order degenerate perturbation theory. Subsequently different kinds of models have been proposed to understand the effects of electronic correlations in different systems.

The above mentioned models have been solved in different limits to explain different exotic phenomena. The XY model[26], for instance, which is derived from the Heisenberg model in the limit of negligible interaction between the z-component of the spins, has been successfully used to study topological phase transitions, such as the Berezinskii-Kosterlitz-Thouless[27] transition in 2D. Another example is the t-J model, derived from the Hubbard model, which has been used extensively to study the high-$T_c$ superconductivity.

Further generalizations have been introduced, by way of different models. The Majumdar-Ghosh model[28,29], for spin-$\frac{1}{2}$ systems is an extension of the Heisenberg model by adding next-nearest neighbour interactions. It gives a very clear visualization of a dimerized ground state. Thereafter, a model has been suggested by Affleck, Kennedy, Lieb and Tasaki[30] to understand topological order in the spin model systems. Many of these models have been solved exactly, either in some limits or in certain dimensions. Perturbative as well as mean field techniques also give a substantial information regarding the physical properties of these systems, but much needs to be explored in the non-perturbative limits an that is where the numerical methods come in.

## 1.1 Techniques for Effective Hamiltonian

The exact solution for a system of interacting particles is far from simple. There have been many approaches that can interpret weakly correlated systems, such as the Bloch band theory and *ab-initio* methods; but they fail to capture strong correlations. This is why, constructing a model Hamiltonian is necessary, which can capture the intricacies of the total Hamiltonian of an interacting system, however, on a smaller, less complex scale.

For a system of $N_e$ electrons and $N_n$ nuclei, the total Hamiltonian would look like :

$$\hat{H} = \hat{T_e}(r) + \hat{T_N}(R) + \hat{V_{ext}}(r, R) + \hat{V_{ee}}(r) + \hat{V_{NN}}(R) \tag{1.1}$$

Expanding which we have,

$$\hat{H} = -\frac{\hbar^2}{2}\sum_{i=1}^{N_e}\frac{\nabla_i^2}{m} - \frac{\hbar^2}{2}\sum_{I=1}^{N_n}\frac{\nabla_I^2}{M_I} - \sum_{i=1}^{N_e}\sum_{I=1}^{N_n}\frac{Z_I e^2}{|r_i - R_I|} + \sum_{i=1}^{N_e}\sum_{j>1}^{N_e}\frac{e^2}{|r_i - r_j|} + \sum_{I=1}^{N_n}\sum_{J>1}^{N_n}\frac{Z_I Z_J e^2}{|R_I - R_J|} \tag{1.2}$$

where, $\hbar$ is the Planck's constant, $m$ and $M$ are the masses of electrons and nuclei respectively, $\nabla_i^2$ and $\nabla_I^2$ are the Laplacians of the coordinates of the $i^{th}$ electron and $I^{th}$ nucleus. $Z_I$ and $Z_J$ are the atomic numbers of the $I^{th}$ and $J^{th}$ nuclei. $r_i$ and $R_I$ are the spatial coordinates of the $i^{th}$ electron and $I^{th}$ nucleus. $r_j$ and $R_J$ are the spatial coordinates of the $j^{th}$ electron and $J^{th}$ nucleus. $e$ is the electronic charge.

The first two terms describe the kinetic energies of the electrons and nuclei respectively. The third term is the Coulomb attraction term between electrons and nuclei. The fourth and fifth terms describe inter-electron and inter-nuclear Coulomb repulsion respectively.

In practice, this amounts to a formidable task as one has to take into account all the electrons and nuclei involved and the inter-particle electrostatic interactions too, by means of different approaches. The Born-Oppenheimer Approximation disseminates the electronic and nuclear motions and further approximations like the Hartree theory, aims to solve Eq.1.2 by treating $H_e$ as a sum of single particle terms and considering a one-particle form for $V_{e-e}$, instead of its actual two particle nature.

i.e.

$$\Psi(R, r) = \prod_i \psi(r_i) \tag{1.3}$$

Each one particle Schrödinger's equation considers an effective potential that treats the interaction with the other electrons in a mean field approach.

This also paved the way for a celebrated method, Density Functional Theory[31,32], proposed by Walter Kohn and Pierre Hohenberg in the '60s. The Hohenberg-Kohn theorems map the ground state electronic wave function to the electronic density, so the density that minimizes the energy of the overall functional is basically the solution of the full Schrödinger's equation. Thus the problem of interacting electrons in a static external potential is reduced to a problem of non-interacting electrons moving in an *effective potential*. The Schrödinger's equation is now rewritten as

$$E[\rho] = \hat{F}[\rho] + \int dr V_{ext}(r)\rho(r) \tag{1.4}$$

where, $\rho$ is the electron density and $\hat{F}[\rho]$ is the universal functional of density. The second term, or, the effective potential includes the external potential and the effects of the Coulomb interactions between the electrons (exchange and correlation effects).

Despite the upside of this simplification, the form of exchange correlation functional in terms of electronic density is not exactly known, so in many cases DFT resorts to semi-empirical parameters to approximate out such effects[33]. This

creates loopholes, which can manifest into errors while predicting properties, particularly the excited state properties. However, DFT method is quite popular as it predicts and accurately accounts for many ground state properties of systems ranging from small molecular systems to various periodic crystals.

However, in this thesis, we have considered systems which are beyond the realm of density functional theory, as all the systems are designed for ultra-cold lattice model systems. It is thus necessary, to preserve the many-body nature of the Hamiltonian, and this is where the knowledge of second quantization is availed of. In second quantized notation, $H_e$ may be written as –

$$H_e = -\sum_{\alpha\beta ab\sigma} t^{L_a L_b}_{\mathbf{R}_\alpha \mathbf{R}_\beta} c^\dagger_{\mathbf{R}_\alpha L_a \sigma} c_{\mathbf{R}_\beta L_b \sigma} + \frac{1}{2} \sum_{\substack{\alpha\beta\gamma\delta \\ abcd \\ \sigma\sigma'}} V_{ee}(\mathbf{R}, L) c^\dagger_{\mathbf{R}_\alpha L_a \sigma} c^\dagger_{\mathbf{R}_\beta L_b \sigma'} c_{\mathbf{R}_\delta L_d \sigma'} c_{\mathbf{R}_\gamma L_c \sigma} \quad (1.5)$$

where the overlap integrals are given by

$$\begin{aligned} t^{L_a L_b}_{\mathbf{R}_\alpha \mathbf{R}_\beta} &= \int d\boldsymbol{r} \varphi *_{\mathbf{R}_\alpha L_a}(\boldsymbol{r}) \left\{ \frac{\hbar^2 \Delta}{2m} - v_{ext}(\boldsymbol{r}) \right\} \varphi_{\mathbf{R}_\alpha L_a}(\boldsymbol{r}) \\ V_{ee}(\mathbf{R}, L) &= \int d\boldsymbol{r} d\boldsymbol{r'} \varphi *_{\mathbf{R}_\alpha L_a \sigma} \varphi *_{\mathbf{R}_\alpha L_a \sigma'}(\boldsymbol{r'}) \frac{e^2}{\boldsymbol{r} - \boldsymbol{r'}} \varphi_{\mathbf{R}_\gamma L_c \sigma'} \varphi_{\mathbf{R}_\delta L_d \sigma} \end{aligned} \quad (1.6)$$

Here $c^\dagger$ and $c$ are the creation and annihilation operators respectively, which are represented in terms of localized Wannier basis functions $\varphi(\boldsymbol{r})$. $L$ is the orbital index and $\sigma$ is the spin projection ($\uparrow$ or $\downarrow$). Generally, in $d$ or $f$ electronic systems, the Coulomb repulsion is the strongest when two electrons are in the same localized Wannier orbital. Thus, to understand the many-body behaviour of such systems, the Hubbard model was proposed, in which $V(\boldsymbol{R}, \boldsymbol{R}, \boldsymbol{R}, \boldsymbol{R}) = U$. Also, the overlap integral is uniform over all sites and only the nearest-neighbor overlap or 'hopping'

is prominent. Thus, the Hubbard model is given by

$$H = \underbrace{-t \sum_{\langle ij \rangle, \sigma} \left( c^{\dagger}_{i\sigma} c_{j\sigma} + h.c. \right)}_{\hat{T}} + U \sum_{i} n_{i\uparrow} n_{i\downarrow} \tag{1.7}$$

The Heisenberg model can be obtained from the Hubbard model at half-filling in the limit of strong onsite Coulomb repulsion. In second order degenerate perturbation theory, the energy correction is given by

$$E^{(2)} = -\sum_{m,n} \frac{\langle m|\hat{T}|n\rangle\langle n|\hat{T}|m\rangle}{E_m - E_n} \tag{1.8}$$

To obtain an appropriate model, we consider two lattice sites and obtain the Hamiltonian operator, which can be written in terms of perturbation theory, as the square of the kinetic energy operator $\hat{T}^2$(see Eq. 4.4). In the limit for strong onsite repulsion $U \gg t$, the hopping term (the kinetic energy term in 2nd quantized lattice model) can be chosen as perturbation. In this limit, there are four possible states, $|\uparrow,\uparrow\rangle$, $|\uparrow,\downarrow\rangle$ , $|\downarrow,\uparrow\rangle$ and $|\downarrow,\downarrow\rangle$, each of which is a ground state of the Hubbard term $U \sum_{i} n_{i\uparrow} n_{i\downarrow}$ with same zero energy. The numerator of the $2^{\text{nd}}$ order perturbed energy term can be written as

$$E^{(2)} = -\frac{t^2}{U} \sum_{e} \langle g| \sum_{\sigma} (c^{\dagger}_{1\sigma} c_{2\sigma} + c^{\dagger}_{2\sigma} c_{1\sigma}) |e\rangle\langle e| \sum_{\sigma'} (c^{\dagger}_{1\sigma'} c_{2\sigma'} + c^{\dagger}_{2\sigma'} c_{1\sigma'}) |g\rangle \tag{1.9}$$

As can be seen, there are two exited states, namely, $|0,\uparrow\downarrow\rangle$ and $|\uparrow\downarrow,0\rangle$. The $U$ term in the denominator comes because the transition of any state from ground state to the excited states (whichever is allowed) costs an energy, $U$, i.e. $E_e - E_g = U$.

Considering only the operator, we get

$$\begin{aligned}\mathcal{H}^{(2)} &= -\frac{t^2}{U}\sum_{\sigma,\sigma'}(c^\dagger_{1\sigma}c_{2\sigma}+c^\dagger_{2\sigma}c_{1\sigma})(c^\dagger_{1\sigma'}c_{2\sigma'}+c^\dagger_{2\sigma'}c_{1\sigma'}) \\ &= -\frac{t^2}{U}\sum_{\sigma,\sigma'}\left(c^\dagger_{1\sigma}c_{2\sigma}c^\dagger_{1\sigma'}c_{2\sigma'}+c^\dagger_{2\sigma}c_{1\sigma}c^\dagger_{2\sigma'}c_{1\sigma'}+c^\dagger_{1\sigma}c_{2\sigma}c^\dagger_{2\sigma'}c_{1\sigma'}+c^\dagger_{2\sigma}c_{1\sigma}c^\dagger_{1\sigma'}c_{2\sigma'}\right)\end{aligned} \tag{1.10}$$

For $\sigma=\sigma'$, The first 2 terms become zero as can seen by taking the annihilation operators to the right. Also, we define $n_i = n_{i\uparrow}+n_{i\downarrow}$. Thus

$$\begin{aligned}\mathcal{H}^{(2)}_{\sigma=\sigma'} &= -\frac{t^2}{U}\left\{\sum_\sigma n_{1\sigma}(1-n_{2\sigma})+n_{2\sigma}(1-n_{1\sigma})\right\} \\ &= -\frac{t^2}{U}\left\{n_{1\uparrow}(1-n_{2\uparrow})+n_{2\uparrow}(1-n_{1\uparrow})+n_{1\downarrow}(1-n_{2\downarrow})+n_{2\downarrow}(1-n_{1\downarrow})\right\} \\ &= -\frac{t^2}{U}\left\{(n_{1\uparrow}+n_{2\uparrow})+(n_{1\downarrow}+n_{2\downarrow})-(n_{1\uparrow}+n_{1\downarrow})(n_{2\uparrow}+n_{2\downarrow})-(n_{1\uparrow}-n_{1\downarrow})(n_{2\uparrow}-n_{2\downarrow})\right\} \\ &= -\frac{t^2}{U}\left(n_1+n_2-n_1n_2-4S^z_1S^z_2\right)\end{aligned} \tag{1.11}$$

where $S^z_i = \frac{1}{2}(n_{i\uparrow}-n_{i\downarrow})$

For $\sigma\neq\sigma'$, the terms would be

$$\begin{aligned}\mathcal{H}^{(2)}_{\sigma\neq\sigma'} &= -\frac{2t^2}{U}(c^\dagger_{1\uparrow}c_{2\uparrow}+c^\dagger_{2\uparrow}c_{1\uparrow})(c^\dagger_{1\downarrow}c_{2\downarrow}+c^\dagger_{2\downarrow}c_{1\downarrow}) \\ &= -\frac{2t^2}{U}(c^\dagger_{1\uparrow}c_{2\uparrow}c^\dagger_{1\downarrow}c_{2\downarrow}+c^\dagger_{2\uparrow}c_{1\uparrow}c^\dagger_{2\downarrow}c_{1\downarrow}+c^\dagger_{1\uparrow}c_{2\uparrow}c^\dagger_{2\downarrow}c_{1\downarrow}+c^\dagger_{2\uparrow}c_{1\uparrow}c^\dagger_{1\downarrow}c_{2\downarrow})\end{aligned} \tag{1.12}$$

The first 2 terms would be zero, because, the states on which they would act on, are singly occupied eigenstates of Hubbard Hamiltonian. So these two terms annihilate two fermions from one site and create two fermions on the other, which cannot be the case. Thus, rearranging the operators of the remaining terms, we

obtain

$$\begin{aligned}\mathcal{H}^{(2)}_{\sigma\neq\sigma'} &= -2(c^{\dagger}_{1\uparrow}c_{2\uparrow}c^{\dagger}_{2\downarrow}c_{1\downarrow} + c^{\dagger}_{2\uparrow}c_{1\uparrow}c^{\dagger}_{1\downarrow}c_{2\downarrow}) \\ &= -2(-c^{\dagger}_{1\uparrow}c_{1\downarrow}c^{\dagger}_{2\downarrow}c_{2\uparrow} - c^{\dagger}_{1\downarrow}c_{1\uparrow}c^{\dagger}_{2\uparrow}c_{2\downarrow}) \\ &= -2(S^{+}_{1}S^{-}_{2} + S^{-}_{1}S^{+}_{2}) \end{aligned} \tag{1.13}$$

where $S^{+}_{i} = \frac{1}{2}c^{\dagger}_{i\uparrow}c_{i\downarrow}$ and $S^{-}_{i} = \frac{1}{2}c^{\dagger}_{i\downarrow}c_{i\uparrow}$ Hence the total Hamiltonian from perturbation would be

$$\begin{aligned}\mathcal{H}^{(2)} &= -\left(\mathcal{H}^{(2)}_{\sigma=\sigma'} + \mathcal{H}^{(2)}_{\sigma\neq\sigma'}\right) \\ &= -\frac{t^2}{U}\left(n_1 + n_2 - n_1 n_2\right) + \frac{4t^2}{U}\left\{S^{z}_{1}S^{z}_{2} + \frac{1}{2}\left(S^{+}_{1}S^{-}_{2} + S^{-}_{1}S^{+}_{2}\right)\right\}\end{aligned} \tag{1.14}$$

For a half-filled system, where there is only one electron at each site, we have $n_1 = n_2 = 1$. Thus the first term would just be a constant $\frac{t^2}{U}$ and we are left with the familiar Heisenberg Hamiltonian

$$\mathcal{H}^{(2)} = -\frac{t^2}{U} + J\left(\hat{\boldsymbol{S}}_{\boldsymbol{1}}.\hat{\boldsymbol{S}}_{\boldsymbol{2}}\right) \tag{1.15}$$

where $J = \frac{4t^2}{U}$.

## 1.2 Analytical Methods and their drawbacks

The Hubbard and the Heisenberg models have exactly been solved in one dimension using the Bethe *ansatz*. After inclusion of other types of interaction terms, only a few such Hamiltonians could be solved exactly, mostly in one dimension. Such exactly solvable models are termed as *integrable* models. There have been different approaches to study the ground state properties of models which do not have exact solutions. Mean field approaches have been used extensively. Though

the interactions are smeared out in this approach, the mean field theories have been able to qualitatively predict different phases and phase transitions in certain limits. Moreover, spin wave theory(explained in a later chapter) , which is a first order perturbative term over and above the mean field theory, has been a very popular tool to study the low energy properties of quantum ferromagnets and antiferromagnets. Renormalization group based approaches[34] have been applied to predict the nature of the phase transitions in a quantitative manner using critical exponents. Many body perturbation theory and quantum field theoretical approaches[35] have been able to predict many exotic phases. However, all of these methods have their various pros and cons. In fact, most of these approaches fail in the limit of strong interactions.

There have been analytical approaches to study the dynamics of quantum systems. For instance, Floquet theory[36–39] is a very good approach to understand quantum systems, in which the properties show a periodic nature with time. However, most of the interacting many-body systems are quantum chaotic[40] in nature, and thus, to understand the ground and excited state properties of these model lattice systems, various computational methods have been developed.

## 1.3 Computational Approaches

With the advancement of technology, computational approaches have gained a lot of popularity. Not only they have been able to predict the existing results obtained by the analytical techniques, but also they have provided a lot more information about the physics of the systems. For example, the formal treatment of the theory of many-body localization, namely using the level statistics and long time dynamics, could not have been possible without computational approaches.

There are quite a few computational methods for quantum many-body systems, namely, exact diagonlization, Quantum Monte Carlo[41], Density matrix Renormal-

ization Group Methods[42], Matrix Product States[43] and Dynamical Mean field theory[44], each of them having their own pros and cons. Exact diagonlization, for example, is the most accurate of them all, in which the whole Hilbert space (Fock space in lattice exact diagonalizaion method) is taken into account. For small systems, it can exactly predict the low-energy as well as high-energy properties. But, as the system size grows larger, the Hilbert (or Fock) space grows exponentially. For instance, if we take an interacting spin-$\frac{1}{2}$ system, the spin at each site can have 2 possibilities, "$\uparrow$" or "$\downarrow$", thus, for an $N$-site system, there can be $2^N$ possible configurations, which constitute the Hilbert Space (or the Fock Space, to be specific). So, for a cluster of 24 spins, we will have $(\sim)10^7 \times 10^7$ matrices to deal with, which is impossible to solve. For larger systems, the numbers become so huge that, even the fastest computers will take many years to process.

However, with extensive research, people have realized that the ground state comprises of only a very small portion of the Hilbert Space. This led to the development of methods by which, for a given Hamiltonian, the Hilbert space is truncated to a very small subspace such that the ground state as well as low energy properties can be predicted quite accurately.

However, one has to keep in mind that the development of methods should be aimed at deriving a non-perturbative treatment and the method needs to be variationally bound. As we will see in the thesis, we have developed methods and also studied systems using non-perturbative variational methods.

# References

[1] Kanoda, K., Kato, R., Ann., Rev. Cond. Mat. **2**, 167-188, (2011).

[2] Painelli, A., Terenziani, F. and Soos, Z. G. Theor. Chem. Acc. **117**, 915–931 (2007).

[3] Khomskii, D., Physics **2**, 20 (2009).

[4] Brockmann, M., Klümper, A. and Ohanyan, V., Phys. Rev. B, **87**, 054407 (2013).

[5] Dagotto, E., Rev Mod. Phys. **66**, 763-840 (1994).

[6] Leggett, A.J., Phys. Rev. B **66**, 3, 763-840 (1994).

[7] Tesanovic, Z. and Valls, O. T., Phys Rev. B **34**, 3 (1986).

[8] Laughlin, R., B., Phys. Rev. Lett. **50**, 18 (1983).

[9] Radousky, H.,B., *Magnetism in Heavy Fermion Systems*, World Scientific (2000).

[10] Amusia, M., Popov, K., Shaginyan, V. and Stephanovich, V. *Theory of Heavy-Fermion Compounds - Theory of Strongly Correlated Fermi-Systems*, Springer Series in Solid-State Sciences. 182. Springer (2015).

[11] Phillips, Philip, Advanced Solid State Physics. Perseus Books. p. 224 (2008).

[12] Bruus, H., and Flensberg, K., Many-Body Quantum Theory in Condensed Matter Physics - an Introduction, Oxford, 2004.

[13] Mott, N. F. Proc. Phys. Soc. A **62**, 416 (1949).

[14] Ashcroft, N. W and Mermin, N. D., "Solid State Physics", Holt Rinehart and Winston, New York (1976).

[15] Quintanilla, J., and Hooley, C., Phys. World **22**, (06) 32, (2009).

[16] Parkinson, J. B., and Farnell, D. J., *An Introduction to Quantum Spin Systems*, Springer Lecture Notes in Physics (2010).

[17] Affleck, I., J. Phys. Condens. Matt. **1**, 3047 (1989).

[18] Basko, D. M., Aleiner, I. L. and Altshuler, B. L., arXiv:cond-mat/0602510.

[19] Bloch, I., Dalibard, J. and Zwerger, W., Rev. Mod. Phys. **80**, 885–964 (2008).

[20] Lewenstein, M., Sanpera, A., Ahufinger, V., Damski, B., Sen(De), A., Sen, U., Adv. Phys. **56**, 243–379 (2007).

[21] Bloch, I., Dalibard, J., and Nascimbène, S., Nat. Phys. **8**, 267–276 (2012).

[22] Heisenberg., W., Zeit. Phys. **49**, 619-636 (1928). Jaksch, D., Zoller, P., Ann. Phys. **315**, 52–79 (2005).

[23] Bethe, H., Zeit. Phys. **71**, 205–226 (1931).

[24] Hubbard J. , Proc. R. Soc. Lond. A **276**, 238–257 (1963).

[25] Lieb, E. H. and Wu, F. Y., Phys. Rev. Lett **20**, 1445-1448 (1968).

[26] Lieb, E., Schultz, T., Mattis, D., Ann. of Phys., **16**, 407 (1961).

[27] Kosterlitz, J. M. and Thouless, D. J. , J. Phys. C: **6**, 7 (1972).

[28] Majumdar, C. K., and Ghosh, D., J. Math. Phys. **10**, 1388 (1969).

[29] Majumdar, C. K., J. Phys. C **3**, 911–915 (1970).

[30] Affleck, I., Kennedy, T., Lieb, E. H., and Tasaki, H., Phys. Rev. Lett. **59**, 799-802, (1987).

[31] Hohenberg, P. and Kohn, W., Phys. Rev. **136**, B864-B871 (1964).

[32] Kohn, W. and Sham, L. J., Phys, Rev. **140**, A1133-A1138 (1965).

[33] Cohen, A. J., Mori-Sanchez, P. and Yang, W., Science, **321**, 792-794 (2008).

[34] Salmhofer, M., Nucl. Phys. B **941**, 868-899 (2019).

[35] Rao, S., Sen, D., arXiv:cond-mat/0005492 (2000).

[36] Floquet, G., Ann. de l'Ecole Norm. Sup. 12, 47 (1883).

[37] Ince, E. L., Ordinary Diffential Equations (Dover Publ., New York, 1956).

[38] Magnus, W., and S. Winkler, S., Hill's Equation (Dover Publ., New York, 1979).

[39] Bukov, M., Kolodrubetz, M., and Polkovnikov, A., Phys. Rev. Lett. **116**, 125301 (2016).

[40] Blümel, R. and Smilansky, U, Phys. Rev. Lett. **69**, 3491–3494 (1992).

[41] Matuttis H. G. and Morgenstern I., Quantum Monte Carlo Investigations for the Hubbard Model. In: Hoffmann K. H., Schreiber M. (eds) Computational Physics. Springer, Berlin, Heidelberg (1996).

[42] White, S. R., Phys. Rev. Lett. **69**, 2863 (1992).

[43] Schollwöck, U., Ann. Phys., **326**, 96-192 (2011).

[44] Georges, A., Kotliar. G., Krauth, W., and Rozenberg, M.J., Rev. Mod. Phys. **68**, 13-125 (1996).

# 2

# Matrix Product state approach to static and time-dependent simulations for quantum many-body systems

## 2.1 Introduction

Matrix Product states (MPS) are an efficient representation of a quantum many-body system in one dimension[1]. Although the representation of a state in an arbitrary basis is exact, in practice, the state is truncated for computational convenience and thus are suitable to represent weakly entangled states. Originally MPS were discovered for analytical studies, until Ostlund and Romer[2] realized that the infinite system DMRG can be represented as a 'matrix' in the MPS formalism. Subsequently it was understood that finite-size DMRG is a variational energy optimization scheme in the MPS formalism[3,4]. Since then, MPS have been a very successful method as they can accurately represent ground state or low energy states of a quantum system, which are usually weakly entangled states. They can also predict many-body localized states[5], for which the entanglement entropy obeys the area law[6–8].

## 2.2 Decomposition of an arbitrary state to MPS

### 2.2.1 Singular Value Decomposition

Singular Value decomposition (SVD) is a technique which has always come in handy for quantum mechanical simulations. It is the basis of decomposition of any quantum state to an MPS. It is also used to approximate each such matrix by a matrix of lower rank, specific to weakly entangled quantum states [9,10], thus reducing memory and computational cost. We illustrate it below.

Consider any general matrix $A$ with dimension $M \times N$. It can be decomposed as

$$A = USV^{\dagger} \tag{2.1}$$

where $U$ and $V$ are unitary matrices of dimensions $M \times \min(M,N)$ and $\min(M,N) \times N$ respectively, i.e. $UU^{\dagger} = \mathbb{1}$ and $VV^{\dagger} = \mathbb{1}$(Fig.2.1a). $S$ is a diagonal matrix of the singular values having dimensions $\{\min(M,N) \times \min(M,N)\}$. The matrix is truncated by taking the highest $R$ singular values ($R < \min(M,N)$) (Fig.2.1b). The reason for taking the highest ones is that, SVD of a bipartite quantum system is equivalent to *Schmidt Decomposition* and the singular values for such decomposition (or the Schmidt coefficients) happen to be the eigenvalues of the reduced density matrix for the system.

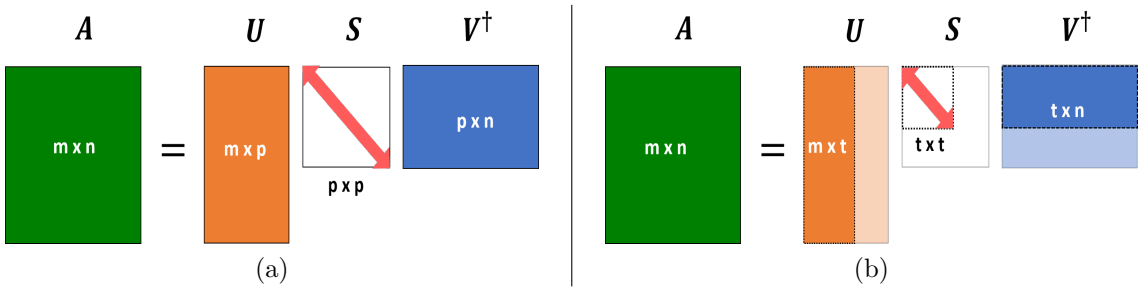


Figure 2.1: Pictorial representation of Singular value decomposition. (a) Full decomposition of the given matrix; $p$ being the number of singular values and (b) decomposition followed by truncation by keeping only $t(< p)$ number of singular values starting from the highest.

### 2.2.2 Construction of a Matrix Product State

Let us consider a 1-dimensional lattice of length $L$, each site having degrees of freedom $\{\sigma_i\}, i = 1, ..., L$. Each $\sigma_i$ has a local dimension $d_i$. A general state can be written as

$$|\Psi\rangle = \sum_{\sigma_1,...,\sigma_L} c_{\sigma_1,...,\sigma_L} |\sigma_1, ..., \sigma_L\rangle \tag{2.2}$$

As the length of the chain increases the Hilbert space of the configurations increases exponentially. In this case we can use the advantages of SVD truncation as well as obtain a local picture of the state, convenient for computation. We reshape the set of coefficients $c_{\sigma_1,...,\sigma_L}$ into a matrix by putting $\sigma_1$ apart and the taking rest $\sigma_i$s together :

$$\begin{aligned} c_{\sigma_1,...,\sigma_L} &= c_{\sigma_1,(\sigma_2...,\sigma_L)} \\ &= \sum_{a_1} M^1_{\sigma_1,a_1} S_{a_1,a_1} V^\dagger_{a_1,(\sigma_2...,\sigma_L)} \\ &= \sum_{a_1} M^1_{\sigma_1,a_1} c'_{a_1,\sigma_2...,\sigma_L} \end{aligned} \tag{2.3}$$

In the last step the index $(\sigma_2..., \sigma_L)$ is reshaped back and hence the parentheses are dropped.

We perform a similar scheme of SVD for the $c'_{a_1,\sigma_2...,\sigma_L}$ and thus get a $c''$. We keep on doing this :

$$
\begin{aligned}
c_{\sigma_1,\ldots,\sigma_L} &= \sum_{a_1} M^1_{\sigma_1,a_1} c'_{(a_1,\sigma_2),(\sigma_3\ldots,\sigma_L)} \\
&= \sum_{a_1} M^1_{\sigma_1,a_1} \sum_{a_2} M^2_{(a_1,\sigma_2),a_2} S'_{a_2,a_2} V'^{\dagger}_{a_2,(\sigma_3\ldots,\sigma_L)} \\
&= \sum_{a_1,a_2} M^1_{\sigma_1,a_1} M^2_{(a_1,\sigma_2),a_2} c''_{a_2,\sigma_3\ldots,\sigma_L} \\
&= \sum_{a_1,a_2} M^1_{\sigma_1,a_1} M^2_{(a_1,\sigma_2),a_2} \sum_{a_3} M^3_{(a_2,\sigma_3),a_3} S''_{a_3,a_3} V''^{\dagger}_{a_3,(\sigma_4\ldots,\sigma_L)} \\
&\vdots \\
&= \sum_{a_1,\ldots,a_L} M^1_{\sigma_1,a_1} M^2_{(a_1,\sigma_2),a_2} M^3_{(a_2,\sigma_3),a_3} \ldots M^{L-1}_{(a_{L-2},\sigma_{L-1}),a_L} M^L_{\sigma_L,a_L} \\
&= \sum_{a_1,\ldots,a_L} M^{\sigma_1}_{a_1} M^{\sigma_2}_{a_1,a_2} M^{\sigma_3}_{a_2,a_3} \ldots M^{\sigma_{L-1}}_{a_{L-1},a_L} M^{\sigma_L}_{a_L} \qquad (2.4)
\end{aligned}
$$

In the last step, brackets in the indices are dropped and the matrices are reshaped as rank-3 tensors. In a simplified form, we can write as

$$
c_{\sigma_1,\ldots,\sigma_L} = M^{\sigma_1} M^{\sigma_1} \ldots M^{\sigma_{L-1}} M^{\sigma_L} \qquad (2.5)
$$

In this way, we have decomposed a many-body wave function into a MPS. The dimension of the index $\{a_i\}$ are the *bond dimensions* while $\{\sigma_i\}$ are physical dimensions of the MPS. As we have decomposed from the left, such an MPS is termed as a *left canonical* MPS.

## 2.3 Tensor Network Diagrams

### 2.3.1 Pictorial Representation of Tensors

Since MPS comprise of rank-3 tensors, it can be called a *tensor network* in one dimension. These can be graphically represented by nice diagrams, making it easy for us to visualize. A tensor of rank-1, (which is a just a vector) can be represented by a square (or any shape) with one leg, denoting its index, as shown in Fig 2.2a. Similarly tensors of rank 2 and 3 can be denoted by squares with 2 and 3 legs respectively. Thus a general $n^{th}$ rank tensor is a square with $n$ legs, each leg corresponding to 1 tensor index.

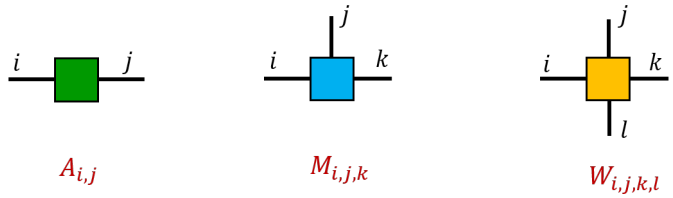


(a)

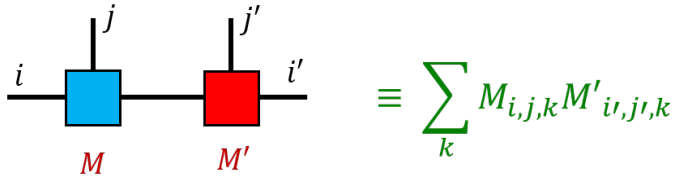


(b)

Figure 2.2: Pictorial representations of (a) rank-2, rank-3 and rank-4 tensors, and (b) contraction of a single index of two tensors

### 2.3.2 Tensor Contraction and Tensor Networks

The tensor contraction of one index of two tensors, say rank-3, is graphically represented by joining one leg each. So, for two tensors $M^{\sigma_1}_{i_1 j_1}$ and $M^{\sigma_2}_{i_2 j_2}$ with

$j_1 = j_2$ the contraction $A = \sum_{j_1} M^{\sigma_1}_{i_1 j_1 k_1} M^{\sigma 2}_{i_2 j_1 k_2}$ is represented by Fig 2.2b. If we have $L$ number of such tensors, and we contract one leg of each tensor with the next one, we get a *tensor network*. An MPS is such a tensor network .

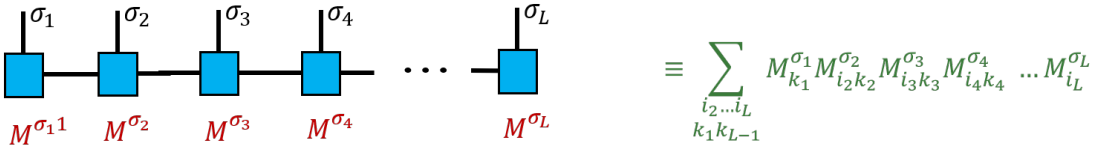


Figure 2.3: Pictorial representation of a 1D tensor network or a Matrix Product State.

## 2.4 Left, right and mixed canonical MPS

Previously, in Sec. 2.2.2 we have started the decomposition from the leftmost site index. But we can also begin from the rightmost index in the following way:

$$
\begin{aligned}
c_{\sigma_1,\ldots,\sigma_L} &= c_{(\sigma_1\ldots,\sigma_{L-1}),\sigma_L} \\
&= \sum_{a_L} A_{(\sigma_1\ldots,\sigma_{L-1}),a_L} S_{a_L,a_L} V^{\dagger}_{a_L,\sigma_L} \\
&= \sum_{a_L} c'_{\sigma_1\ldots,\sigma_{L-1},a_L} N^1_{a_L,\sigma_L} \\
&\vdots \\
&= \sum_{a_1,\ldots,a_L} N^1_{\sigma_1,a_1} N^2_{(a_1,\sigma_2),a_2} \ldots N^{L-1}_{(a_{L-2},\sigma_{L-1}),a_L} N^L_{\sigma_L,a_L} \\
&= \sum_{a_1,\ldots,a_L} N^{\sigma_1}_{a_1} N^{\sigma_2}_{a_1,a_2} \ldots N^{\sigma_{L-1}}_{a_{L-1},a_L} N^{\sigma_L}_{a_L} \qquad (2.6)
\end{aligned}
$$

with $V^{\dagger}_{a_L,\sigma_L} = N^1_{a_L,\sigma_L}$ in the 3$^{\text{rd}}$ step. Thus we create a *right canonical* MPS.

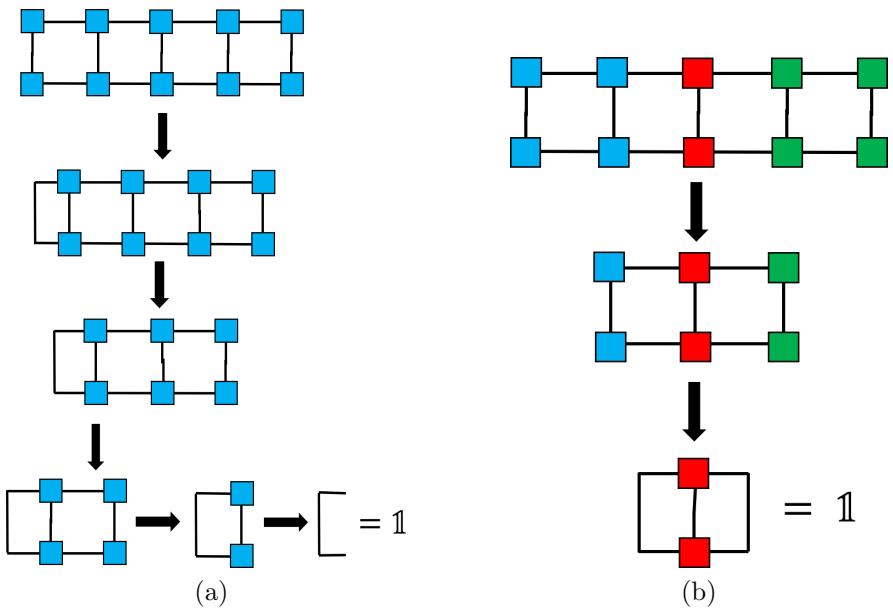


Figure 2.4: Tensor-network diagram for the normalization of (a) a left-canonical MPS and (b) a mixed-canonical MPS, by sequential tensor contractions.

We can also choose any arbitrary site and decompose all the sites on the left of that site to be left canonical and all those on the right to be right canonical. This is diagrammatically represented in Fig. 2.4a

Such a MPS is called a *mixed canonical* MPS. Thus we can write,

$$c_{\sigma_1,\ldots,\sigma_L} = \sum_{a_1,\ldots,a_L} M^{\sigma_1}_{a_1} M^{\sigma_2}_{a_1,a_2} \ldots M^{\sigma_{i-1}}_{a_{i-1},a_i} S_{a_i,a_i} N^{\sigma_{i+1}}_{a_i,a_{i+1}} \ldots N^{\sigma_{L-1}}_{a_{L-1},a_L} N^{\sigma_L}_{a_L} \tag{2.7}$$

Here the $i^{\text{th}}$ site is the *orthogonality center*. the corresponding diagram is shown in Fig.2.4b This representation is used most often, as it helps to reduce computational cost when calculating expectation values of local operators and short range correlations.

## 2.5 Matrix Product Operators

Analogous to the MPS, we can write any Hamiltonian as a product of tensors corresponding to each site of the system. Each of them are rank-4 tensors and the their contraction is called a *Matrix Product Operator*(MPO).
Any general operator can be written as

$$\hat{O} = \sum_{\substack{\sigma_1,...,\sigma_L,\\ \sigma'_1,...,\sigma'_L}} w_{\sigma_1,...,\sigma_L,\sigma'_1,...,\sigma'_L} |\sigma_1, ..., \sigma_L\rangle\langle\sigma'_1, ..., \sigma'_L| \tag{2.8}$$

The coefficients $w_{\sigma_1,...,\sigma_L,\sigma'_1,...,\sigma'_L}$ can be written in MPO form as

$$w_{\sigma_1,...,\sigma_L,\sigma'_1,...,\sigma'_L} = \sum_{a_1,...,a_L} W^{\sigma_1,\sigma'_1}_{a_1} W^{\sigma_2,\sigma'_2}_{a_1,a_2} \dots W^{\sigma_{L-1}\sigma'_{L-1}}_{a_{L-1},a_L} W^{\sigma_L\sigma'_L}_{a_L} \tag{2.9}$$

In this case, the $W^{\sigma_i,\sigma'_i}$s are rank-4 tensors. The corresponding tensor network diagram is shown in Fig.2.5.

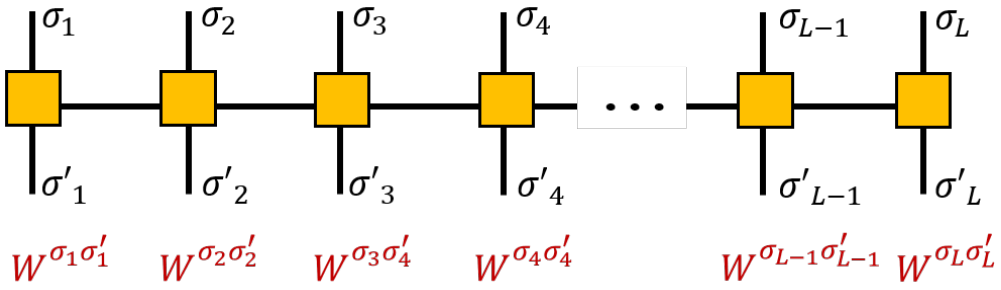


Figure 2.5: Tensor Network Diagram of a Matrix Product Operator (MPO).

### 2.5.1 Creating a Matrix Product Operator

There are different ways to create an MPO[1,11,12]. For the $i^{th}$ site, the Hamiltonian $\mathcal{H}$ is split into a left block $H^L_{i-1}$, a right block $H^R_{i+1}$, a tensor product of terms $h^L_{j,a_j}$

and $h^R_{j,a_j}$ connecting these blocks

$$\mathcal{H} = H^L_{i-1} \otimes \mathbb{1}^R_i + \mathbb{1}^L_i \otimes H^R_{i+1} + \sum_{a_i} h^L_{i,a_i} + h^R_{i,a_i} \tag{2.10}$$

The decomposition for the bonds $i$ and $i-1$ follow a recursion relation, represented in terms of a auxiliary operator-valued matrix at the site $i$

$$\begin{pmatrix} H^R_{i+1} \\ h^R_{i-1,a_{i-1}} \\ \mathbb{1}^R_{i-1} \end{pmatrix} = \begin{array}{c} \\ 1 \\ N_{i-1} \\ 1 \end{array} \overbrace{\begin{array}{c} \begin{array}{ccc} 1 & N_i & 1 \end{array} \\ \begin{pmatrix} \mathbb{1}_i & \hat{C}_i & \hat{D}_i \\ 0 & \hat{A}_i & \hat{B}_i \\ 0 & 0 & \mathbb{1}_i \end{pmatrix} \end{array}}^{\boldsymbol{W}^i} \bigotimes \begin{pmatrix} H^R_i \\ h^R_{i,a_i} \\ \mathbb{1}^R_i \end{pmatrix} \tag{2.11}$$

where $\hat{A}_i$, $\hat{B}_i$, $\hat{C}_i$, $\hat{D}_i$ are matrices of operators acting on the site $i$. $\hat{C}_i$ and $\hat{B}_i$ correspond to the nearest-neighbor interactions. $\hat{D}_i$ is comprised by onsite interactions and $\hat{A}_i$ contains the next or further neighbor interactions. For instance, let us consider the nearest-neighbor Heisenberg model

$$\mathcal{H}_{NN} = \sum_i \hat{S}^z_i \hat{S}^z_{i+1} + \frac{1}{2}\left(\hat{S}^+_i \hat{S}^-_{i+1} + \hat{S}^-_i \hat{S}^+_{i+1}\right) \tag{2.12}$$

The operator valued matrix for the $i_{th}$ site is

$$W^{\sigma_i \sigma'_i} = \begin{pmatrix} \mathbb{1} & \hat{S}^+_i & \hat{S}^-_i & \hat{S}^z_i & -h\hat{S}^z_i \\ 0 & 0 & 0 & 0 & \frac{J}{2}\hat{S}^-_i \\ 0 & 0 & 0 & 0 & \frac{J}{2}\hat{S}^+_i \\ 0 & 0 & 0 & 0 & J\hat{S}^z_i \\ 0 & 0 & 0 & 0 & \mathbb{1} \end{pmatrix} \tag{2.13}$$

Thus here, $\hat{C}_i = \begin{pmatrix} \hat{S}_i^+ & \hat{S}_i^- & \hat{S}_i^z \end{pmatrix}$, $\hat{B}_i = \begin{pmatrix} \frac{J}{2}\hat{S}_i^- & \frac{J}{2}\hat{S}_i^+ & J\hat{S}_i^z \end{pmatrix}^T$ and $\hat{D}_i = -h\hat{S}_i^z$ and $\hat{A}_i = 0_{3\times 3}$. $\hat{A}_i$ has non-zero elements when next or higher neighbour interactions are present. For a finite size chain, the tensors for first and last sites would be a row and a column vector respectively.

$$W^{\sigma_1\sigma_1'} = \begin{pmatrix} \mathbb{1} & \hat{S}_1^+ & \hat{S}_1^- & \hat{S}_1^z & -h\hat{S}_1^z \end{pmatrix}, \qquad W^{\sigma_L\sigma_L'} = \begin{pmatrix} -h\hat{S}_L^z \\ \frac{J}{2}\hat{S}_L^- \\ \frac{J}{2}\hat{S}_L^+ \\ J\hat{S}_L^z \\ \mathbb{1} \end{pmatrix} \tag{2.14}$$

This makes the total Hamiltonian scalar. For the next-neighbor Hamiltonian

$$\mathcal{H}_{NNN} = \mathcal{H}_{NN} + \sum_i \hat{S}_i^z \hat{S}_{i+2}^z + \frac{1}{2}\left(\hat{S}_i^+ \hat{S}_{i+2}^- + \hat{S}_i^- \hat{S}_{i+2}^+\right) \tag{2.15}$$

The MPO can be written as

$$W^{\sigma_i,\sigma_i'} = \begin{pmatrix} \mathbb{1} & \hat{S}_i^+ & \hat{S}_i^- & \hat{S}_i^z & 0 & 0 & 0 & -h\hat{S}_i^z \\ 0 & 0 & 0 & 0 & \mathbb{1} & 0 & 0 & \frac{J}{2}\hat{S}_i^- \\ 0 & 0 & 0 & 0 & 0 & \mathbb{1} & 0 & \frac{J}{2}\hat{S}_i^+ \\ 0 & 0 & 0 & 0 & 0 & 0 & \mathbb{1} & J\hat{S}_i^z \\ 0 & 0 & 0 & 0 & 0 & 0 & 0 & \frac{J'}{2}\hat{S}_i^- \\ 0 & 0 & 0 & 0 & 0 & 0 & 0 & \frac{J'}{2}\hat{S}_i^+ \\ 0 & 0 & 0 & 0 & 0 & 0 & 0 & J'\hat{S}_i^z \\ 0 & 0 & 0 & 0 & 0 & 0 & 0 & \mathbb{1} \end{pmatrix} \tag{2.16}$$

In this case three elements of $\hat{A}_i$ are non-zero.

## 2.6 Overlaps and Expectation Values

The overlap of two MPS $|\Psi_1\rangle = \boldsymbol{M}^{\sigma_1}\boldsymbol{M}^{\sigma_2}\dots\boldsymbol{M}^{\sigma_L}$ and $|\Psi_2\rangle = \tilde{\boldsymbol{M}}^{\sigma_1}\tilde{\boldsymbol{M}}^{\sigma_2}\dots\tilde{\boldsymbol{M}}^{\sigma_L}$ is represented as a tensor network diagram , shown in Fig.2.6. It involves a series of tensor contractions and can be algebraically expressed as

$$\langle\Psi_2|\Psi_1\rangle = \sum_{\sigma_L}\tilde{M}^{\sigma_L\dagger}\left(\dots\left(\sum_{\sigma_3}\tilde{M}^{\sigma_3\dagger}\left(\sum_{\sigma_2}\tilde{M}^{\sigma_2\dagger}\left(\sum_{\sigma_1}\tilde{M}^{\sigma_1\dagger}M^{\sigma_1}\right)M^{\sigma_2}\right)M^{\sigma_3}\right)\dots\right)M^{\sigma_L} \tag{2.17}$$

For the overlap of $|\Psi_1\rangle$ with itself, the $\tilde{M}^{\sigma_1}$ will be replaced by $M^{\sigma_1}$. In this case, for a MPS constructed by sequential SVD procedure (as described in section 2.2 the sum $\sum_{\sigma_1}\tilde{M}^{\sigma_i\dagger}M^{\sigma_i} = 1$ for each $i$, as $M^{\sigma_i}$ are unitary matrices. Therefore, the overlap $\langle\Psi_1|\Psi_1\rangle = 1$, i.e. it is already normalized. A similar diagram can be constructed for the energy expectation value $\langle\Psi|\mathcal{H}|\Psi\rangle$. For an operator $\hat{O}_i$ acting at the $i^{th}$ site, the expectation value can be written as

$$\langle\Psi_2|\hat{O}_i|\Psi_1\rangle = \sum_{\sigma_L}\tilde{M}^{\sigma_L\dagger}\left(\dots\left(\sum_{\sigma_i,\sigma_i'}\hat{O}^{\sigma_i,\sigma_i'}\tilde{M}^{\sigma_i\dagger}\left(\dots\left(\sum_{\sigma_1}\tilde{M}^{\sigma_1\dagger}M^{\sigma_1}\right)\dots\right)M^{\sigma_i'}\right)\dots\right)M^{\sigma_L} \tag{2.18}$$

where the operator is multiplied to the matrix at the $i^{th}$ site (marked in red).

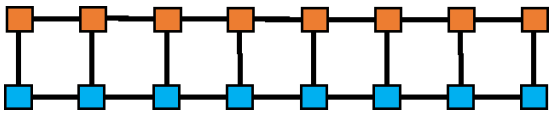

Figure 2.6: Tensor Network Diagram of the overlap between two MPS.

The diagram is shown in Fig.2.7a and the rest is just the overlap expression. Assuming that the MPS is right normalized on the right of the $i^{th}$ site and left

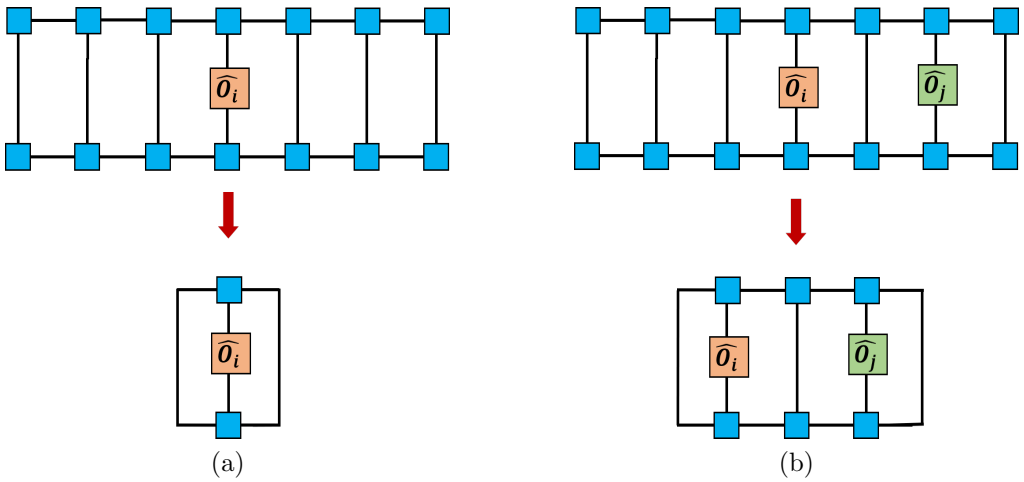


Figure 2.7: Tensor network diagram for (a) the expectation value of a single site operator $\langle \hat{O}^i \rangle$ and (b) two point correlation function. $\langle \hat{O}^i \hat{O}^j \rangle$

normalized on its left, the expectation value just becomes

$$\langle \Psi_2 | \hat{O}_i | \Psi_1 \rangle = \sum_{a_{i-1}, ai} \sum_{\sigma_i, \sigma_i'} \hat{O}^{\sigma_i, \sigma_i'} \tilde{M}^{\sigma_i \dagger}_{a_{i-1}, a_i} M^{\sigma_i'}_{a_{i-1}, a_i} \tag{2.19}$$

$$= \sum_{\sigma_i, \sigma_i'} \hat{O}^{\sigma_i, \sigma_i'} Tr \left( \tilde{M}^{\sigma_i \dagger} M^{\sigma_i'} \right) \tag{2.20}$$

When there are two or more operators acting simultaneously, for instance, when calculating correlation functions, this is generally not possible. But the computational cost can be reduced by using this normalization condition beyond whichever site there is no operator acting, shown in Fig.2.7b.

### 2.6.1 Need for shift of Orthonormality center

To make use of the orthonormality condition for efficient calculation of expectation values at the $(i+1)^{th}$ site, the use of orthonormality center, which is initially at the $i^{th}$ site, should be shifted to the $(i+1)^{th}$ site. As per the representation described above, a mixed canonical MPS with respect to the $i^{th}$ site then needs to

be reconstructed so that it is also mixed canonical w.r.t to the $(i+1)^{th}$ site. Doing this for every iteration is a computationally expensive job. There is a workaround though, a representation suggested by Guifré Vidal in 2004 [1,13], which makes every site an orthogonality center in a single step.

### 2.6.2 Vidal's Canonical Form: Every site is an orthogonality center

The representation of $|\Psi\rangle$ given by Vidal is the following :

$$|\Psi\rangle = \sum_{\sigma_1 \ldots \sigma_L} \Gamma^{\sigma_1} \Lambda^{(1)} \Gamma^{\sigma_2} \Lambda^{(2)} \Gamma^{\sigma_3} \Lambda^{(3)} \ldots \Gamma^{\sigma_{L-1}} \Lambda^{(L-1)} \Gamma^{\sigma_L} \tag{2.21}$$

In the above expression, there is a matrix $\Gamma^{\sigma_i}$ for each site $i$, and a diagonal matrix of singular values $\Lambda^{(i)}$ obtained by iterative SVD. Similar to the construction of a left (or right) canonical MPS, we perform a successive reshaping 'SVD'ing as described in section 2.2

$$\begin{aligned}
c_{\sigma_1,\ldots,\sigma_L} &= c_{\sigma_1,(\sigma_2\ldots,\sigma_L)} \\
&= \sum_{a_1} M^1_{\sigma_1,a_1} \Lambda^{(1)}_{a_1,a_1} V^{\dagger}_{a_1,(\sigma_2\ldots,\sigma_L)} \\
&= \sum_{a_1} \Gamma^{\sigma_1}_{1,a_1} c'_{(a_1,\sigma_2),\sigma_3,\ldots\sigma_L} && (2.22) \\
&= \sum_{a_1,a_2} \Gamma^{\sigma_1}_{1,a_1} M^2_{(a_1,\sigma_2),a_2} \Lambda^{(2)}_{a_2,a_2} V'^{\dagger}_{a_2,(\sigma_3\ldots,\sigma_L)} && (2.23) \\
&= \sum_{a_1,a_2} \Gamma^{\sigma_1}_{1,a_1} \Lambda^{(2)}_{a_2,a_2} \Gamma^{\sigma_1}_{a_1,a_2} V'^{\dagger}_{a_2,(\sigma_3\ldots,\sigma_L)} && (2.24) \\
&\vdots && (2.25) \\
&= \sum_{\sigma_1 \ldots \sigma_L} \Gamma^{\sigma_1} \Lambda^{(1)} \Gamma^{\sigma_2} \Lambda^{(2)} \Gamma^{\sigma_3} \Lambda^{(3)} \ldots \Gamma^{\sigma_{L-1}} \Lambda^{(L-1)} \Gamma^{\sigma_L} && (2.26)
\end{aligned}$$

At every step after SVD, we replace the $M$ matrix as ,

$$M = \Lambda^{(i-1)}_{a_{i-1},a_{i-1}} \Gamma^{\sigma_i}_{a_{i-1},a_i} \tag{2.27}$$

Therefore, to find the $\Gamma^{\sigma_i}$ at each step except the first, we need to calculate the quantity $(\Lambda^{(i-1)})^{-1}M$ . Thus we need to discard the zero singular values for this representation which may sometimes lead to inaccuracy.

## 2.7 DMRG as a Variational principle

The Density Matrix Renormalization group (DMRG) method was developed by Steven R. White in 1992[14]. This is a very accurate method to calculate the eigenvalues and eigenvectors of strongly correlated lattice model Hamiltonians. This can treat large low dimensional systems (generally 1-dimensional and quasi 1-dimensional) which exact diagonalization cannot handle.

Since we are primarily interested in ground state properties, we need to find a $\Psi$ which minimizes the energy expectation value $\langle\Psi|\mathcal{H}|\Psi\rangle/\langle\Psi|\Psi\rangle$. Now, $|\Psi\rangle$ and $\mathcal{H}$ are expressed as MPS and MPO respectively. For an MPS $|\Psi\rangle = M^{\sigma_1}M^{\sigma_2}\dots M^{\sigma_L}$ this amounts to solving the equation

$$\frac{\partial}{\partial \boldsymbol{M}^{\sigma_i}} \left(\langle\Psi|\mathcal{H}|\Psi\rangle\right) - E\langle\Psi|\Psi\rangle = 0 \tag{2.28}$$

where $E$ is a Lagrange multiplier as $\langle\Psi|\Psi\rangle$ is a constant of normalization. The solution can be represented as a tensor network diagram shown in Fig 2.8a and 2.8b, considering the MPO form of $\mathcal{H}$ as in Eq. 2.9

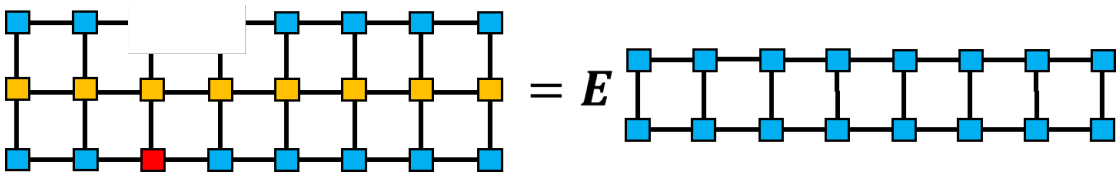


(a)

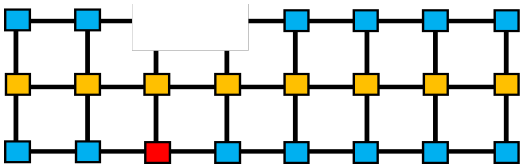


(b)

Figure 2.8: Tensor network diagram for DMRG with (a) an unnormalized MPS and (b) a normalized MPS.

## 2.8 Iterative Sweeping

$$\langle\Psi|\mathcal{H}|\Psi\rangle = \sum_{\substack{\sigma_1,\ldots,\sigma_L,\\ \sigma'_1,\ldots,\sigma'_L,\\ a_1,\ldots,a_L}} \overbrace{\left[\left(M^{\sigma_1\dagger}_{a_1}\hat{W}^{\sigma_1,\sigma'_1}_{b_1}M^{\sigma'_1}_{a'_1}\right)\ldots\left(M^{\sigma_{i-1}\dagger}_{a_{i-2},a_{i-1}}\hat{W}^{\sigma_{i-1},\sigma'_{i-1}}_{b_{i-2},b_{i-1}}M^{\sigma'_{i-1}}_{a'_{i-2},a'_{i-1}}\right)\right]}^{\text{LEFT-BLOCK}}$$

$$\times \quad \left(M^{\sigma_i\dagger}_{a_{i-1},a_i}\hat{W}^{\sigma_i,\sigma'_i}_{b_{i-1},b_i}M^{\sigma'_i}_{a'_{i-1},a'_i}\right)\left(M^{\sigma_{i+1}\dagger}_{a_i,a_{i+1}}\hat{W}^{\sigma_{i+1},\sigma'_{i+1}}_{b_i,b_{i+1}}M^{\sigma'_{i+1}}_{a'_i,a'_{i+1}}\right) \quad \times$$

$$\underbrace{\left[\left(M^{\sigma_{i+2}\dagger}_{a_{i+1},a_{i+2}}\hat{W}^{\sigma_{i+2},\sigma'_{i+2}}_{b_{i+1},b_{i+2}}M^{\sigma'_{i+1}}_{a'_{i+1},a'_{i+2}}\right)\ldots\left(M^{\sigma_L\dagger}_{a_L}\hat{W}^{\sigma_L,\sigma'_L}_{b_L}M^{\sigma'_L}_{a'_L}\right)\right]}_{\text{RIGHT-BLOCK}}$$

$$= \mathbf{L}_{1,i-1}\left(M^{\sigma_i\dagger}\hat{W}^{\sigma_i,\sigma'_i}M^{\sigma'_i}\right)\left(M^{\sigma_{i+1}\dagger}\hat{W}^{\sigma_{i+1},\sigma'_{i+1}}M^{\sigma'_{i+1}}\right)\mathbf{R}_{i+2,L} \tag{2.29}$$

To perform iterative energy minimization, which will be explained in details in the next section, one performs an iterative SVD truncation procedure, by constructing effective one or two site Hamiltonian. To do that, for instance, sequential

tensor contractions (or joining of legs) are performed, giving rise to left and right blocks, with two sites $i$ and $i+1$ in between these blocks. The first term of Eq.2.28 then amounts to removing $M^{\sigma_i\dagger}$ and thus, the effective expression takes the form $H_{eff}|\Psi\rangle$ where $H_{eff}$ is a $(a_i\sigma_i\sigma_{i+1}a_{i+1}) \times (a_i\sigma_i\sigma_{i+1}a_{i+1})$ effective Hamiltonian matrix. This matrix can be diagonalized to obtain the ground state, $\Psi_0$ for two sites. Following that, SVD is performed to split them into individual matrices of the MPS for the two sites. The lowest eigenvalue $\lambda_0$ corresponding to $\Psi_0$ is the estimate of the ground state energy of the system.

## 2.9 DMRG Sweeps in a Computer

Therefore, as mentioned in the previous section, the iterative DMRG sweep is performed in the following way:

## 2.10 Time Evolving Block Decimation (TEBD)

The *Time Evolving Block Decimation* (TEBD), developed in 2004 [13,15–18] is a popular method to study real as well as imaginary time evolution of one dimensional quantum many-body systems in the MPS formalism. It is based on the *Trotter-Suzuki* [19] Decomposition of the propagator $e^{-i\mathcal{H}\delta t}$. This method is efficient and fast but is mostly applicable for short-ranged Hamiltonians. Initially it was developed for finite size systems, but in 2007, its infinite-size variant has been also developed.

### 2.10.1 Trotter-Suzuki Decomposition

Since two consecutive terms of a nearest-neighbor Hamiltonian generally do not commute, unitarity is not preserved. The way to solve this issue is to split the Hamiltonian into sums of odd and even terms.

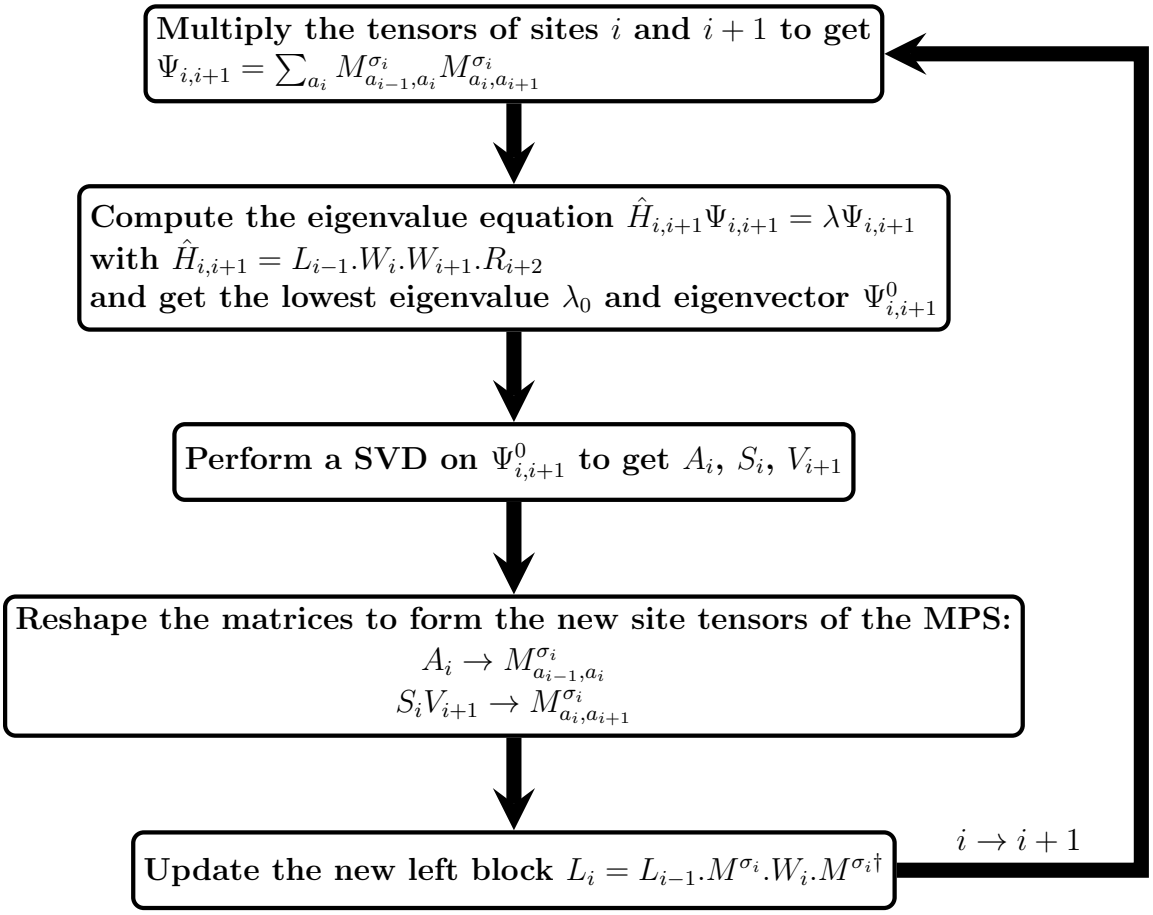


Figure 2.9: Left to Right sweep of the 2-site DMRG algorithm

$$\begin{aligned}
\mathcal{H} &= \hat{H}_{odd} + \hat{H}_{even} \\
\hat{H}_{odd} &= \hat{h}_{1,2} + \hat{h}_{3,4} + \hat{h}_{5,6} + \ldots = \sum_{i,odd} \hat{h}_{i,i+1} \\
\hat{H}_{even} &= \hat{h}_{2,3} + \hat{h}_{4,5} + \hat{h}_{6,7} + \ldots = \sum_{i,even} \hat{h}_{i,i+1}
\end{aligned} \tag{2.30}$$

The propagator can be calculated using the Baker-Campbell-Hausdorff formula

$$\begin{aligned}
U^{exact}(\delta t) &= e^{-i\mathcal{H}\delta t} \\
&= e^{-i\hat{H}_{\text{odd}}\delta t} e^{-i\hat{H}_{\text{even}}\delta t} e^{-i\left[\hat{H}_{\text{odd}},\hat{H}_{\text{even}}\right]\delta_t^2}
\end{aligned} \tag{2.31}$$

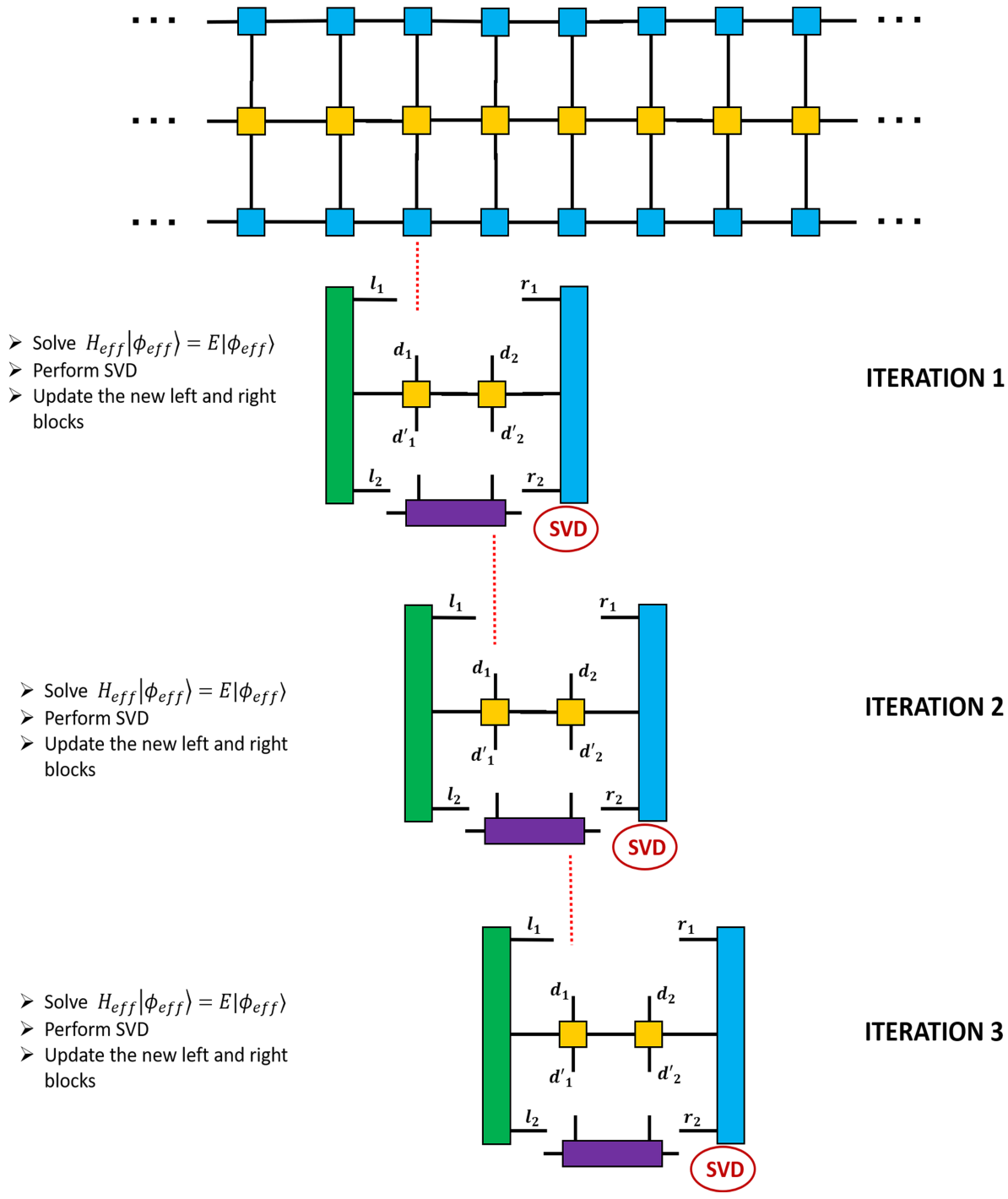


Figure 2.10: Schematic of the 2-site DMRG sweep algorithm

For TEBD of the first order (TEBD1), we consider

$$\begin{aligned} U^{\text{TEBD1}}(\delta t) &= e^{-i\hat{H}_{\text{odd}}\delta t}e^{-i\hat{H}_{\text{even}}\delta t} \\ U^{exact}(\delta t) &= U^{\text{TEBD1}}(\delta t) + \mathcal{O}(\delta t^2) \end{aligned} \tag{2.32}$$

For a very small value of $\delta t$ (ideally $\delta t \to 0$) TEBD1 is very accurate. The advantage of TEBD is that it preserves unitarity upto the order of accuracy, which is $\delta t$ for TEBD1, and better for higher orders.

The second order form TEBD2 is obtained by rearranging the terms in a symmetric way

$$\begin{aligned} U^{\text{TEBD2}}(\delta t) &= e^{-i\hat{H}_{\text{even}}\delta t/2}e^{-i\hat{H}_{\text{odd}}\delta t}e^{-i\hat{H}_{even}\delta t/2} \\ U^{exact}(\delta t) &= U^{\text{TEBD2}}(\delta t) + \mathcal{O}(\delta t^3) \end{aligned} \tag{2.33}$$

A more accurate but computationally slightly expensive would be to consider the fourth order form, TEBD4,

$$\begin{aligned} U^{\text{TEBD2}}(\delta t) &= U^{\text{TEBD2}}(\delta t_1)U^{\text{TEBD2}}(\delta t_1)U^{\text{TEBD2}}(\delta t_2)U^{\text{TEBD2}}(\delta t_1)U^{\text{TEBD2}}(\delta t_1) \\ &= e^{-i\hat{H}_{\text{even}}\delta t_1/2}e^{-i\hat{H}_{\text{odd}}\delta t_1}e^{-i\hat{H}_{even}\delta t_1}e^{-i\hat{H}_{\text{odd}}\delta t_1}e^{-i\hat{H}_{even}(\delta t_1+\delta t_2)/2} \\ &\quad \times e^{-i\hat{H}_{\text{odd}}\delta t_2}e^{-i\hat{H}_{even}(\delta t_1+\delta t_2)/2}e^{-i\hat{H}_{\text{odd}}\delta t_1}e^{-i\hat{H}_{even}\delta t_1}e^{-i\hat{H}_{\text{odd}}\delta t_1}e^{-i\hat{H}_{\text{odd}}\delta t_2} \end{aligned} \tag{2.34}$$

where $\delta t_1 = \dfrac{1}{1-4^{1/3}}\delta t$ and $\delta t_2 = (1-4\delta t_1)\delta t$ .

The Trotter-Suzuki method is available for nearest-neighbor interactions. To extend the algorithm to next-nearest-neighbor or longer range interactions, *swap gates* are used[20]. By these operators, the indices are temporarily swapped to make them nearest-neighbor and again they are swapped in the reverse order after the time evolution.

### 2.10.2 Algorithm

After segregating the odd and even parts (or mutually non-commuting parts of the Hamiltonian) the operators $\hat{H}_{\text{even}}$ and $\hat{H}_{\text{odd}}$ are calculated. The operators applied to the sites are individual operators and not an MPO. For example, the operator for any two sites $i, i+1$ for the z-component of the 1d Heisenberg model $U^{(\sigma_i,\sigma_{i+1}),(\sigma'_i,\sigma'_{i+1})}(\delta t) = e^{ih_{i,i+1}\delta t}$ where

$$h_{i,i+1} = \mathbb{1}_{i-1} \otimes S^z_i \otimes S^z_{i+1} \otimes \mathbb{1}_{i+2} \tag{2.35}$$

or simply

$$h_{i,i+1} = S^z_i \otimes S^z_{i+1} \tag{2.36}$$

since identity operators are absorbed while creating the left and right blocks in the Hamiltonian. These operators are then acted on the $i^{\text{th}}$ and $i+1^{\text{th}}$ sites of the MPS, namely

$$\Psi^{\sigma_i\sigma_{i+1}}(t) = \Lambda^{(i-1)}\Gamma^{\sigma_i}\Lambda^{(i)}\Gamma^{\sigma_{i+1}}\Lambda^{(i+1)} \qquad \text{and} \tag{2.37}$$

$$\begin{aligned}\Psi^{\sigma_i\sigma_{i+1}}(t+\delta t) &= U_{i,i+1}(\delta t)\Psi^{\sigma_i\sigma_{i+1}}(t) \\ &= M^{\sigma_i}\Lambda'^{\,(i)}V^{\sigma_{i+1}\dagger} \\ &= \Lambda^{(i-1)}\left(\Lambda^{(i-1)}\right)^{-1} M^{\sigma_i}\Lambda'^{\,(i)}V^{\sigma_{i+1}\dagger}\left(\Lambda^{(i+1)}\right)^{-1}\Lambda^{(i+1)} \qquad (2.38) \\ &= \Lambda^{(i-1)}\Gamma'^{\sigma_i}\Lambda'^{(i)}\Gamma'^{\sigma_{i+1}}\Lambda^{(i+1)} \qquad (2.39)\end{aligned}$$

where the new tensors as constructed as
$\Gamma'^{\sigma_i}_{a_{i-1}a_i} = \left(\Lambda^{(i-1)}_{a_i,a_i}\right)^{-1} M^{\sigma_i}_{a_{i-1},a_i}$ and $\Gamma'^{\sigma_{i+1}}_{a_i a_{i+1}} = V^{\sigma_{i+1}\dagger}_{a_i,a_{i+1}}\left(\Lambda^{(i+1)}_{a_{i+1},a_{i+1}}\right)^{-1}$

For clarity, a full flowchart of all the steps required to compute within DMRG programs are described below.

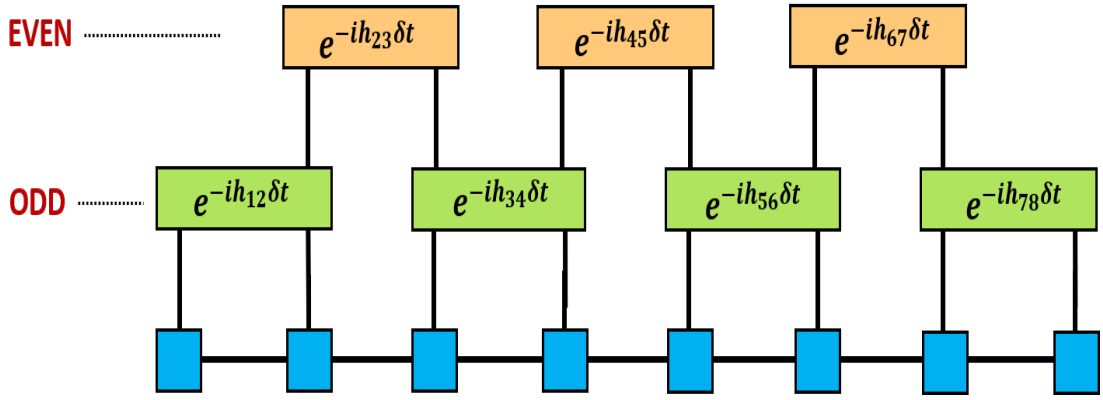


Figure 2.11: Schematic for the TEBD algorithm

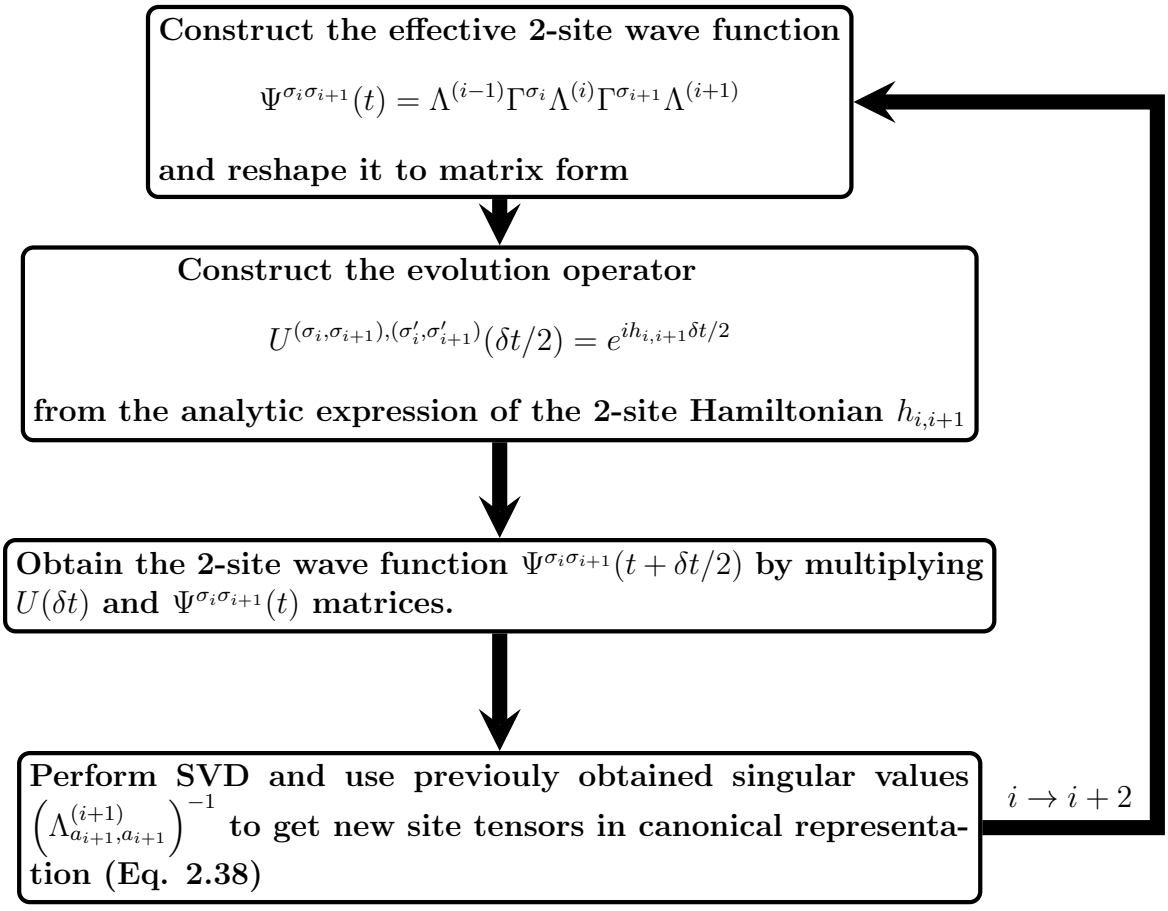


Figure 2.12: Algorithm for the left-right sweep of the TEBD1 algorithm

Now, the above algorithm is followed separately for starting from odd and even sites. For the right-left sweep, exactly the same algorithm is followed starting from the right, only with sites $i$ and $i-1$ at every iteration.

Also, for TEBD2 and TEBD4 algorithms, the same flowchart is followed both for odd and even sites, but these operations are sequentially done a number of times, following Eqs. 2.33 and 2.34.

In this chapter, we have given details of the MPS methods in terms of pictorial representations, the description of what it contains and how to implement these in coding. We have developed these methods to calculate the static and dynamic properties for both bosonic and fermionic systems. The codes have been developed in-house in Python and Julia languages. The DMRG and TEBD algorithms have been developed and verified with our home-built Exact Diagonalization codes as well as the TenPy package developed by Hauschild *et al.*[21]. We have also implemented these codes in our works, which have been described in chapters 3 and 5.

Currently, we are developing the Time Dependent Variational Principle (TDVP)[19], which is the most accurate time evolution method among all the existing methods in the MPS formalism. In the future, we also plan to implement these methods for dissipative bosonic as well as fermionic chains to study the dynamics of their decoherence in the presence of macroscopic baths.

# References

[1] Schollwöck, U., Ann. Phys., **326**, 96-192 (2011).

[2] Rommer, S. and Ostlund, S., Phys. Rev. B **55**, 2164–2181 (1997).

[3] Dukelsky, J., Martín-Delgado, M.A., Nishino, T. and Sierra, G., Euro. Phys. Lett. **43**, 457 (1998).

[4] McCulloch, I. P., J. Stat. Mech. **10**, P10014 (2007).

[5] Friesdorf, M., Werner, A. H., Brown, W., Scholz, V. B. and Eisert, J., Phys. Rev. Lett. **114**, 170505 (2015).

[6] Schuch, N. Wolf, M. M., Verstraete, F. and Cirac, J. I. Phys. Rev. Lett. **100**, 030504 (2008) .

[7] Schollwöck, U., Rev. Mod. Phys. **77**, 259–315 (2005).

[8] Eisert, J., Cramer, M., and Plenio, M. B., Rev. Mod. Phys. **82**, 277–306 (2010).

[9] Gómez-Rodríguez, Rev. Mex. Fís **46**, 5 (2000).

[10] Oseledets, I. V., SIAM J. Sci. Comput. **33**, 2295–2317 (2011).

[11] Pirvu, B., Murg, V., Cirac, J, I. and Verstraete, F., New J. Phys. **12**, 025012 (2010).

[12] Parker, D. E., Cao, X. and Zaletel, M. P., Phys. Rev. B, **102**, 035147 (2020).

[13] G. Vidal, Phys. Rev. Lett. **93**, 04050 (2004).

[14] White, S. R., Phys. Rev. Lett. **69**, 19 (1992).

[15] Zwolak, M. and Vidal, G., Phys. Rev. Lett. **93**, 207205 (2004).

[16] Verstraete, F., García-Ripoll, J. J. and Cirac, J. I., Phys. Rev. Lett., **93**, 207204 (2004).

[17] Vidal, G., Phys. Rev. Lett., **98**, 070201 (2007).

[18] Orús, R. and Vidal, G., Phys. Rev. B **78**, 155117 (2008).

[19] Paeckel , S., Köhler, T., Swoboda, A., Manmana, S. R., Schollwöck, U. and Hubig, C., Ann. Phys. **411**, 167998 (2019).

[20] Stoudenmire, E. M. and White, S. R., New J. Phys., **12**, 055026, (2010).

[21] https://tenpy.readthedocs.io/en/latest/

# 3

# Loss of classicality in an alternating Spin Chain in presence of next-neighbor coupling and Dzyaloshinskii-Moriya interaction

## 3.1 Introduction

Low dimensional quantum spin systems are of considerable interest as they exhibit a wide range of exotic physical phenomena[2,3]. Due to strong quantum fluctuations, in most of the quantum low dimensional systems, the long range order gets destroyed even at absolute zero temperature. Many such properties have theoretically and computationally been predicted[4–7] and most of those have already been realized experimentally[8–13]. The most popular model to explain these phenomena is the Heisenberg model along with various other terms such as anisotropy[14–17] and Dzyaloshinskii-Moriya[18,19] interactions. Most of these terms break the SU(2) symmetry of spin-1/2 systems and lead to exotic broken symmetry ground state.

The low-lying excitations in these systems vary dramatically depending on

the site spins (whether they are integer or half-odd-integer) and nature of the superexchange interactions. The nearest neighbor integral spin or nearest and next-neighbor coupled half-odd-integer spins show a finite gap in the excitation spectrum and in effect a short range two-spin correlation functions in the ground state. Interestingly, the next-neighbor coupling induces frustration in the system and such an infinite degeneracy of the classical ground state of the spin system gets lifted when quantum fluctuations are introduced. The gapless spin system, the spin gap due to Resonating Valence Bond or spontaneous dimerization due to frustration, single magnon state, multi-magnon states, spin-glass and spin-ice ground states in a large classes of magnetic systems have already been realized computationally and experimentally. There have been studies on the low-energy and low temperature properties of alternating spin chains with nearest and next nearest neighbor Heisenberg interactions. Such ferrimagnetic systems have been shown to display a rich low energy spectrum with both antiferromagnetic (AFM) ground state and ferromagnetic excitations. Due to underlying non compensating site spins with finite magnetization, these low dimensional systems show long range magnetic order with finite magnetization at temperature. Since quantum fluctuations of the Heisenberg model cannot destroy the classical ferromagnetic order, these alternating spin-chains can be well explained within the limit of Linear Spin Wave Theory (LSWT).

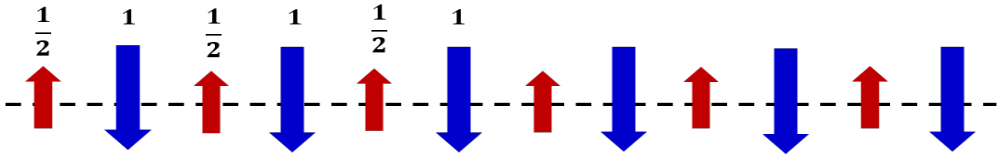


Figure 3.1: Schematic of a spin-$\frac{1}{2}$/spin-1 alternating chain

In this chapter, we are interested in studying the effect of Dzyaloshinskii-Moriya (DM) interactions on the low energy spectrum of Heisenberg chain systems consisting of alternating site spins and with competing exchange interactions[1]. We have carried out detailed studies on the low-energy properties of these systems using perturbative linear spin-wave theory and non-perturbative density matrix renormalization group methods. We have compared the spin-density, two-spin correlation functions and various order parameters between the perturbative and non-perturbative methods and with change in the magnitude of alternating site spins in the low-dimensional system. In next section, we have carried out the detailed analysis of the low-energy spectrum of an alternating spin chains $(S_1, S_2)$ with nearest and next-nearest neighbor AFM interactions and the z-component of the DM interactions using linear spin-wave theory method. In the subsequent section, DMRG calculations have been performed on the alternating spin systems ($S_1 = 1, S_2 = 1/2$ and $S_1 = 3/2, S_2 = 1/2$) with nearest neighbor Heisenberg AFM interactions and z-component of the DM interactions (and at times with next-nearest neighbor frustrated term). The ground state energy, spin density and two-point equal time correlation functions and various other order parameters have been calculated to characterize the ground state. We have analyzed the effects of DM and next-neighbor frustrations on the low energy properties of these alternating spin chains.

## 3.2 Results with nearest-neighbour interactions

### 3.2.1 Linear Spin Wave Theory analysis

The Heisenberg Hamiltonian for an alternating chain of spins $S_1$ and $S_2$ with Dzyaloshinskii-Moriya (DM) interactions can be written as

$$\mathcal{H} = J\sum_{\langle ij\rangle} \boldsymbol{S}_i.\boldsymbol{S}_j + \boldsymbol{D}.\boldsymbol{S}_i \times \boldsymbol{S}_j \tag{3.1}$$

$$= J\sum_{\langle ij\rangle} S_i^z S_j^z + \frac{J}{2}\left(S_i^+ S_j^- + S_i^- S_j^+\right) + \frac{iD^z}{2}\left(S_i^+ S_j^- - S_i^- S_j^-\right) \tag{3.2}$$

for $J > 0$ and $\boldsymbol{D} = \{D^z, 0, 0\}$

Here the A sublattice comprise of spin-$\frac{1}{2}$ sites and the B sublattice comprise of spin-1.

#### Holstein-Primakoff Transformations and Fourier Transformation

We apply the Holstein-Primakoff transformations

**Sublattice A**

$$\begin{aligned} S_{1,i}^z &= S_1 - a_i^\dagger a_i, \\ S_{1,i}^+ &= \sqrt{2S_1 - a_i^\dagger a_i}\, a_i, \\ S_{1,i}^- &= a_i^\dagger \sqrt{2S_1 - a_i^\dagger a_i}, \end{aligned} \tag{3.3}$$

**Sublattice B**

$$\begin{aligned} S_{2,i}^z &= -S_2 + b_i^\dagger b_i, \\ S_{2,i}^+ &= b_i^\dagger \sqrt{2S_2 - b_i^\dagger b_i}, \\ S_{2,i}^- &= \sqrt{2S_2 - b_i^\dagger b_i}\, b_i \end{aligned} \tag{3.4}$$

Substituting the above equations we get

$$\begin{aligned}\mathcal{H} = J\sum_{\langle ij\rangle}\Bigg[\Big(S_1 - a_i^\dagger a_i\Big)\Big(b_j^\dagger b_j - S_2\Big) + \frac{1}{2}\Bigg(a_i\sqrt{2S_1 - a_i^\dagger a_i}\,b_j\sqrt{2S_2 - b_j^\dagger b_j} \\ + a_i^\dagger\sqrt{2S_1 - a_i^\dagger a_i}\,b_j^\dagger\sqrt{2S_2 - b_j^\dagger b_j}\Bigg)\Bigg] \\ + \frac{iD^z}{2}\sum_{\langle ij\rangle}\Bigg(a_i\sqrt{2S_1 - a_i^\dagger a_i}\,b_j\sqrt{2S_2 - b_j^\dagger b_j} - a_i^\dagger\sqrt{2S_1 - a_i^\dagger a_i}\,b_j^\dagger\sqrt{2S_2 - b_j^\dagger b_j}\Bigg)\end{aligned} \tag{3.5}$$

$$\begin{aligned}&\approx -2NJS_1S_2 + J\sum_{\langle ij\rangle}\Big[S_1 b_j^\dagger b_j + S_2 a_i^\dagger a_i + \sqrt{S_1S_2}\Big(a_i b_j + a_i^\dagger b_j^\dagger\Big)\Big] \\ &\qquad + iD_z\sqrt{S_1S_2}\sum_{\langle ij\rangle}\Big(a_i b_j - a_i^\dagger b_j^\dagger\Big) \\ &= \mathcal{H}_0 + \mathcal{H}_1\end{aligned} \tag{3.6}$$

$\mathcal{H}_0$ being the classical energy. After applying the Fourier transform, we get

$$\mathcal{H}_{1k} = \sqrt{S_1S_2}\sum_{\delta,k}\Big(J^{(+)}e^{-ik\delta}a_k b_{-k} + J^{(-)}e^{ik\delta}a_k^\dagger b_{-k}^\dagger\Big) + 2J\sum_k\Big(S_2 a_k^\dagger a_k + S_1 b_k^\dagger b_k\Big) \tag{3.7}$$

where $\delta$ is the sum of all nearest neighbours.

$J^{(+)} = J + iD^z$ and $J^{(-)} = J - iD^z$ .

For a 1D chain with nearest neighbours placed equidistantly, $\sum_{\delta,k} e^{ik\delta} = \sum_{\delta,k} e^{-ik\delta} = 2\sum_k \cos(\frac{k}{2})$

So, we get,

$$\begin{aligned}\mathcal{H}_{1k} &= 2\sqrt{S_1S_2}\sum_k \cos(\frac{k}{2})\left(J^{(+)}a_k b_{-k} + J^{(-)}a_k^\dagger b_{-k}^\dagger\right) + 2J\sum_k\left(S_2 a_k^\dagger a_k + S_1 b_k^\dagger b_k\right) \\ &= 2\sqrt{S_1S_2}\sum_k \cos(\frac{k}{2})\left(J^{(+)}a_k b_{-k} + J^{(-)}a_k^\dagger b_{-k}^\dagger\right) + J\sum_k\{S_2\left(a_k^\dagger a_k + a_{-k}^\dagger a_{-k}\right) \\ &\quad + S_1\left(b_k^\dagger b_k + + b_{-k}^\dagger b_{-k}\right)\} \end{aligned} \tag{3.8}$$

Here, we have used the fact that $\sum_k a_k^\dagger a_k = \frac{1}{2}\sum_k\left(a_k^\dagger a_k + a_{-k}^\dagger a_{-k}\right)$ and similar for $b^\dagger$ and $b$.

Now, this can be written in matrix form,

$$\mathcal{H}_{1k} = \sum_k \boldsymbol{A}_k^\dagger \boldsymbol{H}_k \boldsymbol{A}_k \tag{3.9}$$

where

$$\boldsymbol{H}_k = \begin{pmatrix} JS_2 & 0 & 0 & J^-\sqrt{S_1S_2}\cos(\frac{k}{2}) \\ 0 & JS_1 & J^-\sqrt{S_1S_2}\cos(\frac{k}{2}) & 0 \\ 0 & J^+\sqrt{S_1S_2}\cos(\frac{k}{2}) & JS_2 & 0 \\ J^+\sqrt{S_1S_2}\cos(\frac{k}{2}) & 0 & 0 & JS_1 \end{pmatrix} \tag{3.10}$$

The above matrix is written in the basis $\boldsymbol{A}_k = \{a_k^\dagger, b_k^\dagger, a_{-k}, b_{-k}\}$

### Bogoliubov Transformation and Diagonalization

The Bogoliubov transformation can be written in a generalized form as:

$$\boldsymbol{A}_k = \boldsymbol{V}_k.\tilde{\boldsymbol{A}}_k \tag{3.11}$$

where $\tilde{\boldsymbol{A}}_k$ is the array of 4 Bogoliubov operators and $\boldsymbol{V}_k$ is the coefficient matrix. The diagonal form can be obtained by the similarity transformation

$$\boldsymbol{V}_k^{\dagger}\mathcal{H}_k\boldsymbol{V}_k = \boldsymbol{\Omega}_k \tag{3.12}$$

Also, the commutation relations are preserved after transformation into the Bogoliubov basis. So,

$$\boldsymbol{g} = \boldsymbol{V}_k\ \boldsymbol{g}\ \boldsymbol{V}_k^{\dagger} \tag{3.13}$$

where $\boldsymbol{g}$ is the commutator matrix, written as

$$\boldsymbol{g} = \boldsymbol{A}_k\boldsymbol{A}_k^{\dagger} - \left[\left(\boldsymbol{A}_k^{\dagger}\right)^T \boldsymbol{A}_k^T\right]^T = \begin{pmatrix} \mathbb{1}_2 & \\ & -\mathbb{1}_2 \end{pmatrix} \tag{3.14}$$

From Eq. (3.12) and (3.13), we get

$$\left(\boldsymbol{g}\mathcal{H}_k\right).\boldsymbol{V}_k = \boldsymbol{V}_k.\left(\boldsymbol{g}\boldsymbol{\Omega}_k\right) \tag{3.15}$$

This is actually the eigenvalue equation. The columns of similarity matrix $\boldsymbol{V}_k$ are the eigenvectors of $(\boldsymbol{g}\mathcal{H}_k)$.
Diagonalizing $(\boldsymbol{g}\mathcal{H}_k)$, and then multiplying by $\boldsymbol{g}^{-1}(=\boldsymbol{g})$ we get the 4 modes,

$$\omega_{1k} = \omega_{4k} = \frac{1}{2}\left\{J\left(S_1 - S_2\right) - \Omega_k\right\} \tag{3.16}$$

and

$$\omega_{2k} = \omega_{3k} = \frac{1}{2}\left\{J\left(S_1 - S_2\right) + \Omega_k\right\} \tag{3.17}$$

where

$$\Omega_k = \frac{1}{2}\sqrt{-4\left(J^2 + D^2\right)S_1S_2\cos^2(k/2) + J^2(S_1 + S_2)^2} \tag{3.18}$$

Two low-energy spin wave dispersion curves are shown in Fig. 3.2, corresponding to the two sublattices with two different bosonic modes. In the case of $D^z = 0$, the lower dispersion mode (colored red) is the gapless mode, due mainly to the antiferromagnetic interactions, while the higher energy dispersion mode is gapped and has features of ferromagnetic interactions. This same relation was obtained by Pati *et al.*[20]. As $D^z$ is increased, within the linear spin-wave theory, the dispersion $\omega_{1k}$ becomes negative near $k = 0$. This implies that there is an instability with respect to static spin-wave formalism[21]. This instability can be removed by applying an external magnetic field as there will be an extra tunable coefficient $B$ of $a_k^\dagger a_k$ due to the field, which will shift the value of $\omega_{1k}$ back to zero. We will see below how the non-perturbative method accounts for such instability when the quantum fluctuations is properly accounted for.

For $D^z > 0.3535$, the discriminant, $\Omega_k^2$ (3.18) becomes negative. Thus, both the $\omega$'s, namely, $\omega_{1k}$ and $\omega_{2k}$ become complex. Hence, the spin wave dispersion curves become unrealistic and are thus no longer remain valid.

**Sublattice Magnetization**

The magnetization for the $A$ sublattice can be written as([22])

$$M_a = S_1 - \langle a^\dagger{}_{i=1} a_{i=1} \rangle = S_1 - \frac{1}{N_{uc}} \sum_{k,k'} \langle a_k^\dagger a_{k'} \rangle \tag{3.19}$$

where $N_{uc}$ is the number of atoms in the unit cell. Using the Bogoliubov transformation defined before $\boldsymbol{A}_k = \boldsymbol{V}_k . \tilde{\boldsymbol{A}}_k$, we get

$$M_a = S_1 - \frac{1}{N_{uc}} \sum_{k,k',m,n} V_k(1,n)^* V_k(1,m) \tilde{A}_k^\dagger(n) \tilde{A}_k(m) \tag{3.20}$$

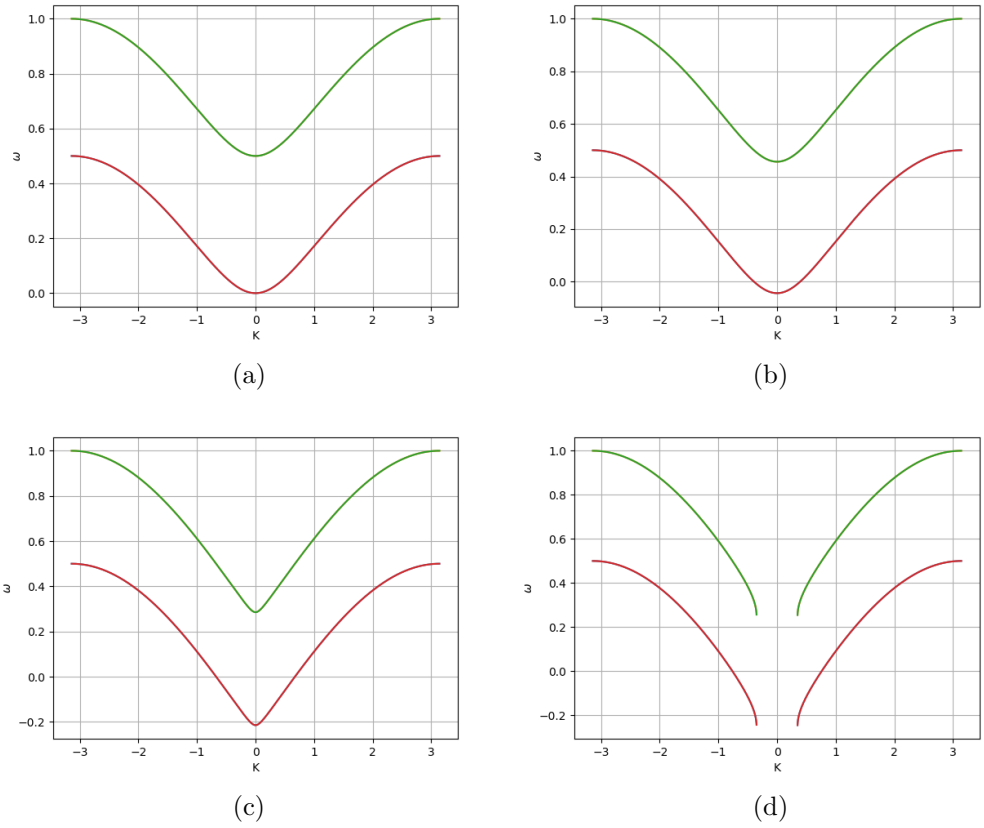


Figure 3.2: Energy dispersion plots for $D^z/J$ = (a) 0.0, (b)0.2, (c) 0.35 and (d) 0.4 for a spin-$\frac{1}{2}$/spin-1 alternating chain

When acting on the ground state, only the terms of the form $\alpha_k \alpha^\dagger{}_k$ in the Bogoliubov basis will have non-zero contribution. So it is sufficient to sum over only terms $m = n = 3, 4$ and $k = k'$. Hence,

$$M_a = S_1 - \frac{1}{N_{uc}} \sum_k \sum_{m=3,4} V_k(1,n)^* V_k(1,n) \tilde{A}_k^\dagger(n) \tilde{A}_k(n) \tag{3.21}$$

$$= \left( S_1 + \frac{1}{2} \right) \tag{3.22}$$

$$+ \frac{1}{2} \int_{-\pi}^{\pi} dk \frac{\left( J(S_1+S_2) + \sqrt{-4\left(J^2+D^2\right) S_1 S_2 \cos^2(k/2) + J^2 (S_1+S_2)^2} \right)^2}{4(J^2+D^2) S_1 S_2 \cos^2(k/2)}$$

$$\tag{3.23}$$

In a similar way, the magnetization for the B- sublattice can be calculated as

$$\begin{aligned} M_b = \langle b^\dagger{}_{i=1} b_{i=1} \rangle - S_2 &= \frac{1}{N_{uc}} \sum_{k,k'} \langle b_k^\dagger b_{k'} \rangle - S_2 \\ &= \frac{1}{N_{uc}} \sum_{k,k'} \sum_{m=3,4} V_k(2,n)^* V_k(2,n) \tilde{A}_k^\dagger(n) \tilde{A}_k(n) - S_2 - \frac{1}{2} \end{aligned} \tag{3.24}$$

As can be seen from linear spin-wave results, for each spin-$\frac{1}{2}$/Spin-1 dimer, the total magnetization is $(S_1 - S_2) = \frac{1}{2}$ since the fluctuations in each of the site spins are exactly opposite and thus gets cancelled out to give finite magnetization value for every dimer. Thus, the system behaves as a classical ferrimagnet with alignment of finite magnetizations of dimers in a lattice. However, this result is valid only for $D^z = 0$, as evident from non perturbative DMRG calculations, discussed in the next subsection. For $D^z \neq 0$, the non-perturbative quantum fluctuations make the spin of each site as well as the dimer to be zero.

### Correlation Function

These correlation functions comprise of 3 types, $\langle S^z_{1i} S^z_{1j} \rangle$, $\langle S^z_{2i} S^z_{2j} \rangle$ and $\langle S^z_{1i} S^z_{2j} \rangle$. Since the system behaves as a ferrimagnet with finite magnetization for every dimer, the correlation functions should be calculated after subtracting the product of the averages of each $S^z$ values, given by

$$\langle S^z_{1i} S^z_{1j} \rangle - \langle S^z_{1i} \rangle \langle S^z_{1j} \rangle = \frac{1}{2\pi} \int_{-\pi}^{\pi} \left\{ 1 + \frac{\Omega_k \cos(k|i-j|}{J(S_1 + S_2)} \right\} dk \tag{3.25}$$

for the first type of correlations.

The plots of the correlation function with distance between the spin sites are shown in Fig 3.3a. This clearly shows very short range order upto only a few sites, which is consistent with the earlier work[20] for $D^z = 0$. But for $D^z \neq 0$, in the LSWT regime, the correlation length is also very small and there is not much significant difference between the correlation function for different values of $D^z$ until the function becomes complex at $D^z \simeq 0.36$. Thus LSWT fails to explain this case, as it assumes that there is primarily antiferromagnetic order with fluctuations, even in presence of $D^z$. This is contrary to all the DMRG results, especially with nonzero $D^z$, presented later.

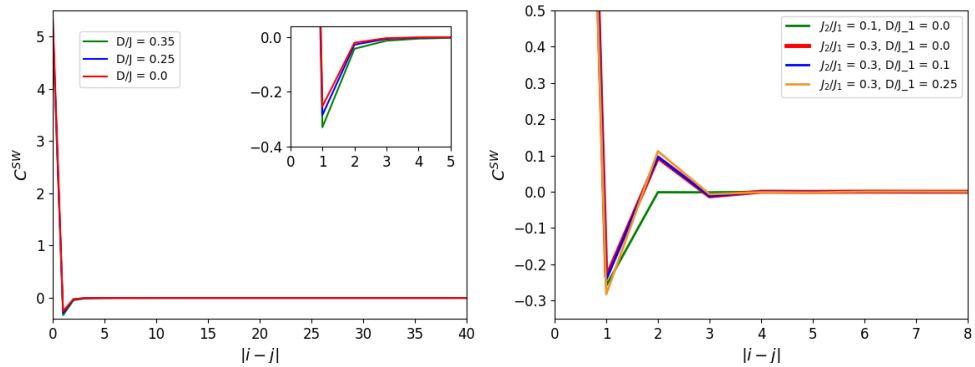


Figure 3.3: $S^z$-$S^z$ correlation function plots from linear spin wave theory for (a) nearest-neighbour and (b) next-nearest-neighbour interactions in a spin-1 alternating chain

### 3.2.2 DMRG Results

Finite size DMRG calculations have been performed in the Matrix Product State (MPS) formalism[25] for a chain of 120 and 240 sites with nearest neighbor (NN) as well as next-nearest neighbor (NNN) magnetic exchange interactions and the z-component of the Dzyaloshinskii-Moriya interactions. In this chapter, we present the results for 240 sites and at times, the same for the 120 sites are also given. The cut off for bond dimension of the MPS has been kept to be 500 and finite size sweeps up to 200 have been used to obtain the converged ground state. For NN interactions without $D^z$, the spin density (shown is Fig.3.4 ) of each site is less than the classical value, but the difference between spin density for each dimer is 1/2 as expected, which is also confirmed from our LSWT calculations and previous work[20]. This means that each site has quantum fluctuations, but each spin-1/2-spin-1 dimer has classical magnetization value. Hence the $S^z$-$S^z$ correlation function, given by

$$C^z\left(|i-j|\right) = \langle S_i^z S_j^z \rangle - \langle S_i^z \rangle \langle S_j^z \rangle \tag{3.26}$$

sharply falls to zero after a length of two sites, as the product of the averages have finite values(Fig3.5a). This is characteristic of a magnetic chain with long range order, which in this case is due to the formation of a ferrimagnetic chain with finite dimer magnetization in the lattice.

However, the moment we turn on the nearest-neighbor DM interactions, it introduces strong quantum fluctuations in each of the spin sites, making the dimer move away from classical magnetic state, as was found for zero DM interaction. Although, the quantum fluctuation was present in each site spin (when $D^z = 0$), the dimer did not have the quantum fluctuation, because oppositely oriented z-component of the site spins had exactly opposite fluctuations, thus cancelling each other's fluctuation making each dimer classical magnetic state. However, with

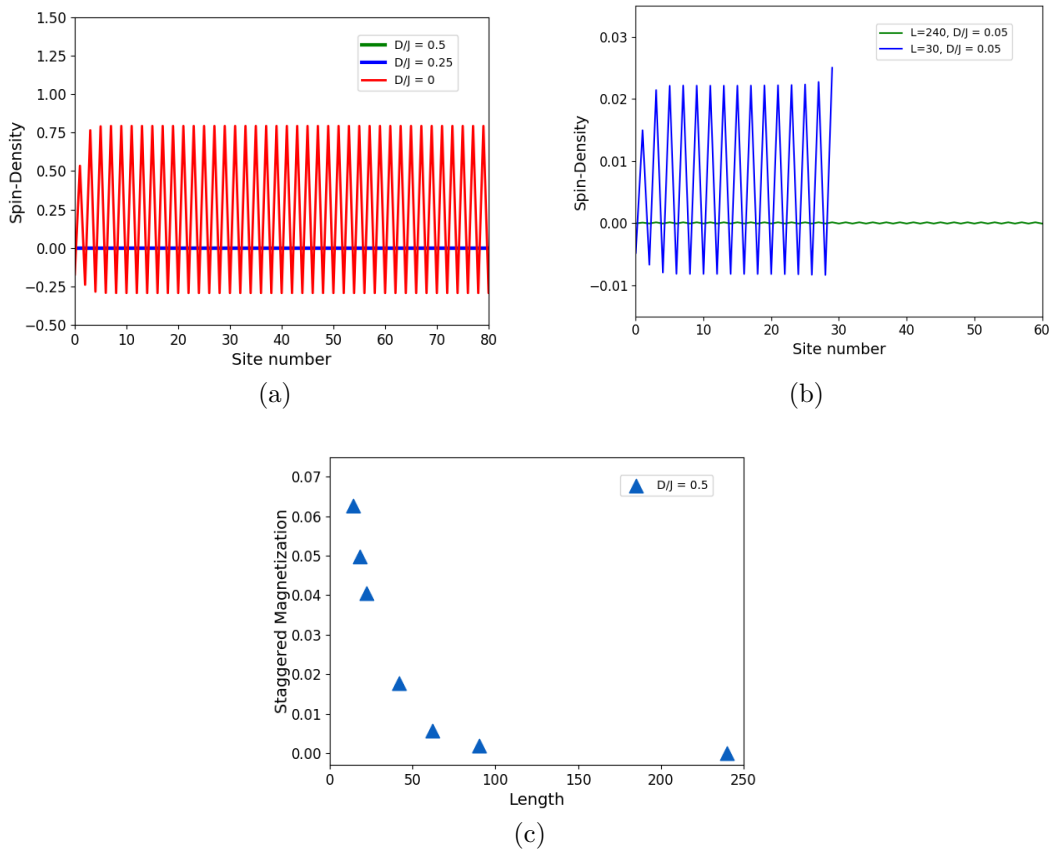


Figure 3.4: Plots of (a)Spin density vs site for a 240 site spin-$\frac{1}{2}$/spin-1 alternating chain for $D^z/J = 0.0, 0.25, 0.5$ (b) Spin density for $D^z/J = 0.05$ for 30 and 240 sites, and, (c) Staggered magnetization for various lengths for $D^z/J = 0.5$, all with NN interactions

$D^z \neq 0.0$, the situation is very different; it not only introduces strong quantum fluctuations in each of the site spins, each of their z-components vanishes and therefore the z-component of the dimer also vanishes. It is quite clear that these fluctuations are stronger for larger magnitude spins and LSWT, which considers fluctuations of classical magnetic ground state to linear order, can never capture such strong fluctuations. This also suggests that although in a ferrimagnet, the interactions are antiferromagnetic, any non-local interactions can destroy the site magnetization of different magnitude magnetic ions as well as the dimeric magnetization of classically non-compensating spin dimers completely. However, we

will see below how spin structure and ordering of the spin sites in a ferrimagnet change when DM interactions are introduced and varied.

**Onset of instability of the classical ferrimagnetic state with $D^z$**

The classical ferrimagnetic state of the alternating spin $\frac{1}{2}$/spin-1 chain is unstable even for a small value of $D^z/J$. This is evident from the spin density plots for different values of $D^z/J$. Fig. 3.4a shows the zigzag pattern of the spin density for a 240-site chain for $D^z/J = 0$ and for $D^z/J = 0.25, 0.5$. As can be seen, for the nonzero $D^z/J$, the spin density at every site vanishes. To verify the quantum fluctuation at every site spin, we have considered small and large sized lattice and have calculated spin density for a small $D^z/J$ value. It is clear from Fig. 3.4b that, for $D^z/J = 0.05$, the magnetization fluctuates antiferromagnetically, however, the scale of fluctuation is quite small (of the order of $10^{-2}$). However, as we increase the lattice length, the site magnetization vanishes. Thus, in the thermodynamic limit, when the system size goes to infinity, the magnetization will go to zero eventually, even for small DM interactions. In Fig. 3.4c the staggered magnetization $\frac{1}{L}\sum_{i=1}^{L}|(-1)^i\langle S_i^z\rangle|$ vs chain length has been plotted for a large value $D^z/J = 0.5$, which also clearly shows the nonlinear decrease in magnitude of magnetization with lattice length.

For non-zero $D^z$, although each site z-component spin density vanishes, the two-point z-component spin correlation function $C^z(|i-j|)$ decays at a relatively slower rate, thus introducing quasi-long-range order.

## Structure Factor

The classical ferrimagnetic ordering in the chain is also reflected in the structure factor, $S(q)$, for $D_z^z = 0$. This is shown in Fig 3.5b. The preferred direction of or-

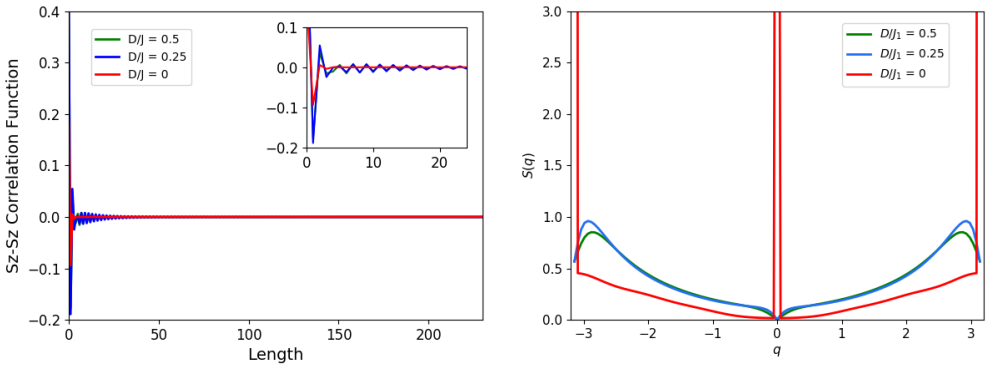


(a) (b)

Figure 3.5: Plots of (a) correlation function $C^z(|i-j|)$ and (b) structure factor $S(q)$ vs $q$, for $D^z/J = 0.0$, 0.25 and 0.5 for a spin-$\frac{1}{2}$/spin-1 alternating chain of 240 sites with NN interactions

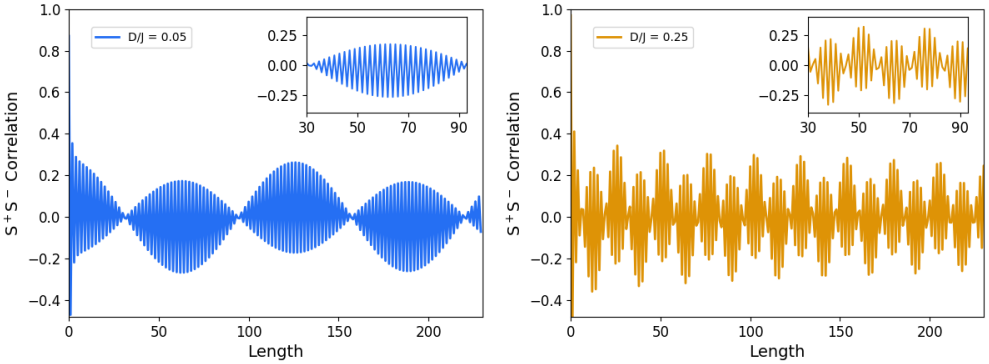


(a) (b)

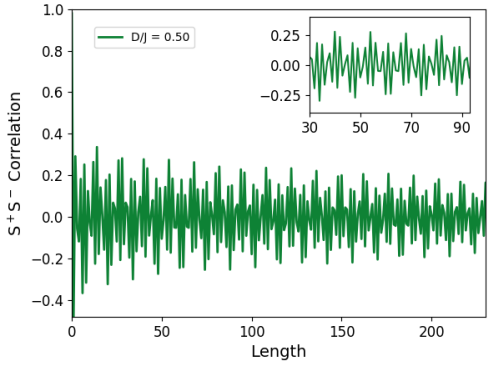


(c)

Figure 3.6: Plots of correlation function $C^{(+)}(|i-j|)$ for $D^z/J = 0.05$ (a), 0.25 (b) and 0.5 (c) for a spin-$\frac{1}{2}$/spin-1 alternating chain of 240 sites with NN interactions

dering of any two spin-$\frac{1}{2}$ or spin-1 at alternate sites is parallel. This is manifested in the sharp peak of $S(q)$ at $q = 0$ and at $q = \pi$. For $D^z \neq 0$, the peak at $q = 0$ or at $q = \pi$ vanishes, as there is no preferred ordering. Nevertheless, there are two broad peaks at $q < \pi$ and $q > -\pi$, referring to some canted or spiral ordering angle. In fact, the spiral ordering angle varies with the magnitude of $D^z$.

### 3.2.3 $S^+$-$S^-$ Correlation

The $S^+$-$S^-$ correlation (or cross-correlation) given by

$$C^{(+)}(|i-j|) = \langle S_i^+ S_j^- \rangle - \langle S_i^+ \rangle \langle S_j^- \rangle \tag{3.27}$$

starts building up with finite values for nonzero $D^z$, which on the other hand was decaying for $D^z = 0$. This correlation function has fluctuations, which continue for longer distances. Interestingly, within each of the spiral order, the fluctuation is maximum in the middle and there appears to be a periodicity, which varies with the variation of the DM strength (Fig.3.6). The DM interaction introduces the spiral order of certain length even in XY-plane, as the term is a vector.

## 3.3 Results with Next-nearest-Neighbor Interactions

### 3.3.1 Spin-Wave Theory Analysis

The Hamiltionian with next-nearest-neighbor interactions can be written in terms of the Holstein-Primakoff bosons as

$$
\begin{aligned}
\mathcal{H} &= J_1 \sum_{\langle ij \rangle} S_i^z S_j^z + \frac{J}{2}\left(S_i^+ S_j^- + S_i^- S_j^+\right) + \frac{iD^z}{2}\left(S_i^+ S_j^- - S_i^- S_j^-\right) + J_2 \sum_{\langle\langle ij \rangle\rangle} S_i^z S_j^z \\
&= J_1 \sum_{\langle ij \rangle} \Bigg[ \left(S_1 - a_i^\dagger a_i\right)\left(b_j^\dagger b_j - S_2\right) + \frac{1}{2}\Bigg( a_i \sqrt{2S_1 - a_i^\dagger a_i}\, b_j \sqrt{2S_2 - b_j^\dagger b_j} \\
&\qquad + a_i^\dagger \sqrt{2S_1 - a_i^\dagger a_i}\, b_j^\dagger \sqrt{2S_2 - b_j^\dagger b_j} \Bigg) \Bigg] \\
&+ J_2 \sum_{\langle\langle ij \rangle\rangle} \Bigg[ \left(S_1 - a_i^\dagger a_i\right)\left(S_1 - a_j^\dagger a_j\right) + \frac{1}{2}\Bigg( \sqrt{2S_1 - a_i^\dagger a_i}\, a_i a_j^\dagger \sqrt{2S_1 - a_j^\dagger a_j} \\
&\qquad + a_i^\dagger \sqrt{2S_1 - a_i^\dagger a_i} \sqrt{2S_1 - a_j^\dagger a_j}\, a_j \Bigg) \Bigg] \\
&+ J_2 \sum_{\langle\langle ij \rangle\rangle} \Bigg[ \left(b_i^\dagger b_i - S_2\right)\left(b_j^\dagger b_j - S_2\right) + \frac{1}{2}\Bigg( b_i^\dagger \sqrt{2S_1 - b_i^\dagger b_i} \sqrt{2S_1 - b_j^\dagger b_j}\, b_j \\
&\qquad + \sqrt{2S_2 - a_i^\dagger a_i}\, b_i b_j^\dagger \sqrt{2S_2 - b_j^\dagger b_j} \Bigg) \Bigg] \\
&+ \frac{iD^z}{2} \sum_{\langle ij \rangle} \Bigg( a_i \sqrt{2S_1 - a_i^\dagger a_i}\, b_j \sqrt{2S_2 - b_j^\dagger b_j} - a_i^\dagger \sqrt{2S_1 - a_i^\dagger a_i}\, b_j^\dagger \sqrt{2S_2 - b_j^\dagger b_j} \Bigg) \\
&\approx -2NJ_1 S_1 S_2 + J_1 \sum_{\langle ij \rangle} \Big[ S_1 b_j^\dagger b_j + S_2 a_i^\dagger a_i + \sqrt{S_1 S_2}\left(a_i b_j + a_i^\dagger b_j^\dagger\right) \Big] \\
&\qquad + iD_z \sqrt{S_1 S_2} \sum_{\langle ij \rangle} \left(a_i b_j - a_i^\dagger b_j^\dagger\right) \\
&+ NJ_2 S_1^2 + J_2 \sum_{\langle\langle ij \rangle\rangle} S_1 \Big[ -a_i^\dagger a_i - a_j^\dagger a_j + a_i a_j^\dagger + a_i^\dagger a_j \Big] \\
&+ NJ_2 S_2^2 + J_2 \sum_{\langle\langle ij \rangle\rangle} S_2 \Big[ -b_i^\dagger b_i - b_j^\dagger b_j + b_i b_j^\dagger + b_i^\dagger b_j \Big]
\end{aligned}
\tag{3.28}
$$

After the Fourier transformation, we get

$$\begin{aligned}\mathcal{H}_{1k} = \sqrt{S_1 S_2}\sum_{\delta,k}\left(J^{(+)}e^{-ik\delta}a_k b_{-k} + J^{(-)}e^{ik\delta}a_k^\dagger b_{-k}^\dagger\right) \\ + 2\sum_k\left[\left(J_1S_2 - J_2S_1\right)a_k^\dagger a_k + \left(J_1S_1 - J_2S_2\right)b_k^\dagger b_k\right] \\ + J_2S_1\left(e^{-2ik\delta}a_k a_k^\dagger + e^{2ik\delta}a_k^\dagger a_k\right) + J_2S_2\left(e^{-2ik\delta}b_k b_k^\dagger + e^{2ik\delta}b_k^\dagger b_k\right) \quad (3.29)\end{aligned}$$

In matrix form it can be written as,

$$\begin{pmatrix} J_1S_2 - J_2S_1(1-\cos(k)) & 0 & 0 & J^-\sqrt{S_1S_2}\cos(k/2) \\ 0 & J_1S_1 - J_2S_2(1-\cos(k)) & J^-\sqrt{S_1S_2}\cos(k/2) & 0 \\ 0 & J^+\sqrt{S_1S_2}\cos(k/2) & J_1S_2 - J_2S_1(1-\cos(k)) & 0 \\ J^+\sqrt{S_1S_2}\cos(k/2) & 0 & 0 & J_1S_1 - J_2S_2(1-\cos(k)) \end{pmatrix}$$

Bogoliubov transformation, followed by diagonalization gives 2 modes as before (the other two are the same):

$$\begin{aligned}\boldsymbol{\omega_{1k}} &= \frac{1}{4}\left[\left(S_1 - S_2\right)\left\{J_1 + J_2\left(1 - 2\cos(2k)\right)\right\}\right] + \Omega_k \\ \boldsymbol{\omega_{2k}} &= \frac{1}{4}\left[\left(S_1 - S_2\right)\left\{J_1 + J_2\left(1 - 2\cos(2k)\right)\right\}\right] - \Omega_k\end{aligned} \quad (3.30)$$

where

$$\Omega_k = \sqrt{-4\left(J_1^2 + D^2\right)S_1S_2\cos^2(k) + \left\{J_1 - 2J_2\left(\frac{1}{2} - \cos(2k)\right)\right\}^2\left(S_1 + S_2\right)^2}$$

A similar expression without he DM interaction had been derived by Mohakud *et al.*[23]. The energy modes dispersion values for different parameters are plotted in Fig. 3.7.

On introducing the next-neighbor AFM coupling, we introduce spontaneous frustration in a one-dimensional antiferromagnetic lattice. This leads to the dis-

persion relation becoming flattened and as the $J_2$ is increased further, the spin group velocity reduces. Interestingly, on further increase of $J_2$, the AFM dispersion mode flattens more, until it becomes negative at $J_2 = 0.25$ and complex. The magnetization in this case (calculated similarly) as in Eqs. 3.24 reduces from its classical value, but for the dimer, it remains the same, $(S_1 - S_2)$, which is classical.

The correlation function vs. length is plotted in Fig 3.3b. Clearly, the LSWT predicts short range order for both non-zero $J_2$ and nonzero $D^z$ values, contrary to DMRG results, whcih is given in next subsection.

### 3.3.2 DMRG Results

First, the DMRG calculations were performed for $J_2/J_1 = 0.4$, as for a spin-1/2 antiferromagnetic chain, this was predicted to have Resonating Valance Bond doubly degenerate ground state, way back in 1969 [26,28]. With next-neighbor interactions term as half of nearest neighbor, the dimer no longer behaves as classical magnetic dimer with finite magnetization value. The magnetization average at each site becomes zero again, thus making the magnetization value in the dimer to be zero. For $D^z = 0$, the system spontaneously dimerizes with introduction of quasi long range order, as evident from the $S^z$-$S^z$ correlation function plotted in Fig.3.8a. As $D^z$ is turned on, unlike that of only nearest neighbor interactions, the quasi long range order is destroyed. Hence, in both the cases, the DM interaction term changes the spin vectors through quantum fluctuations and thereby the two point correlation function between them and effectively reverses completely or to some extent the quasi long range order or short range order set by the Heisenberg interaction terms. Interestingly, even with small values of DM interactions the spontaneous changes in quantum fluctuations in spin density and spin spin correlation functions occur.

The cross-correlation $C^{(+)}(|i-j|)$ builds up more with increase in DM interac-

tions.

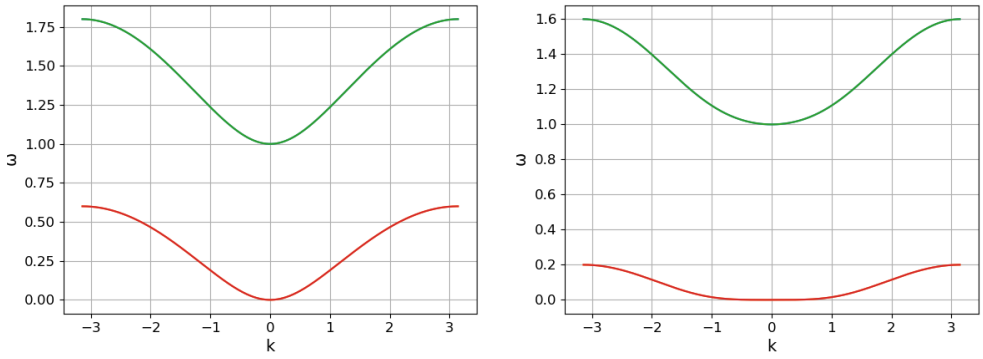


Figure 3.7: Energy dispersion plots for spin-$\frac{1}{2}$/spin-1 alternating chain with next-neighbor frustration for $D^z/J_1$ = (a) 0.0, (b)0.2, (c) 0.35 and (d) 0.4

Interestingly, for $D^z/J_1 = 0$, and with nonzero $J_2$, both $C^z(|i-j|)$ and $C^{(+)}(|i-j|)$ show spiral ordering. However, $J_2$ introduces frustration and due to this, the local as well as the global spin order changes. As can be seen from the correlation functions, the antiferromagnetic short range correlations between two consecutive spin sites (from a given site) remain positive or negative, suggesting local frustrated ferromagnetic domains. This is manifested in the structure factor, $S(q)$, where we find two sharp peaks, each at $\pi/2 > q > 0$ and $0 < q < \pi$ (shown in Fig 3.8b). For $D^z \neq 0$, this local order vanishes, again giving two broad peaks at $-\pi > q > 0$ and $0 < q < \pi$. The structure factor reveals the manifestation of the competing nature of the frustrated interactions and z-component of the DM interactions. Note that, the DM interactions arise due to the local non-centrosymmetry in the spin systems[29–32].

On the other hand, when we consider correlation function between spin raising and lowering operators ($S_i^+ S_j^-$) as a function of distance, $|i-j|$, we find that within short distances, the correlation function between two consecutive sites are positive or negative. This is present at different distances, for $D^z = 0$ as well as for $D^z \neq 0.0$

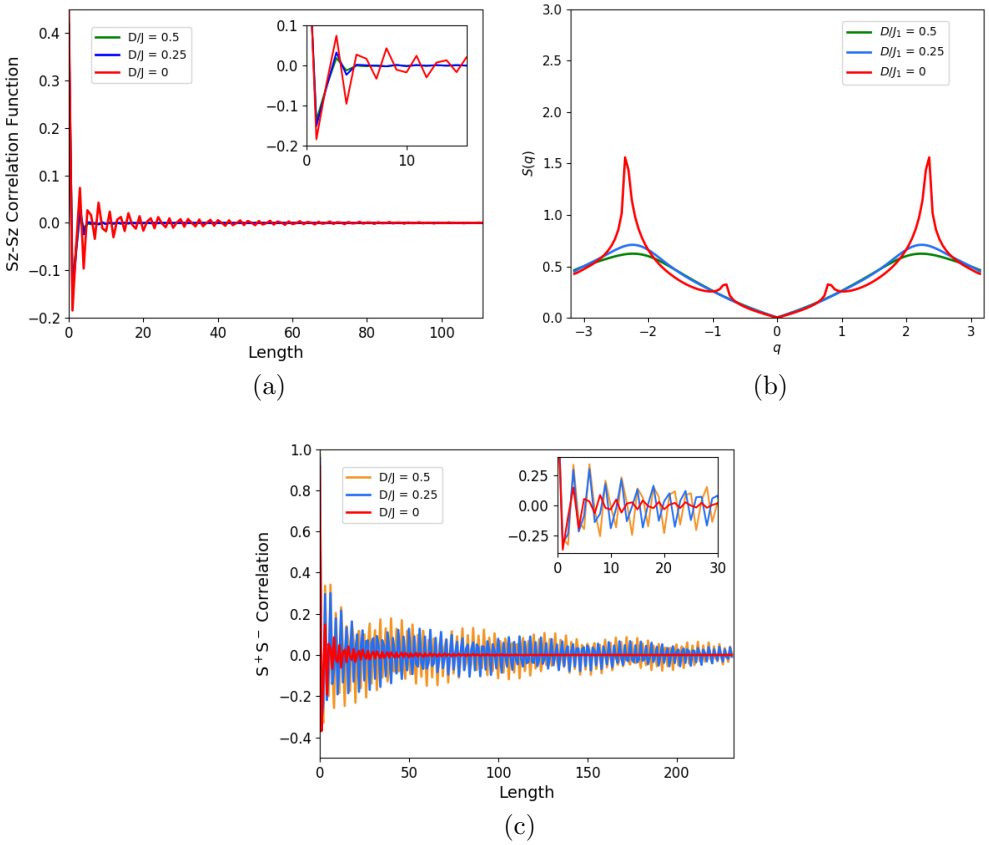


Figure 3.8: Plots of (a) correlation function $C^z\left(|i-j|\right)$, (b) structure factor $S(q)$ vs $q$ and (c) $C^{(+)}\left(|i-j|\right)$ for $J_2/J_1 = 0.4$ and $D^z/J_1 = 0.0$, 0.25 and 0.5 for a spin-$\frac{1}{2}$/spin-1 alternating chain of 240 sites with NNN interactions

values. The $S^+$-$S^-$ correlation functions are plotted in Fig.3.8c as a function of distance between spin sites for various $D^z$ values. From all these figures, it is clear that, since we have considered the z-component of the DM interactions containing $\hat{S}^x$ and $\hat{S}^y$ operators, it preserves the local spiral character for spin components along the XY plane, but kills the z-component local spiral order. Furthermore, investigation reveals that the local spiral angle is different with the magnitude of $D^z$ values,. Thus, the main point is that although $J_2$ introduces frustration and thereby degeneracy and local order along the z-axis, the DM interactions along the in-plane direction preserves the local order, while along the z-direction kills

the local order.

## 3.4 Conclusions

We have investigated the ground state and low energy properties of an alternating spin-$\frac{1}{2}$/spin-1 chain in the presence of DM interactions and next-neighbor frustrations. Without DM and next-neighbor antiferromagnetic interactions, both Linear Spin Wave Theory and non-perturbative DMRG results predict the ground state to be a classical ferrimagnetic state with total spin $N(S_1 - S_2)$. When DM interactions are present, however small it may be, LSWT again predicts a ground state with total spin $N(S_1 - S_2)$, contrary to DMRG results, which show that the ground state to have total spin zero. The reason behind this is that the DM interactions introduce strong quantum fluctuations at each site, thus making the spin at each site zero, and hence the total spin zero. This effect could be captured by the cubic or quartic orders of Spin Wave Theory[24]. In presence of next-neighbor frustration, the system again goes away from classical limit, and the average of z-component of each site spin becomes zero and two point equal time correlations functions show quasi-long range order. When both next-neighbor frustration and DM interactions are present, the magnetic structure generates a short range order in the XY-plane and a local order accompanies it. Both both next-nearest neighbor frustration and DM interactions destroy this spiral order, and also any kind of short range order along the z-axis.

# References

[1] Lahiri A., and Pati,S.K. , arXiv preprint arXiv:2010.06258 (2020).

[2] Parkinson, John B., Farnell and Damian J. J, *An Introduction to Quantum Spin Systems*, Springer Lecture Notes in Physics (2010).

[3] Affleck, I., J. Phys. Condens. Matt. **1**, 3047 (1989).

[4] Anderson, P. W., Science **235**, 1196–1198 (1987).

[5] Anderson, P. W., Baskaran, G. , Zou, Z. and Hsu, T., Phys. Rev. Lett. **58**, 2790-2793 (1987).

[6] Balents, L., Nature **464**, 199-208 (2010).

[7] Sandvik, A. V., AIP Conf. Proc. 1297, 135 (2010).

[8] Arjun, U., Ranjith, K. M., Koo, B., Sichelschmidt, J., Skourski, Y., Baenitz, M., Tsirlin, A. A. and Nath, R., Phys. Rev. B **99**, 014421 (2019).

[9] Buyers, W. J. L., Morra, R. M., Armstrong, R. L., Hogan, M. J., Gerlach, P., Hirakawa and K., Phys. Rev. Lett. **56**, 371 (1986).

[10] Renard,J.P., Verdaguer, M., Regnault,L.P., Erkelens,W. A. C., Rossat-Mignod,J and Stirling, W.G., Europhys. Lett. **3**, 945, (1986).

[11] Senko, C., Richerme, P., Smith, J., Lee, A., Cohen, I., Retzker, A. and Monroe, C., Phys. Rev. X **5**, 021026 (2015).

[12] Breunig, O., Garst, M., Klümper, A., Rohrkamp, J., Turnbull, M. M., and Lorenz, T., Science Advances **3**, eeeao73 (2017).

[13] Banerjee, A., Bridges, C.A., Yan, J.Q., Aczel, A.A., Li, L., Stone, M.B., Granroth, G.E., Lumsden, M.D., Yiu, Y., Knolle, J. and Bhattacharjee, S., Nat. Mater. **15**, 733–740 (2016).

[14] Takahashi, M., and Suzuki, M. , Prog. Theo. Phys., **48**, 2187-2209, (1972).

[15] Binder, K., and Landau, D.P., Phys. Rev. B **13**, 1140 (1976).

[16] Dong, X.Y., Ahmed, S. and McGurn, A.R., Phys. Rev. B **37**, 1575 (1988).

[17] Dmitriev, D.V.,Krivnov, V.Ya., Ovchinnikov, A.A. and Langari, A., JETP **95**, 538 (2002).

[18] Dzyaloshinskii, I.E. Sov. Phys. JETP , 5, 1259–1272 (1957).

[19] Moriya, T., Phys. Rev. Lett. **4**, 228 (1960).

[20] Pati, S. K. , Ramasesha, S. and Sen, D., Phys. Rev. B **55**, 8894 (1997).

[21] Wurstbauer, U. , Majumder, D. and Mandal, S. S. , Dujovne, I., Rhone, T. D., Dennis, B. S., Rigosi, A. F., Jain, J. K., Pinczuk, A., West, K. W. and Pfeiffer, L. N., Phys. Rev. Lett., **107**, 6 (2011).

[22] Rousochatzakis, I. and Läuchli, A. M. and Moessner, R., Phys. Rev. B **85**, 104415 (2012).

[23] Mohakud, S, Pati, S.K., and Miyashita, S., Phys. Rev. B, **76**, 14435 (2007).

[24] Jin, Shangjian, Luo, Cheng, Datta, Trinanjan and Yao, Dao-Xin, Phys. Rev. B **100**, 054410 (2019).

[25] Sch ollwock, U., Ann. Phys. **326** 1 (2011).

[26] Majumdar, C. K., and Ghosh, D., J. Math. Phys. **10**, 1388 (1969).

[27]

[28] Okamoto, K. and Nomura, K., Physics Letters A, 169, 433-437 (1992).

[29] Yi, Tian-Cheng, You, Wen-Long, Wu, Ning and Oleś, Andrzej M., Phys. Rev. B **100** 024423 (2019).

[30] Coffey, D., Rice, T. M., and Zhang, F.C., Phys. Rev. B **44**, 10112 (1991).

[31] Daniel, M, and L. Kavitha, L. , Phys. Rev. B **63**, 172302 (2001).

[32] Mohakud,S., Hijii, K., Miyashita, K. S., and Pati, S. K. J.Phys.Chem. Sol. **73**, 2 (2012).

# 4

# Signatures of nonlinear magnetoelectricity in second harmonic spectra of SU(2) symmetry broken quantum many-body systems

## 4.1 Introduction

The study of Magnetoelectric(ME) effect in materials has gained a huge interest due to their potential applications in sensors[1], ME RAM[2–4] and other spintronic devices. The ME effect is observed in materials where there is a significant coupling between the charge and the spin degrees of freedom. This coupling gives rise to interesting linear as well as nonlinear responses in the presence of an electromagnetic field and are manifested in the measurement of nonlinear magneto-optical susceptibilities. Several mechanisms of this ME effect have been proposed. The most prominent one is due to exchange striction[5] which not only explains ME effect in some multiferroic oxides[6,7], but also organic molecular solids[8]. Others are due to inverse Dzyaloshinskii-Moriya interaction or spin current mechanism[9–11] in

spiral magnets and spin-dependent metal-ligand hybridization[12–15] which involve spin-orbit coupling (SOC). In recent years, electrical control of magnetism have also been discovered in layered 2D materials such as bilayer $MoS_2$[16], $CrI_3$[17], etc. There has also been many first principles studies of ME materials[18–20] Still it is essential to know the role of electronic correlations in the manifestation of this phenomenon. In this chapter, we[21] have theoretically calculated the second order nonlinear ME susceptibilities in small molecular systems using weak incident light as perturbation using a local many-body Hamiltonian. These susceptibilities will appear as small peaks in the second harmonic generation spectrum of the materials.

## 4.2 Nonlinear Magnetoelectric Susceptibilities from Perturbation Theory

Following the phenomenological theory of Landau[22], the second order ME contribution to the polarization ($P$) and magnetization ($M$) at the direction $\alpha$, in the presence of electromagnetic field ($E$,$B$), can be written as

$$\tilde{P}_\alpha(\boldsymbol{E},\boldsymbol{B}) = -\frac{\partial F}{\partial E_\alpha}\Big|_{\boldsymbol{B}} = \tilde{\chi}^{(2)}_{eem}\boldsymbol{EB} \tag{4.1}$$

and

$$\tilde{M}_\alpha(\boldsymbol{E},\boldsymbol{B}) = -\frac{\partial F}{\partial B_\alpha}\Big|_{\boldsymbol{E}} = \tilde{\chi}^{(2)}_{emm}\boldsymbol{EB} \tag{4.2}$$

where $F$ is the free energy of the system. $\tilde{\chi}^{(2)}_{eem}$ and $\tilde{\chi}^{(2)}_{emm}$ are two types of second order ME susceptibilities for the instances when the free energy F is proportional to $\boldsymbol{EEB}$ and $\boldsymbol{EBB}$. In this chapter, we have focussed on $\tilde{\chi}^{(2)}_{eem}$, although the inferences of the results will be valid for $\tilde{\chi}^{(2)}_{emm}$ also. Light has been used as a 'probe' to find the ME coefficients. The electric and magnetic fields of light couple

with the electric dipole moment and the spin, thus manifesting the non-linear ME effects in the polarization or magnetization. To derive the expressions for ME susceptibilities, we consider a general Hamiltonian

$$\hat{H} = \hat{H}_0 + \hat{H}_1 \tag{4.3}$$

where $H_0$ is any arbitrary Hamiltonian and $H_1$ is the perturbation. $H_1$ can be written as

$$\begin{aligned} H_1 &= -\sum_i n_i \boldsymbol{E}.\hat{\boldsymbol{r}}_{\boldsymbol{i}} - \sum_i \boldsymbol{B}.\hat{\boldsymbol{S}}_{\boldsymbol{i}} \\ &= -\boldsymbol{\mu}.\boldsymbol{E} - \boldsymbol{\nu}.\boldsymbol{B} \end{aligned} \tag{4.4}$$

where $\boldsymbol{\mu} = \sum_i n_i \hat{\boldsymbol{r}}_{\boldsymbol{i}}$ and $\boldsymbol{\nu} = \sum_i \hat{\boldsymbol{S}}_{\boldsymbol{i}}$.
Here $\boldsymbol{E} = \boldsymbol{E_0} e^{-i\omega t}$ and $\boldsymbol{B} = \boldsymbol{B_0} e^{-i\omega t}$ are the electric and magnetic fields of the incident light of same frequency, $\omega$.
Using perturbation theory, we calculate the nonlinear optical coefficients following Orr and Ward[23]. The $2nd$ order correction to the polarization is given by[24]

$$\begin{aligned} &a_n^{(2)}(t) = \\ &\frac{1}{\hbar^2} \sum_m \frac{\left(\hat{\boldsymbol{\mu}}_{\boldsymbol{nm}}.\boldsymbol{E}(\omega) + \hat{\boldsymbol{\nu}}_{\boldsymbol{nm}}.\boldsymbol{B}(\omega)\right)\left(\hat{\boldsymbol{\mu}}_{\boldsymbol{mg}}.\boldsymbol{E}(\omega) + \hat{\boldsymbol{\nu}}_{\boldsymbol{mg}}.\boldsymbol{B}(\omega)\right)}{(\omega_{ng} - 2\omega)(\omega_{mg} - \omega)} \\ &\qquad \times e^{i(\omega_{mg} - 2\omega)t} \end{aligned} \tag{4.5}$$

where $\boldsymbol{\mu_{ml}} = \langle \phi_m | \hat{\boldsymbol{\mu}} | \phi_l \rangle$ is the electric transition dipole moment and $\boldsymbol{\nu_{ml}} = \langle \phi_m | \hat{\boldsymbol{S}} | \phi_l \rangle$ is the magnetic transition dipole moment. $\hat{\boldsymbol{S}} = S^x \hat{\boldsymbol{x}} + S^y \hat{\boldsymbol{y}} + S^z \hat{\boldsymbol{z}}$, $S_i$s are spin matrices.
Clearly, the numerator of Eqn.(5) contains terms of the form $(\boldsymbol{\mu}.\boldsymbol{E})(\boldsymbol{\nu}.\boldsymbol{B})$ which leads to the coupling of the electric and the magnetic fields. We calculate second order correction to the polarization due to electric field and magnetic field by

obtaining the expectation values,

$$\tilde{\boldsymbol{P}} = \frac{1}{N}\langle\psi^{(2)}|\hat{\boldsymbol{\mu}}|\psi^{(2)}\rangle \quad \tilde{\boldsymbol{M}}\boldsymbol{s} = \frac{1}{N}\langle\psi^{(2)}|\hat{\boldsymbol{\nu}}|\psi^{(2)}\rangle \ . \tag{4.6}$$

Here $\psi^{(2)}$ is the second order corrected wave function. From Eq.4.1 and Eq.4.5 we get the second order ME coefficients as follows,

$$\begin{aligned}
&\chi^{(2)}_{ijk}(2\omega,\omega) \\
&= \frac{N}{\hbar^2}\sum_{mn}\frac{\mu^i_{gn}\mu^j_{nm}\nu^k_{mg}}{(\omega_{ng}-2\omega+i\eta)(\omega_{mg}-\omega+i\eta)} \\
&+ \qquad \frac{\mu^j_{gn}\mu^i_{nm}\nu^k_{mg}}{(\omega^*_{ng}+\omega)(\omega_{mg}-\omega+i\eta)} \\
&+ \qquad \frac{\mu^j_{gn}\mu^k_{nm}\nu^i_{mg}}{(\omega^*_{ng}+\omega)(\omega^*_{mg}+2\omega)}
\end{aligned} \tag{4.7}$$

To avoid the value of $\chi^{(2)}_{ijk}$ shooting to very large values near the poles we have added the term $i\eta$ in the denominator. In general, when there are two different input frequencies $\omega_1$ and $\omega_2$, there is an intrinsic permutation symmetry $\mathcal{P}_1$ and $\chi^{(2)}_{ijk}$ should be averaged over all such permutations. This expression is similar to that obtained in Ref [21] with the numerator consisting of product of both electric and magnetic transition dipole moments.

$$\mu^i_{gn}\mu^j_{nm}\nu^k_{mg} \ \equiv \langle g|\hat{\mu}^i|n\rangle\langle n|\hat{\mu}^j|m\rangle\langle m|\hat{\nu}^k|g\rangle$$

where $|g\rangle$ is the ground state and $|m\rangle$ and $|n\rangle$ are complete set of excited states of the system. In the absence of spin-orbit coupling, the Hamiltonian commutes with $\hat{S}_z$. So two states connected by the electric dipole moment operator $\hat{\mu}_e$(i.e. having different parity) cannot be connected by the magnetic dipole operator $\hat{\mu}_b$. Hence the second order ME coefficient, $\chi^{(2)}$, would be zero. Only when spin SU(2) symmetry is broken, all the states $|g\rangle$, $|m\rangle$ and $|n\rangle$ are no longer eigenstates of the

$\hat{S}_z$. So coupling of the transition dipole moments could lead to a non-zero $\chi^{(2)}$. Note that in the expression for $\tilde{P}^{(2)}$ there are contributions from nonlinear optical susceptibilities $\tilde{\chi}^{(2)}_{eee}$ arising only due to the electric field of the light which have very large values compared to the cross terms, $\tilde{\chi}^{(2)}_{eem}$ or $\tilde{\chi}^{(2)}_{emm}$.

In the presence of spin-orbit coupling, the Zeeman perturbation term in Eqn. 4.4 would be

$$\sum_i \boldsymbol{B}.(\hat{\boldsymbol{L}}_{\boldsymbol{i}} + \mathbf{2}\hat{\boldsymbol{S}}_{\boldsymbol{i}}) = \sum_i \boldsymbol{B}.(\hat{\boldsymbol{J}}_{\boldsymbol{i}} + \hat{\boldsymbol{S}}_{\boldsymbol{i}}) \tag{4.8}$$

rather than $\sum_i \boldsymbol{B}.\hat{\boldsymbol{S}}_{\boldsymbol{i}}$. Here $\hat{\boldsymbol{J}}$ is the total angular momentum quantum number. But, since it is a good quantum number in this process, the contribution to $\chi^{(2)}$ due to this $\hat{\boldsymbol{J}}$ would be zero, and thus effectively the perturbation term is only due to $\hat{\boldsymbol{S}}$. The term could also be written as $\sum_i \boldsymbol{B}.(2\hat{\boldsymbol{J}}_{\boldsymbol{i}} - \hat{\boldsymbol{L}}_{\boldsymbol{i}})$ and the contribution would be due to $\sum_i \boldsymbol{B}.\hat{\boldsymbol{L}}_{\boldsymbol{i}}$. But the results would not change. Since $\hat{\boldsymbol{L}}_{\boldsymbol{i}}$ and $\hat{\boldsymbol{S}}_{\boldsymbol{i}}$ are coupled, taking the one with the smallest number of eigenstates would suffice.

## 4.3 The Model

We consider a one dimensional (zigzag) chain having alternate sites with spin-orbit coupling (Fig.4.1). The zigzag nature of the system ensures that it can be exposed to an extra dimension of electric field. For simplicity, we have considered only the z-component, $L_z$ of the orbital angular momentum. $|L = \pm\frac{1}{2}\rangle$ are the two eigenstates of the z-component of the orbital angular momentum operator $\hat{L}_z$ with quantum number $l = \frac{1}{2}$. The single orbital Hubbard model for fermions has 4 degrees of freedom per site, which can be represented by $|c\rangle$. Hence a fermionic site with a spin-orbit coupling will have 8 possibilities, $|c\rangle \bigotimes |L = \pm\frac{1}{2}\rangle$.

We have considered the unperturbed Hamiltonian as

$$\hat{H}_0 = \sum_{\langle ij\rangle,\alpha,\sigma} t_{ij} d^{\dagger}_{i\alpha\sigma} d_{j\alpha\sigma} + h.c. + U \sum_i n_{i\alpha\uparrow} n_{i\alpha\downarrow} + \lambda \sum_i \vec{L}_i . \vec{S}_i \tag{4.9}$$

where $d_{i\alpha\sigma} = (c_{i\sigma} \bigotimes \hat{L}^z)_{\alpha\alpha}$. $\alpha$ is the pseudospin index for two eigenstates of $L_z$ ($+1/2$ and $-1/2$) and $\sigma$ is the index for the spin. Here $n_{i\alpha} = c^{\dagger}_{i\alpha} c_{i\alpha}$ is the number operator. $t_{ij}$ and $U$ are respectively the hopping and Hubbard parameters. $\lambda$ is the strength of spin-orbit coupilng. The term $\sum_i \boldsymbol{L_i}.\boldsymbol{S_i} = \sum_i L^z_i S^z_i + L^+_i S^-_i + L^-_i S^+_i$ is considered explicitly to break the SU(2) symmetry. The last term of the Hamiltonian can also be used for spin-hardcore-Boson coupling after the transformation

$$\begin{aligned} L^+ &= \hat{b}^{\dagger} \\ L^- &= \hat{b} \\ L^z &= \hat{b}^{\dagger}\hat{b} - \frac{1}{2} \end{aligned} \tag{4.10}$$

where $\hat{b}^{\dagger}$ and $\hat{b}$ are the bosonic creation and annihilation operators respectively and $[\hat{b}^{\dagger}, \hat{b}] = 1$. Here, we have assumed that there is a hardcore Boson on each site (either 1 Boson or 0 Boson). These Bosons can be coupled with spins which break the SU(2) symmetry.

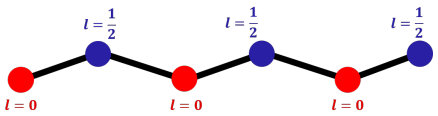


Figure 4.1: Schematic structure of the model system having alternating sites $A$ and $B$.

## 4.4 Results and Discussions

Using the above mentioned basis set, we have diagonalized the Hamiltonian matrix exactly for a chain of 6 sites. We have obtained the 200 lowest eigenstates using Lanczos method[25]. Using these states, ME susceptibilities are computed as given in Eq. 7.

The tumbling average of these susceptibilities are computed from the expression[26,27]

$$||\chi^{(2)}|| = \frac{1}{3}\sqrt{\sum_i \sum_j |\chi^{(2)}_{ijj} + \chi^{(2)}_{jji} + \chi^{(2)}_{jij}|^2} \tag{4.11}$$

These are experimentally important quantities and also define a scalar quantity for better analysis. In the Hamiltonian we have two parameters, on-site correlation $U/t$ and the SOC strength $\lambda/t$. Now, without these two terms, the solution is a plane wave with delocalized eigenstates. When U = 0, the solution is still a charge delocalized state. On the other hand, when $\lambda = 0$ with finite U, the solution is a localized state. Given this physical picture behind our Hamiltonian parameters, we ask here how the coefficients would vary in the regimes (i)$U \to 0, (i)U > \lambda$, (iii) $U \simeq \lambda$ and (iv)$U < \lambda$.

For a fixed value of $U/t = 4.0$, we have shown in Fig.4.2, the variation of $\chi^{(2)}_{eem}$ versus $\omega$ (in units of $\hbar$ eV) for three different values of spin-orbit coupling strength $\lambda/t$ . The plots are obtained by varying $\omega$ in steps of 0.01 upto a value 6.0. Very large value of $\lambda$ is unphysical for real materials but physically realizable in systems of ultracold atoms in optical lattices where the parameters can be tuned experimentally. When $\lambda/t < U/t$, the low energy physics is governed by the strength of $\lambda$. The lowest excitations are those which involve transition from $l_z = \frac{1}{2}$ to $l_z = -\frac{1}{2}$ or vice versa. The excitations corresponding to the exchange involving Hubbard U will have higher energy. The opposite is the case in the $\lambda/t > U/t$ regime, in which the energy is lower for excitations due to magnetic

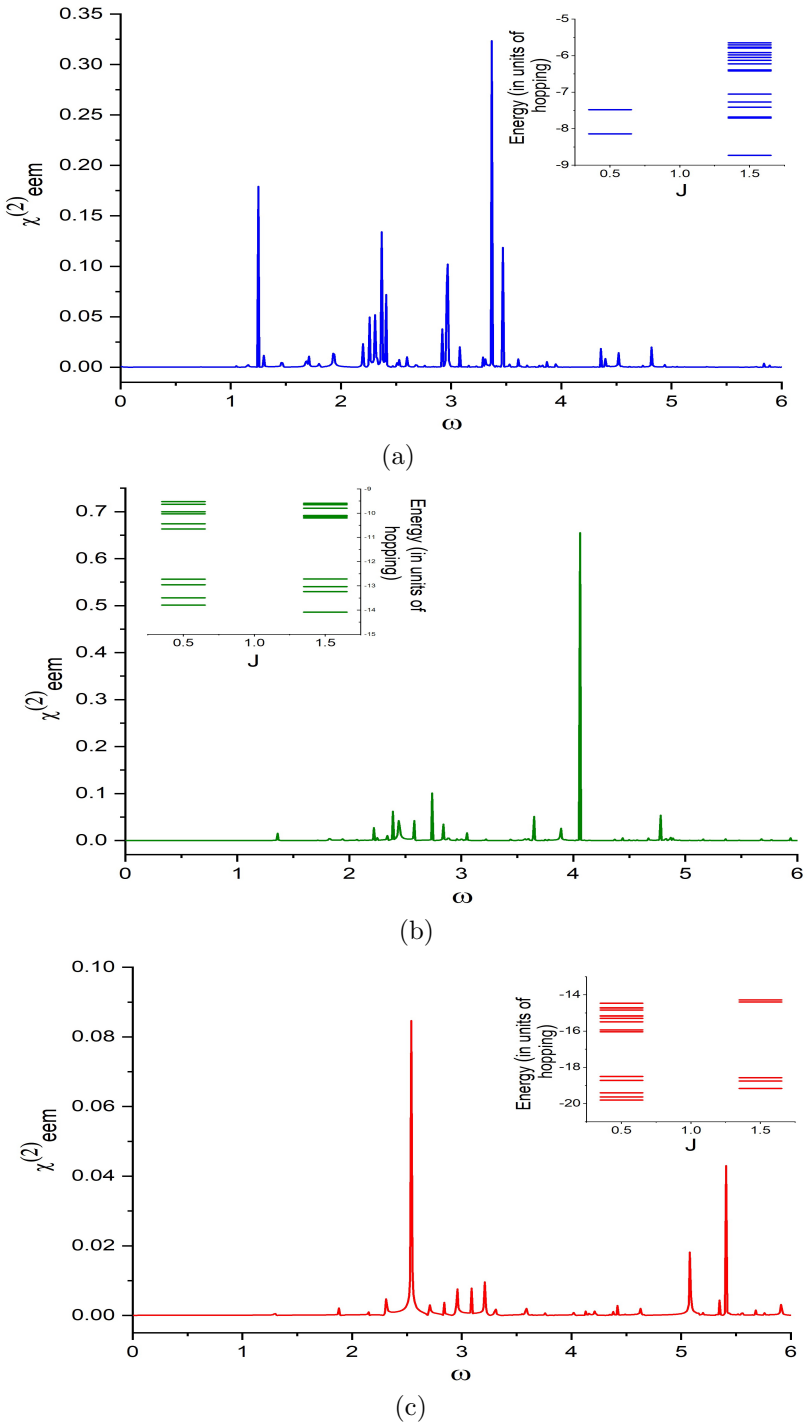


Figure 4.2: Plots of $\chi^{(2)}_{eem}$ vs $\omega$ (in units of $\hbar$ eV)for $U/t = 4.0$ and $\lambda/t = 2.0, 4.0$ and 6.0. The insets show plots of energy in eV vs total angular momentum quantum number J in each case. For $\lambda/t = 4.0$, there are equal number of states for both $J = 0.5$ and $J = 1.5$ and thus there are more degeneracies.

exchange than those due to change in orbital angular momentum. For $\lambda/t \simeq U/t$, the energies corresponding to both the excitations are similar, that is, the excited states are highly degenerate. This is obvious from Fig. 4.3, in which all of Fig.4.2 (a), (b) and (c) are superposed. There are some less or moderately intense peaks for $\lambda/t < U/t$ and $\lambda/t > U/t$ due to less degeneracy of the excited states. And, for $\lambda/t \simeq U/t$, there are less number of peaks, but a single peak with high amplitude corresponding to high degeneracy of the excited states. The insets of Fig.4.2(a),

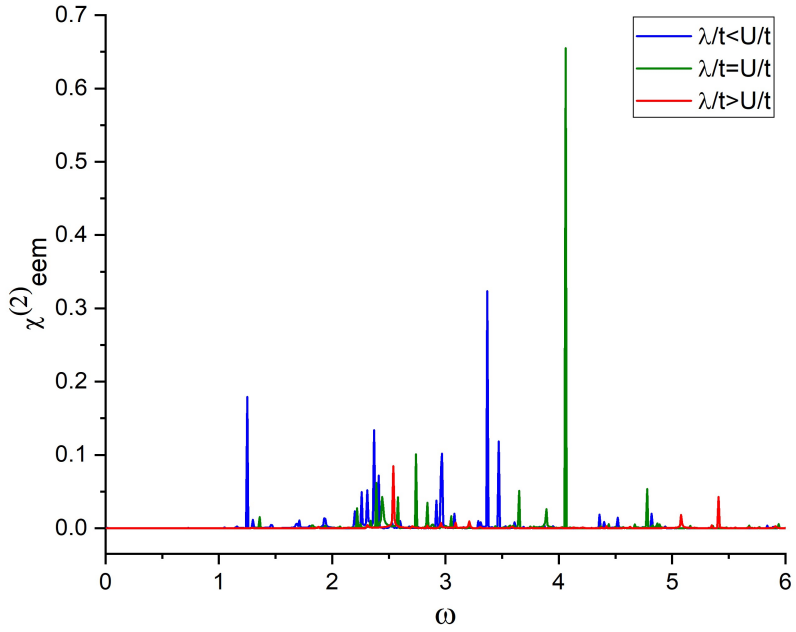


Figure 4.3: Combined plot of $\chi^{(2)}_{eem}$ vs $\omega$(in units of $\hbar eV$) for $U/t = 4.0$ and $\lambda/t = 2.0, 4.0$ and 6.0. For $\lambda = 2.0 and 4.0$, there are more number of less intense peaks. For $\lambda/t = U/t = 4.0$, there is a single peak with high amplitude due to high degeneracy of the excited states involving excitation corresponding to both exchange and orbital transitions.

(b) and (c) also verify the above result. Here we have plotted the energies of 20 lowest excited states as a function of total angular momentum $J$, computed from the expectation value of $\hat{J}^2$ operator($\langle \hat{J}^2 \rangle = \langle (\hat{L} + \hat{S})^2 \rangle$).It is evident from these insets that, for $\lambda/t < U/t$, the low-energy excited states will have higher $J$ values as the electrons prefer filling different angular momentum states rather than pairing up in one orbital, hence the density of states is high at $J = 1.5$. For $\lambda/t > U/t$ the,

exchange is preferred, hence the states with lower value of $J$ , namely $J = 0.5$ have more population of states. At $\lambda/t = U/t$, the excited states comprise excitations due to both exchange and spin-orbit coupling and hence there are almost equal number of states with total angular momentum values, $J = 0.5$ and $J = 1.5$.

The plots of $\chi^{(2)}_{eem}$ versus $\omega$ for five different values of $U/t$ for a fixed $\lambda/t = 0.8$ ,

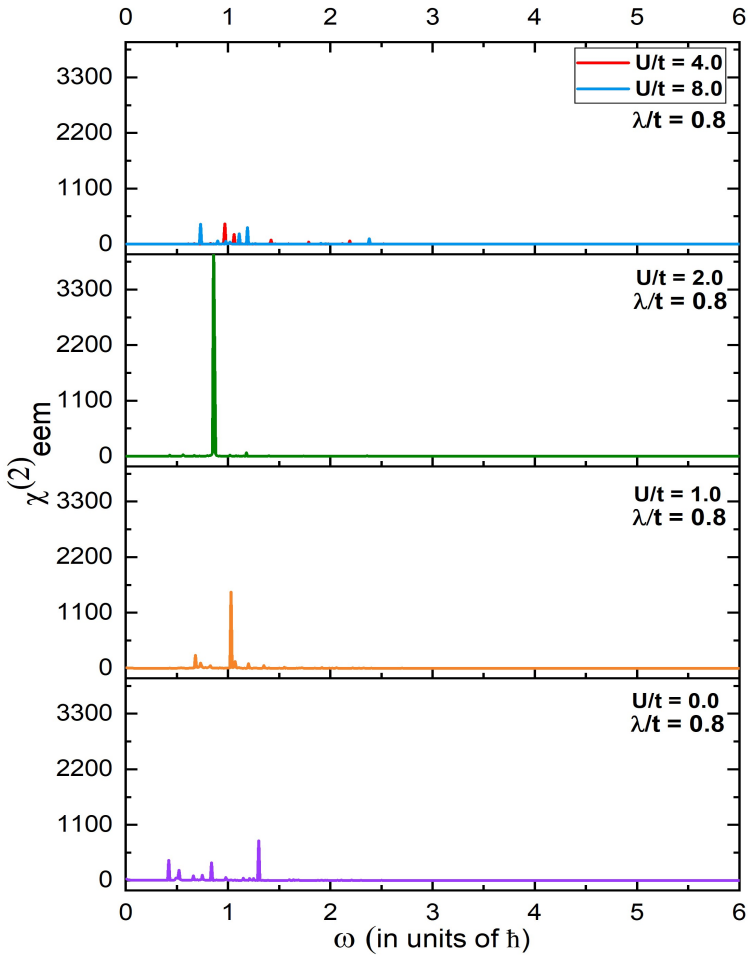


Figure 4.4: Plots of $\chi^{(2)}_{eem}$ vs. $\omega$ for different values of $U/t = 0.0, 1.0, 2.0, 4.0, 8.0$. For $U = 1.0$ and 2.0, the peaks have greater amplitude owing to similar excitation energies due to SOC and exchange.

are shown in Fig.4.4, The spin excitations cost energy $\approx \lambda$ and at most $3\lambda$, since there are 3 sites with SOC in our system. So we find a high amplitude peak in the regime $U/t = 0.8 - 2.4$ as excitations due to $U$ and $\lambda$ have similar energies, leading

to more degeneracies. For $U < \lambda$ and $U > 3\lambda$ the degeneracies are broken and so the amplitude of the peaks decrease. Also, for higher $U$ values, very few peaks are visible only at lower values of $\omega$, namely, those connecting states with similar $\langle U \rangle$. This is because, the spin excitations together can not match the excitations costing energy $U$ and so peaks at higher $\omega$ values are least probable.

From Fig. 4.4, it is also evident that there are non-zero ME susceptibilities at $U = 0$. In this regime, the model is effectively tight-binding with spin-orbit coupling. Though the electronic spins are completely delocalized in this case, there is no role of kinetic exchange. But the broken SU(2) symmetry in the presence of spin-orbit coupling leads to spin-orbital excitations between different eigenstates and hence it is sufficient to give nonzero $\chi^{(2)}_{eem}(\omega)$.

The effect of SU(2) symmetry breaking upon spin-phonon coupling[28–30] will be similar when we consider hardcore Bosons, owing to the equivalence of the two, as shown in Eqn.(4.10). But in reality, there are many bosonic modes, so one has to use Holstein-Primakoff transformations[31] to obtain $\hat{\boldsymbol{L}}$ operator from the bosonic operators and thus the Hamiltonian for spin-orbit coupling can also be used. In that case, there will be many eigenstates for $\hat{L}_z$. So, for low values of $\lambda$ there will be many possibilities for transitions among $l$ values giving rise to many more peaks.

## 4.5 Conclusion

In conclusion, we have shown that there can be non-zero second order dynamical ME susceptibility $\chi^{(2)}_{eem}(\omega)$ at certain resonant frequencies in a system when the spin SU(2) symmetry is broken by spin-orbit or spin-phonon coupling. These resonant frequencies correspond to the different spin and charge excitations in case of spin-orbit coupling. For spin-phonon coupling, these correspond to charge exci-

tations as well as excitations between different phonon modes. The amplitude of the peaks are very high when both the excitations are in similar energy range.

# References

[1] H. Greve, E. Woltermann, R. Jahns, S. Marauska, B. Wagner, R. Knöchel, M. Wuttig, and E. Quandt, App. Phys. Lett. **97**, 152503 (2010).

[2] T. Kosub, M. Kopte, R. Hühne, P. Appel, B. Shields, P. Maletinsky, R. Hübner, M. O. Liedke, J. Fassbender, O. G. Schmidt, et al., Nat. Comm. **8**, 13985 (2017).

[3] M. Bibes and A. Barthélémy, Nat. Mat. **7**, 425 (2008).

[4] P. K. Amiri, J. G. Alzate, X. Q. Cai, F. Ebrahimi, Q. Hu, K. Wong, C. Grèzes, H. Lee, G. Yu, X. Li, et al., IEEE Transactions on Magnetics **51**, 1 (2015).

[5] M. Fiebig, J. Phys. D **38**, R123 (2005).

[6] N. Hur, S. Park, P. A. Sharma, J. S. Ahn, S. Guha, and S.-W. Cheong, Nature **429**, 392 (2004).

[7] L. C. Chapon, P. G. Radaelli, G. R. Blake, S. Park, and S.-W. Cheong, Phys. Rev. Lett. **96**, 097601 (2006).

[8] M. Naka and S. Ishihara, Sci. Rep. **6**, 20781 (2016).

[9] H. Katsura, N. Nagaosa, and A. V. Balatsky, Phys. Rev. Lett. **95**, 057205 (2005).

[10] T. Kimura, T. Goto, H. Shintani, K. Ishizaka, T. Arima, and Y. Tokura, Nature **426**, 55 (2003).

[11] G. Lawes, A. B. Harris, T. Kimura, N. Rogado, R. J. Cava, A. Aharony, O. Entin-Wohlman, T. Yildirim, M. Kenzelmann, C. Broholm, et al., Phys. Rev. Lett. **95**, 087205 (2005).

[12] T. Moriya, J. App. Phys. **39**, 1042 (1968).

[13] T. Arima, J. Phys. Soc. Jap. **76**, 073702 (2007).

[14] C. Jia, S. Onoda, N. Nagaosa, and J. H. Han, Phys. Rev. B **74**, 224444 (2006).

[15] C. Jia, S. Onoda, N. Nagaosa, and J. H. Han, Phys. Rev. B **76**, 144424 (2007).

[16] Z. Gong, G.-B. Liu, H. Yu, D. Xiao, X. Cui, X. Xu, and W. Yao, Nature Communications **4**, 2053 (2013).

[17] G. Huang, Bevin Clark, D. R. Klein, D. MacNeill, E. Navarro-Moratalla, K. L. Seyler, N. Wilson, M. A. McGuire, D. H. Cobden, D. Xiao, W. Yao, et al., Nature Nanotechnology **13**, 544 (2018).

[18] C. Ederer and N. A. Spaldin, Current Opinion in Solid State and Materials Science **9**, 128 (2005).

[19] J. C. Wojdeł and J. Íñiguez, Phys. Rev. Lett. **103**, 267205 (2009).

[20] M. Mostovoy, A. Scaramucci, N. A. Spaldin, and K. T. Delaney, Phys. Rev. Lett. **105**, 087202 (2010).

[21] A. Lahiri and S. K. Pati, arXiv preprint arXiv:2010.06258 (2020).

[22] L. Landau, L. Pitaevskii, and E. Lifshitz, *Electrodynamics of Continuous Media* (1984).

[23] B. Orr and J. Ward, Mol. Phys. **20**, 513 (1971).

[24] R. Boyd, *Nonlinear Optics 3rd Edition* (Academic Press, 2008), ISBN 9780123694706.

[25] C. Lanczos, J. Res. Natl. Bur. Stand. B **45**, 255 (1950).

[26] A. Datta and S. K. Pati, J. Phys. Chem. A **108**, 9527 (2004).

[27] A. Datta and S. K. Pati, J. Chem. Phys. **118**, 8420 (2003).

[28] J. Hemberger, T. Rudolf, H.-A. Krug von Nidda, F. Mayr, A. Pimenov, V. Tsurkan, and A. Loidl, Phys. Rev. Lett. **97**, 087204 (2006).

[29] N. F. Hinsche, A. S. Ngankeu, K. Guilloy, S. K. Mahatha, A. Grubišić Čabo, M. Bianchi, M. Dendzik, C. E. Sanders, J. A. Miwa, H. Bana, et al., Phys. Rev. B **96**, 121402 (2017).

[30] A. Ahlawat, S. Satapathy, V. G. Sathe, R. J. Choudhary, and P. K. Gupta, Appl. Phys. Lett. **103**, 252902 (2013).

[31] T. Holstein and H. Primakoff, Phys. Rev. **58**, 1098 (1940).

# 5

# Quench dynamics of Extended Hubbard Model in presence of Adiabatic Phonons in a dipolar lattice

## 5.1 Introduction

Non-equilibrium quantum systems have gained a lot of attention in current research in condensed matter physics because of their unique properties, very different from equilibrium quantum systems, which we usually know and study in textbooks and literature. Although, there has been much development in non-equilibrium statistical mechanics, the non-equilibrium quantum theory poses a few challenges. Most of the quantum theories deal with equilibrium physical problems, and usual methods like quantum statistical mechanics and perturbation theory are not able to capture the essence of non-equilibrium quantum nature. However, in recent years, there has been a huge upsurge in the study of dipolar lattices in various dimensional Bosonic ultracold systems after the successful realization of dipolar Bose-Einstein-condensation (BEC) in a number of Rydberg atoms[1,2] and Lanthanides[3,4]. Due to the flexibility in controlling every parameter and tun-

ing the interactions between the dilute gases of neutral atoms through Feshbach resonance, these systems have been excellent models to mimic the quantum many-body systems out of equilibrium. Fermionic atomic species like $^{6}$Li and $^{40}$K and bosonic species like $^{173}$Yb and $^{87}$Sr have been cooled down to quantum degeneracy, and are used as perfect ingredients for such studies. Exotic phenomena like BEC-BCS crossover[5] in fermionic systems to Kosterlitz-Thouless transition in bosonic Luttinger liquids[6] have been observed in these systems. In fact, soon after, there has been increased experimental realization of the exotic ground state phases like superfluid, pair-superfluid, supersolid, pair-supersolid, density wave and phases involving quantum magnetism[7]. Long-range dipolar interactions have also been achieved[8], which has helped to probe and understand the ultrafast spin dynamics in many-body systems.

A variety of such exotic phases have also been predicted theoretically using perturbative and non-perturbative methods (exact solutions and computational methods). In this case, the latter gives more microscopic insight into studying the behaviour of such systems. There have been studies where the existence of many-body localization, Anderson localization, thermal and prethermal phases have been found theoretically in disordered dipolar lattices. The emergence of a variety of such phases and phase transitions are a result of the competition between weak and strong dipolar couplings, nearest neighbour and distant neighbor hoppings, three body interactions and various types of disorders.

To understand most of these properties, the Hubbard model has been used[9]. This model is the minimal model to capture the electronic correlation and gives rise to Mott insulator phase in one dimension at half-filling (number of electrons is same as the number of lattice sites). However, to understand the excitonic formation or charge density wave phases, the minimal model is the extended Hubbard model (EHM)[10,11]. This model predicts a Spin Density Wave (SDW), Charge Density Wave (CDW), as a competition between on-site and nearest-neighbour Coulomb

repulsion in half-filled one dimensional lattice systems. This model has been studied extensively analytically using renormalization group methods ('g-ology') as well as computational methods like Quantum Monte Carlo, Exact Diagonalization and Density matrix Renormalization group methods, thus predicting the existence of a novel Bond-Order Wave (BOW)[12,13] phase. In fact, extensive investigations have been carried out to understand the BOW phase transition.

Since we have used the extended Hubbard model in this chapter for further study, we are giving details of the phases and phase transitions which have been observed and predicted in this model.

## 5.2 The Extended Hubbard Model

The extended Hubbard model has been used to understand the mechanisms of spin and charge fluctuations in high-$T_c$ superconductors as well as unconventional superconductors. The Hamiltonian for the extended Hubbard model can be written as

$$\hat{\mathcal{H}}_{UV} = \sum_{\langle ij\rangle,\sigma} \left( t_{ij} c^{\dagger}_{i\sigma} c_{j\sigma} + h.c. \right) + U \sum_{i} n_{i\uparrow} n_{i\downarrow} + V \sum_{\langle ij\rangle} (n_i - 1)(n_j - 1) \tag{5.1}$$

where $\sigma$ is the index for the spin. $t_{ij}$ and $U$ are respectively the hopping and Hubbard U parameters. $V$ is the nearest-neighbour Coulomb repulsion. The operator $n_i = n_{i\uparrow} + n_{i\downarrow}$ is the number operator at each site. At half-filling, the competition between U and V gives rise to different phases: for $U < 2V$ the ground state is a Charge Density Wave (CDW) with alternating two electrons and zero electron occupancies (Fig. 5.1a). For $U > 2V$ the lowest energy state is in Spin Density Wave (SDW) phase with one electron per site with quasi long-range spin order in

a one-dimensional system. At $U \simeq 2V$, it has been pointed out by Nakamura[14] using Exact diagonalization studies and also shown in subsequent numerical studies[12,13] that there exists a Bond Order Wave (BOW) phase for lower values of $U$ and $V$, which is characterized by alternate strong and weak hopping energy. Thus, there are two phase transitions occurring here: one is an Ising like quantum phase transition from CDW to BOW and another is a Kosterlitz-Thouless transition from BOW to SDW, characterized by the closing of a spin-gap. The ground state phase diagram is given in Fig .5.1b.

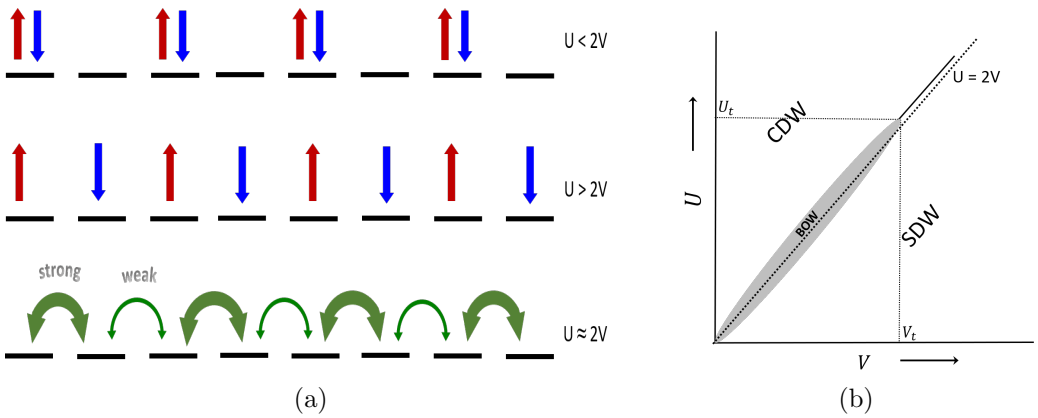


Figure 5.1: (a) Different phases of the Extended Hubbard Model, (b) Phase Diagram proposed by Nakamura.

In fact, it has also been shown that at less than half-filling, a long-range dipolar $V$ leads to singlet superfluid (SSF), triplet superfluid (TSF) and phase separation (PS) phases[15].

### 5.2.1 The SSH Term

The Su-Schrieffer-Heeger (SSH)[16,17] model has been well studied for describing the properties of molecular chains with conjugation, such as polyacetylene. It has been studied extensively as a simple model for describing topological excitations. Interestingly, if we remove the electron-electron interaction term, the Hamiltonian

produces an insulator state, called as Peierls state. However, in the presence of electron-electron interactions, it becomes unstable.[18–20]

In this chapter, we focus on the competition between electron-electron interactions and modulated hopping amplitudes due to SSH interactions.

We consider a lattice with $N$ sites at half-filling ($N$ electrons). We prepare an initial CDW state, which is given a sudden quench. The sudden quench is applied by evolving the initial CDW state with the use of UV-SSH Hamiltonian. The UV-SSH Hamiltonian is given by

$$\hat{\mathcal{H}} = \sum_{\langle ij\rangle,\sigma} -\left\{t + \alpha\left(u_i - u_{i+1}\right)\right\} c^{\dagger}_{i\sigma} c_{j\sigma} + h.c. + U\sum_i n_{i\uparrow} n_{i\downarrow} + V\sum_{\langle ij\rangle}\left(n_i - 1\right)\left(n_j - 1\right) + \frac{1}{2}K\sum_i \left(u_i - u_{i+1}\right)^2 \tag{5.2}$$

Here, the strength of hopping is proportional to the net displacement $(u_i - u_{i+1})$, $u_i$ being the displacement of the the $i^{\text{th}}$ atom. $\alpha$ is the hopping modulation parameter. $K$ is the force constant. Rewriting and adjusting the terms of the Hamiltonian, we obtain[21]

$$\hat{\mathcal{H}} = -t\sum_{\langle ij\rangle,\sigma}\left(1 + \delta_i\right) c^{\dagger}_{i\sigma} c_{j\sigma} + h.c. + U\sum_i n_{i\uparrow} n_{i\downarrow} + V\sum_{\langle ij\rangle}\left(n_i - 1\right)\left(n_j - 1\right) + \frac{1}{\pi\lambda}\sum_i \delta_i^2 \tag{5.3}$$

where, $\delta_i = \alpha\left(u_i - u_{i+1}\right)/t$ and $\lambda = 2\alpha^2/\pi K t^2$

### 5.2.2 Optimal Bond Order for every bond

We perform minimization subject to the constraint that total length of the chain remains constant, that is, $\sum_i \delta_i = 0$. Thus, minimizing the functional $F = H -$

$\eta \sum_i \delta_i$, we obtain an expression for the optimal bond order

$$\delta_i = \frac{\pi\lambda}{2}\left(\langle c^\dagger_{i,\sigma} c_{i+1,\sigma} + hc\rangle - \frac{1}{N}\sum_i \langle c^\dagger_{i,\sigma} c_{i+1,\sigma} + hc\rangle\right) \tag{5.4}$$

This optimal bond order for every bond has been calculated via self-consistent iterations.

## 5.3 Non-equilibrium Dynamics: Quantum Quench

The phases of the Hubbard model at equilibrium have been thoroughly studied for years. But the non-equilibrium dynamics give entirely new directions on such systems. After any external perturbation, the system, prepared at a certain initial state, undergoes unitary time evolution governed by the time-dependent Schrödinger equation, and can eventually achieve either of the following states: (i) it can thermalize, completely losing the memory of the initial state[22–24] (ii) in presence of disorder, it can achieve many-body localization, preserving the memory of the initial state at all times[25,26] (iii) if the system is close to integrability, or is periodically driven by some external agent, it can undergo prethermalization.[27]

Such non-equilibrium dynamics has been experimentally performed in a controlled way in lattices of ultracold atoms[28], as well as in strongly correlated electronic materials using pump-probe spectroscopy[29]. Such sophisticated experiments have been successful in probing a variety of phenomena like time-resolved transition from a superfluid to Mott insulator and strong to weak coupling crossover of paired Fermion superfluids.

The protocol of quantum quenching has gained popularity in recent years as it is a simple way to probe the non-equilibrium dynamics in many-body systems. We start with the eigenstate of a Hamiltonian $H_0$ at $t = 0$ and let it undergo unitary time evolution by suddenly adding a term or changing an interaction strength.

The system, which is no longer an eigenstate of the new Hamiltonian, will show energy conserved dynamics, which gives more insight into these systems.

A few works have been carried out on quench Dynamics of the EHM earlier by many others. Hofmann *et al.*[30] had studied the dynamics of a few doublons in an extended Hubbard chain with very low electron densities at the low-filling conditions. Kollath *et al.*[31] theoretically proposed an intriguing way to probe the Kosterlitz-Thouless transition from BOW to SDW, using time-dependent modulation of hopping, a method known as superlattice modulation spectroscopy. They showed that at the transition point, the energy absorption rate, characterized by the dynamic susceptibility, shows a peak, indicating the transition.

Pandey *et al.*[32] showed that quenching a CDW state by applying EH Hamiltonian along with disorder gives a number of phases, namely, thermal, Anderson localized and Many-body localized (MBL) phases. In fact, in the long time limit and considering averages over disorders, they have shown the formation of MBL phase involving both charge and spin degrees of freedom. In fact, taking a cue from the previous work, in this chapter, we focus on the quench dynamics of the extended Hubbard model in presence modulated hopping and classical harmonic potential.

### 5.3.1 Computational Method: Lanczos Time evolution

We have solved the time-dependent Schrödinger equation using the Lanczos time evolution method[33]. Starting from the initial CDW state at $\tau = 0$ $|\Psi_0\rangle$, we construct the Krylov space basis $K = \{|\Psi_0\rangle, \hat{H}|\Psi_0\rangle, \hat{H}^2|\Psi_0\rangle, \ldots, \hat{H}^K|\Psi_0\rangle\}$. In this truncated basis, we write the Hamiltonian $H_{Kr}$ and diagonalize it to obtain $H_D$.

$$\hat{H} = L\hat{H}_{Kr}L^{\dagger} \tag{5.5}$$

$$= \begin{bmatrix} \begin{pmatrix} \\ k_0 \\ \\ \end{pmatrix} & \begin{pmatrix} \\ k_1 \\ \\ \end{pmatrix} & \begin{pmatrix} \\ k_2 \\ \\ \end{pmatrix} & \dots \end{bmatrix} \begin{bmatrix} a_0 & b_0 & 0 & \dots & 0 \\ b_0 & a_1 & b_1 & \dots & \\ 0 & b_1 & a_2 & \dots & \\ \vdots & \vdots & & \ddots & \\ 0 & & & & \end{bmatrix} \begin{bmatrix} \begin{pmatrix} & k_0^{\dagger} & \end{pmatrix} \\ \begin{pmatrix} & k_1^{\dagger} & \end{pmatrix} \\ \begin{pmatrix} & k_2^{\dagger} & \end{pmatrix} \\ \vdots \end{bmatrix} \tag{5.6}$$

Here, the vector $k_0 = \Psi(0)$, $k_1 = \hat{H}\Psi(0)$, $k_2 = \hat{H}^2\Psi(0)$, etc.

Then the wave function at a later time $\tau$, i.e., $|\Psi(\tau)\rangle$ is obtained by exponentiating the diagonal matrix $H_D$ and performing two similarity transformations as follows

$$|\Psi(\tau)\rangle = e^{-iH\tau}|\Psi(0)\rangle = KUe^{-iH_D\tau}U^{\dagger}K^{\dagger}|\Psi(0)\rangle \tag{5.7}$$

We start from a doublon state. We quench the system with the UV-SSH Hamiltonian[18,19] at $U > 2V$. If it is quenched from a CDW state $(\uparrow\downarrow, 0, \uparrow\downarrow, 0, \uparrow\downarrow, 0, ...)$ the system begins to acquire SDW characteristic very quickly. Hence the double occupancy decreases within a very short time after quenching. More details follow in the results and discussion section below.

## 5.4 Results: Persistent Oscillations in the dynamics

### 5.4.1 Exact Diagonalization

We start with one-dimensional chain of a certain length in the CDW state. Initially the values of the model parameters are taken to be $t = -1.0$ and $U = 2V = 8$. We have performed unitary time evolution using the UV-SSH Hamiltonian (Eq.5.3). This was carried out for two different system lengths, namely, 10 and 12 sites lattice. The dynamics for a 12-site chain evolved up to a time of $800\frac{\hbar}{t}$ seconds ($2 \times 10^4$ steps with 0.04 change in each step) is shown in Fig. 5.2. Fig. 5.2a shows that for lower values of $\lambda$, the average double occupancy $\frac{1}{N}\sum_i n_{i\uparrow}n_{i\downarrow}$ decreases very quickly with time (shown in logarithmic time). Interestingly, for $\lambda = 1.0$, we find that this reduction in double occupancy is relatively slower and there is an oscillation at longer and longer times. The SSH Hamiltonian induces modulation in the bond order, which in turn induces the periodicity of the lattice. This is evident from the fact that the bond order parameter, defined as

$$\hat{B} = \frac{1}{N_{bonds}} \sum_{i=1}^{N_{bonds}} \sum_{\sigma} (-1)^i \langle c^{\dagger}_{i,\sigma} c_{i+1,\sigma} + \text{h.c.} \rangle \tag{5.8}$$

acquires a finite value at later times, as shown in Fig. 5.2b. Mathematically, it is the average staggered kinetic energy. The 3D plot in Fig. 5.3 shows the dynamics of the bond-orders of different bonds for a 12-site system. However, as can be seen, interestingly, there is a persistent oscillation in the dynamics of $\hat{B}$ for $\lambda = 1.0$, whereas for lower values of $\lambda$, the expectation values become stable within a short time. The bipartite charge fluctuation, calculated as the variance of the electron number operator for half the length of the chain, is a signature of many-body entanglement, which eventually leads to thermalization in the system.

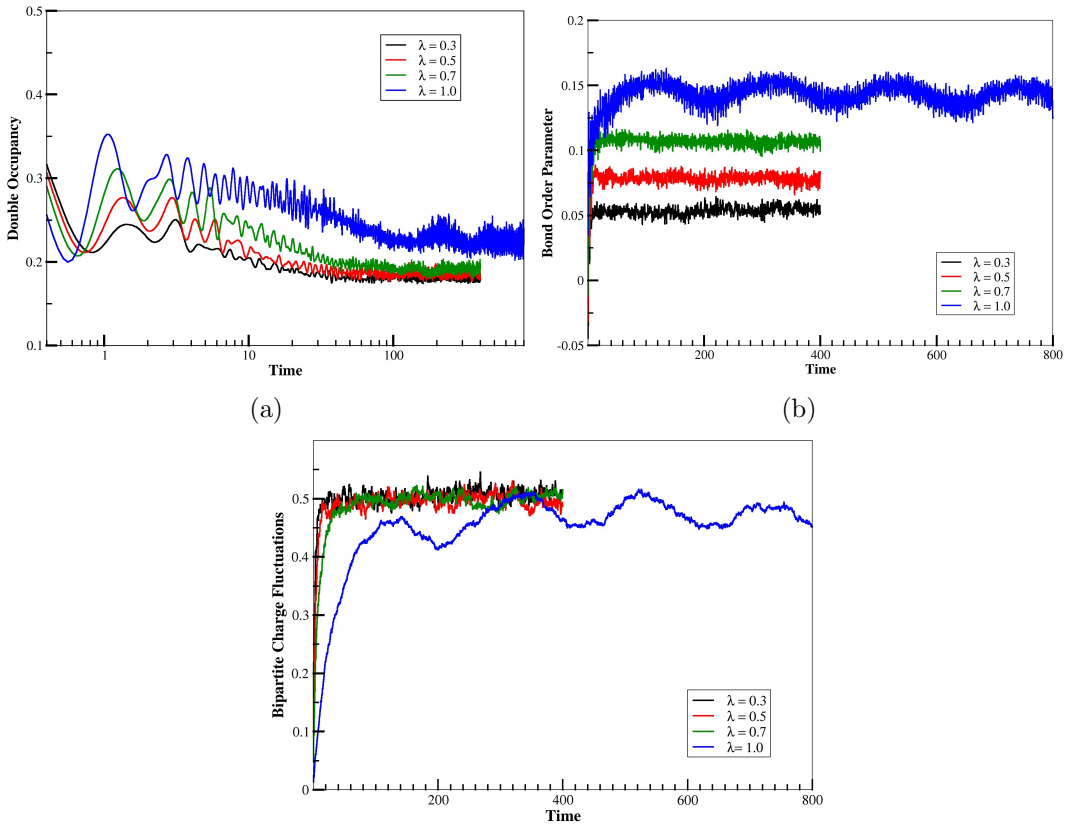


Figure 5.2: Time evolution of (a) the average double occupancy, (b) the bond-order parameter or staggered kinetic energy, and (c) the bipartite charge fluctuations for a 12-site chain with UV-SSH interactions for $U/t = 2V/t = 8.0$ and $\lambda/t = 0.3, 0.5, 0.7, 1.0$.

The expression is given by

$$F_c(t) = \left\langle \left( \sum_{i=1}^{L/2} n_i \right)^2 \right\rangle - \left( \left\langle \sum_{i=1}^{L/2} n_i \right\rangle \right)^2 \tag{5.9}$$

Fig. 5.2c shows that the bipartite charge fluctuation increases up to a certain time and becomes stable after a short duration for $\lambda = 0.3, 0.5$ and $0.7$. This indicates that, the initially prepared state starts losing some of the CDW characteristics, while singly occupied states are being formed. Once these states are formed to a certain extent, the system goes to a thermal state (actually quasi-thermal

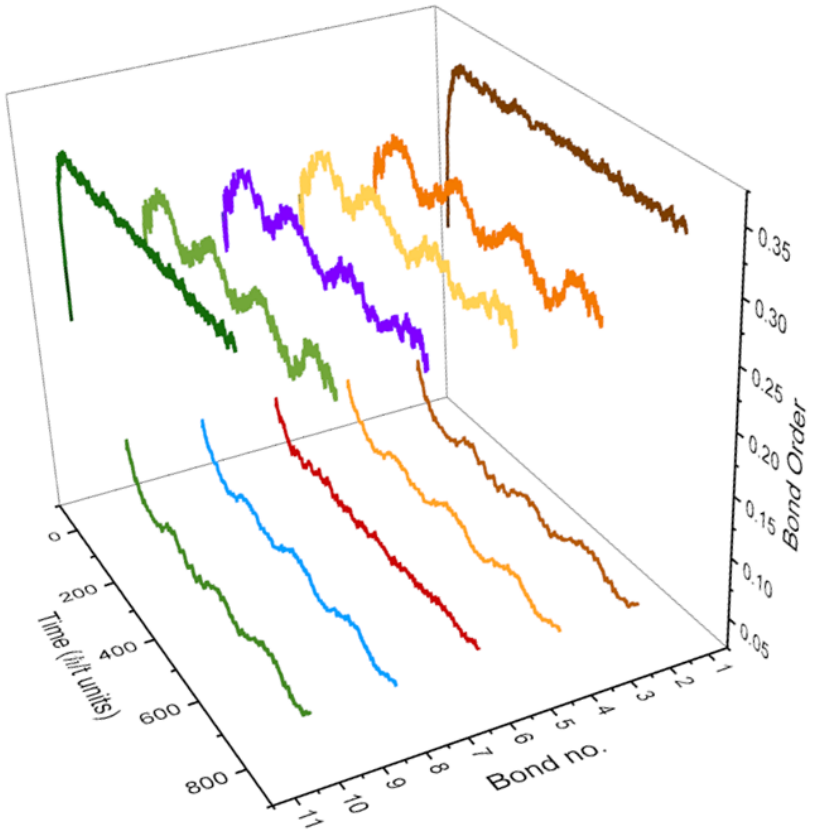


Figure 5.3: Time evolution of the bond-orders for all bonds for a 12-site chain at $\lambda = 1.0$.

for a finite size system). However, this thermal state still has contributions from the doubly occupied electronic states. In fact, average double occupancy becomes stable at a value of 0.2 ( see Fig. 5.2a).

However, for $\lambda = 1.0$, the bipartite charge fluctuation shows oscillations, which do not stabilize even at longer times. This is a clear indication of *prethermalization*. Interestingly, this prethermalized state persists only for $\lambda \simeq 1.0$. Even for higher value of $\lambda > 1.0$, such long time fluctuation is absent. This is evident from the plots of the average double occupancy, bond-order parameter and bipartite charge fluctuations (see Figs. 5.4a, 5.4b and 5.4c). Interestingly, the dynamics of all these quantities become stable after a short duration for $\lambda = 1.5$ and 2.0.

From the above results, one may think that the competition between the two

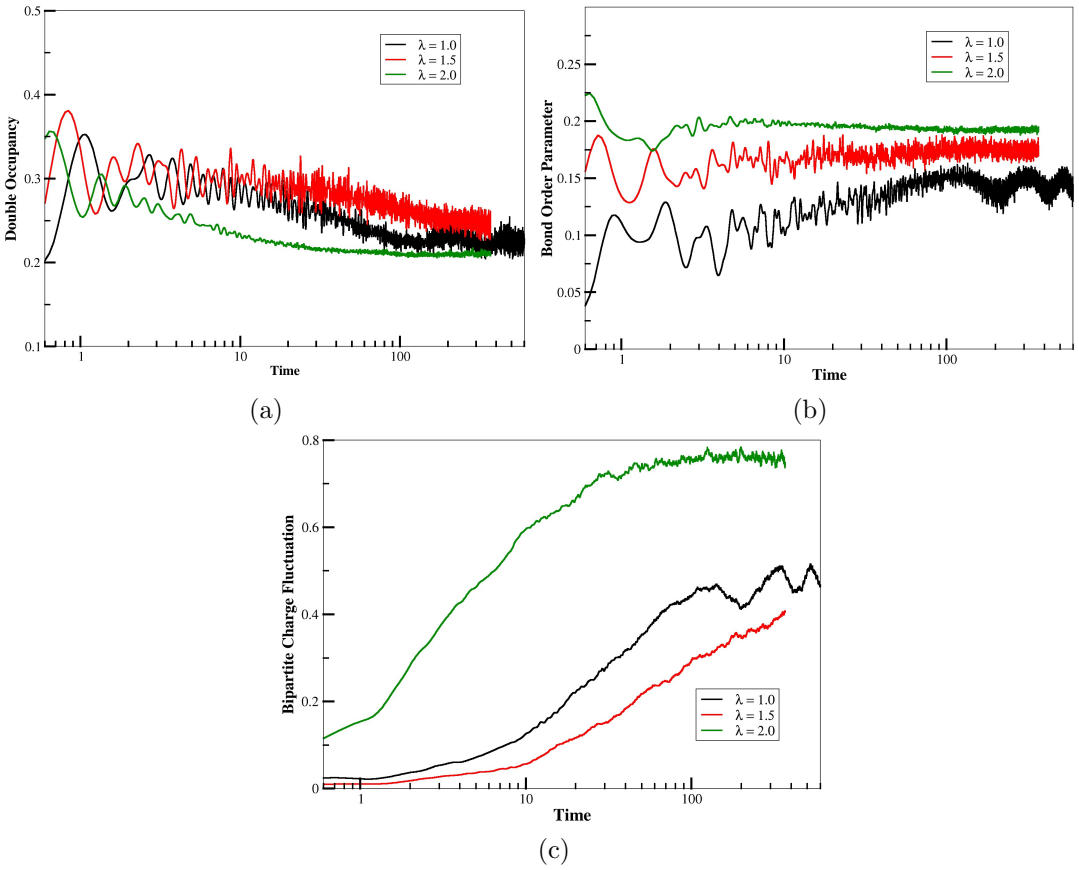


Figure 5.4: Time evolution of (a) the average double occupancy, (b) the bond-order parameter or staggered kinetic energy, and (c) the bipartite charge fluctuations of a 12-site UV-SSH chain for $U/t = 2V/t = 8.0$ and stronger electron-phonon strength $\lambda/t = 1.0, 1.5$ and 2.0.

key players, $t$ and $\lambda$, are responsible for such long time fluctuation dynamics. But this is not the case. The Hubbard-$U$ and the nearest neighbor Coulomb repulsion, $V$ also play a role here. To verify this and to obtain analytical information, we have carried out the computation of these dynamic quantities in two limits; (a) very small $U$ and $V$ values (close to zero) and (b) very large $U$ and $V$, to obtain either in tight binding limit or within frozen charge limit, respectively. However, we find that there is no long time fluctuation in any of these limits for these dynamical quantities. To quantify these claims, we plot below results of our long time dynamics of 12 sites lattice with parameter values $U = 2V = 12$ (high $U$ and

$V$)(Fig. 5.5a and 5.5b) and $U = 2V = 0.0, 1.0$ (no interaction as well as low $U$, $V$) (Fig. 5.5c,5.5d).

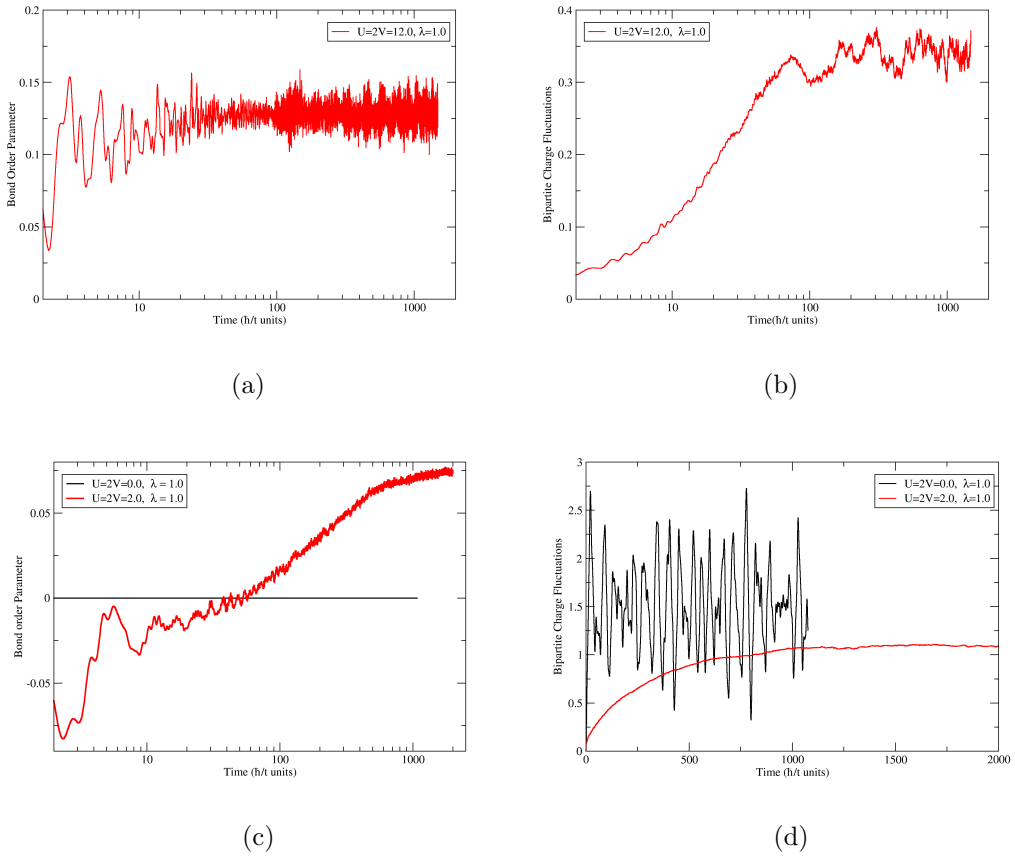


Figure 5.5: Lanczos time evolution of (a) bond-order parameter, and (b) bipartite charge fluctuations for a 12-site UV-SSH chain for $\lambda/t = 1.0$ and *strong* repulsion $U/t = 2V/t = 12.0$. And for $\lambda/t = 1.0$ and *weak* repulsion $U/t = 2V/t = 1.0$, time evolution of (c) the bond-order parameter and (d) bipartite charge fluctuations for a 12-site UV-SSH chain.

Figs. 5.6a and 5.6b show the dynamics of the bond order parameter and bipartite charge fluctuations for a fixed $\lambda = 1.0$ and $U = 2V = 4.0, 5.0$, and 8.0. For $U = 4.0$, the oscillations are absent for a 10-site chain, unlike that for the 12 sites chain, where the oscillations are prominent. However, here, small signatures of prethermalization are present for $U = 4.0$ and 5.0, where there are oscillations

in the bond-order parameter initially. But for 10 sites, these oscillations clearly die down and the system thermalizes at longer times. This is because the phase space (or the Hilbert space) is smaller compared to that of 12 sites and so the systems come into 'thermal' equilibrium sooner. Also, due to finite size effects, the oscillations are not as prominent as that of 12 sites.

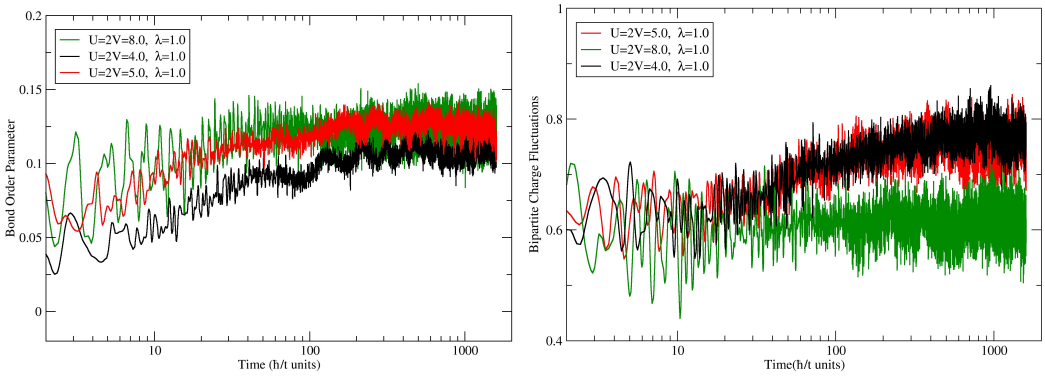


(a) (b)

Figure 5.6: Time evolution of (a) the bond-order parameter and (b) the bipartite charge fluctuations for a 10-site chain with UV-SSH interactions for $U/t = 2V/t = 8.0$ and $\lambda/t = 1.0$.

### 5.4.2 Comparing TEBD result with exact

We have developed the Time Evolving Block Decimation (TEBD) code (described in Chapter 2) in the Matrix Product State (MPS) formalism for simulation of large one dimensional chains. Initially, we have compared the exact results for 12 sites with those obtained using TEBD (Fig. 5.7). Within this procedure, we have used the $4^{th}$ order Trotter-Suzuki method, with time steps of $0.01\hbar/t$. We have kept the maximum bond dimension to 1000.

The long time dynamics of the double occupancy compares fairly well with the exact diagonalization results (Fig. 5.7a ). The bipartite charge fluctuations in Fig. 5.7b show deviation after some time steps. However, the oscillation is clearly visible from TEBD method also. The deviation is probably due to the fact that

the simulation is carried out for almost $40,000$ time steps and the time step is large compared to the accuracy limit of the $4^{th}$ order Trotter-Suzuki, which is $\mathcal{O}(t^5)$. Also, even though the system is in a prethermalized state, the entanglement is quite large and thus a larger bond dimension would be required to compare with the exact results. The bond-order parameter shows a larger deviation from the exact diagonalization results, as self-consistent steps are different in exact diagonalization and TEBD methods(Fig. 5.7c).

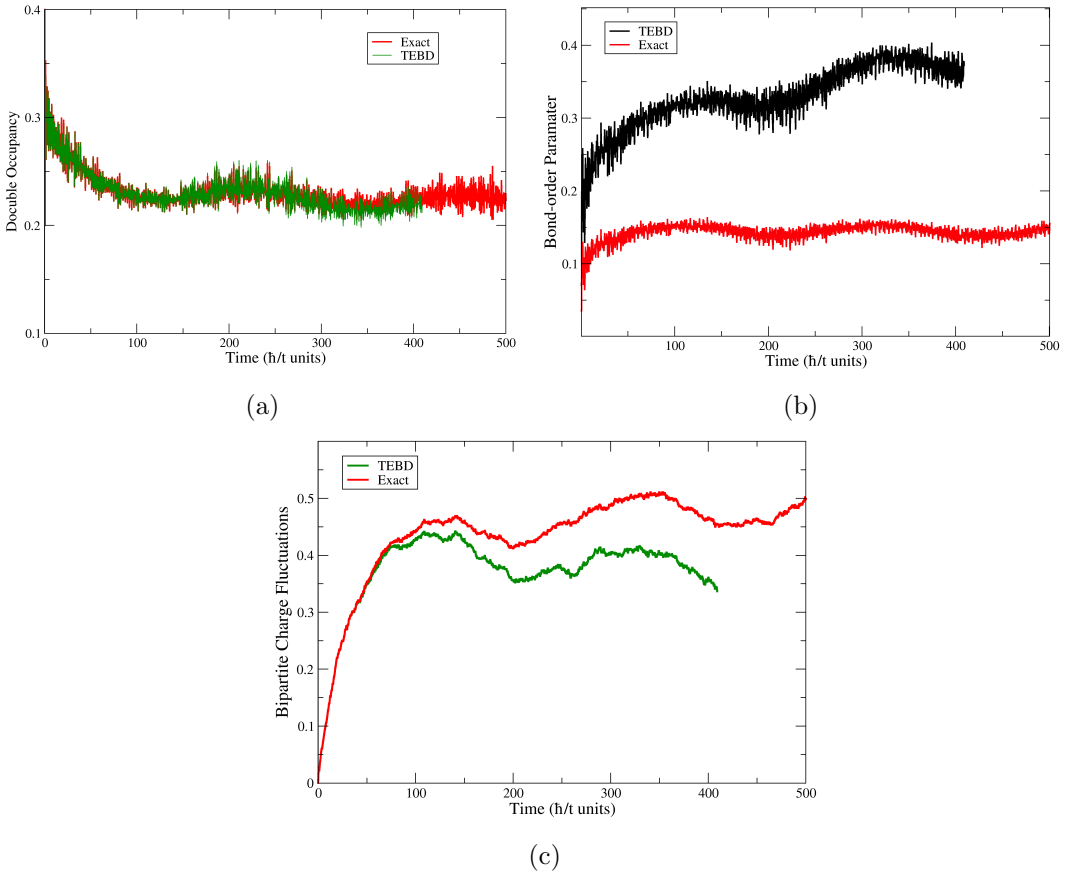


Figure 5.7: TEBD versus exact results of (a) the average double occupancy, (b) the bond-order parameter, and (c) the bipartite charge fluctuations for a 12-site UV-SSH chain for $U/t = 2V/t = 8.0$ and stronger electron-phonon strength $\lambda/t = 1.0$

## 5.5 Conclusion

In conclusion, we have studied the quench dynamics of the extended Hubbard model with SSH terms for a 1D chain starting from a CDW state. We find that the dissociation of doublons is slowed down and in addition, the system acquires BOW character. There are clear signatures of prethermalization for the phonon coupling strength, $\lambda = 1.0$ and for $U = 2V = 8.0$ for 12 sites lattice. For 10 site lattices, this prethermalized state is found at different values of $U$, $V$ and $\lambda$. Thus, there is size dependence in the occurrence of the prethermal state, which is the scope for further investigation. Also, the prethermalization occurs at moderate values of Coulomb repulsion parameters, preventing perturbative or analytical understandings.

# References

[1] Santos, L., Shlyapnikov, G. V., Zoller, P. and Lewenstein, M., Phys. Rev. Lett., **85**, 1791 (2000).

[2] Henkel, N., Nath, R., and Pohl, T., Phys. Rev. B., **104**, 195302 (2010).

[3] Lu, M., Burdick, N.Q., Youn, S.H. and Lev, B.L., Phys. Rev. Lett., **107**, 190401 (2011).

[4] Aikawa, K., Frisch, A., Mark, M., Baier, S., Rietzler, A., Grimm, R. and Ferlaino, F., Phys. Rev. Lett., **108**, 210401 (2012).

[5] Regal, C. A., Greiner, M., and Jin, D. S., Phys. Rev. Lett., **92**, 040403 (2004).

[6] Mathey, L., Günter, Kenneth J., Dalibard, Jean and Polkovnikov, A, Phys. Rev. A., **95**, 5 (2017).

[7] Weld, D. M. and Ketterle, W., J. Phys.: Conf. Ser., **264** 012017 (2011).

[8] C. Menotti,C., Lewenstein, M., Lahayed,T. and T. Pfaue AIP Conf. Proc., **970**, 332 (2008).

[9] Hubbard J. , Proc. R. Soc. Lond. A., **276**, 238 (1963).

[10] R. A. Bari, Phys. Rev. B., **3**, 2662 (1971).

[11] J. E. Hirsch, Phys. Rev. Lett., 53, 2327-2330 (1984).

[12] P. Sengupta, A.W. Sandvik and D.K. Campbell, Phys. Rev. B., **65**, 155113 (2002).

[13] Kumar, M., Ramasesha, S. and Soos, Z. G. Phys. Rev. B., **79**, 3, 224408 (2009).

[14] Nakamura, M., J. Phys. Soc. Jpn., **68**, 3123-3126 (1999) ; Phys. Rev. B **61**, 16 377 (2000).

[15] Mosadeq, H. and Asgari, R. Phys. Rev. B., **91**, 8, 214422 (2015).

[16] Su, W. P., Schrieffer, J. R. and Heeger, A. J., Phys. Rev. Lett., **42**, 1698 (1979).

[17] Fradkin E. and Hirsch, J. E., Phys. Rev. B., **27**, 1680 (1983).

[18] Kivelson, S., Su, W.P., Schrieffer, J.R. and Heeger, A.J., Phys. Rev. Lett., **58**, 1899 (1987).

[19] Grabowski, M., Hone, D. and Schrieffer, J.R., Phys. Rev. B., **31**, 12, 7850 (1984).

[20] Weber, M., Assaad, F.F. and Hohenadler, M., Phys. Rev. B., **91**, 245147 (2015).

[21] Lakshmi, S. and Pati, S. K., J. Chem. Phys.,**121**, 11998 (2004).

[22] Eckstein, M., Kollar, M. and Werner, P., Phys. Rev. Lett., **103**, 5, 056403 (2009).

[23] Sorg, S., Vidmar, L., Pollet, L. and Heidrich-Meisner, F. Phys. Rev. A., **90**, 3, 033606 (2014).

[24] Genway, S., Ho, A. F., and Lee, D. K. K, Phys. Rev. Lett., **105**, 26 (2010).

[25] Mondaini, R. and Rigol, M., Phys. Rev. A., **92**, 4, 041601 (2015).

[26] Bar Lev, Y., Reichman, D.R., and Sagi, Y., Phys. Rev. B., **94**, 20, 201116 (2016).

[27] Moeckel, M., and Kehrein, S., New J. Phys., **12**, 055016 (2010).

[28] Will, S., Iyer, D. and Rigol, M., Nat Commun., **6**, 7009 (2015).

[29] Chou, Y.Z., Liao, Y. and Foster, M. S. Phys. Rev. B., **95**, 10, 104507 (2017).

[30] Hofmann, F., and Potthoff, M., Phys. Rev. B., **85**, 20, 205127 (2012).

[31] Loida, K., Bernier, J., Citro, R., Orignac, E. and Kollath, C., Phys. Rev. Lett., **119**, 230403 (2017).

[32] Pandey, B., Dagotto, E. and Pati, S.K., arXiv:1905.06677.

[33] Lanczos, C., J. Res. Nat'l Bur. Std., **45**, 255–282 (1950).

# 6

# Finite temperature studies of alternating Spin-1/2-Spin-1 Chain using Minimally Entangled Typical Thermal states (METTS)

## 6.1 Introduction

Generally, the concept of temperature is not defined explicitly in quantum mechanics, as the quantum mechanical systems do not have Avogadro number of electrons or they are not in any ensemble. However, we can always assume that the system is in thermal equilibrium with some external bath, which gives an implicit notion of temperature. According to quantum statistical mechanics for a canonical ensemble, the thermal average of an observable is obtained as

$$\langle A \rangle = Tr\left[\rho A\right] = \frac{1}{\mathcal{Z}} Tr\left[e^{-\beta H} A\right] \tag{6.1}$$

Taking an orthonormal basis $|i\rangle$, if we expand the trace and then use the cyclic

property of the trace, we get

$$\begin{aligned}\langle A\rangle &= \frac{1}{\mathcal{Z}}\sum_i \langle i|e^{-\beta H/2}e^{-\beta H/2}A|i\rangle \\ &= \frac{1}{\mathcal{Z}}\sum_i \langle i|e^{-\beta H/2}Ae^{-\beta H/2}|i\rangle \\ &= \frac{1}{\mathcal{Z}}\sum_i \mathcal{P}_i\langle \Phi(i)|A|\Phi(i)\rangle \end{aligned} \tag{6.2}$$

where $|\Phi(i)\rangle = \frac{1}{\sqrt{\mathcal{P}_i}}e^{-\beta H/2}|i\rangle$ are a set of normalized basis states and the unnormalized probability distribution $\mathcal{P}_i = \langle i|e^{-\beta H}|i\rangle$.

Now from the statistical ensemble problem, we can write the similar equation for our quantum systems. In the quantum system, we can sample the $\{|\Phi(i)\rangle\}$ according to $\mathcal{P}_i/\mathcal{Z}$ and hence compute the thermal average of the required observables. However, to do that, we need to prepare these states properly.
Earlier, in 2005, Feiguin and White devised a way to directly obtain a finite temperature state by imaginary time evolution to an inverse temperature $\beta$, stating from a state at $\beta = 0.$ or the infinite temperature state. That is

$$|\Psi(\beta)\rangle = e^{-\beta H/2}|\Psi(\beta = 0)\rangle \tag{6.3}$$

To obtain this infinite temperature state in a spin-$\frac{1}{2}$ chain, for instance, we consider an auxiliary spin chain as the heat bath. at each site, we form a singlet ($\frac{1}{\sqrt{2}}(|\uparrow\downarrow\rangle - |\downarrow\uparrow\rangle)$) or a triplet ($\frac{1}{\sqrt{2}}(|\uparrow\downarrow\rangle + |\downarrow\uparrow\rangle)$) so the the information about the orientation of the spin is completely lost. Thus, if we trace out the auxilliary degrees of freedom from the density matrix of the state, the resulting reduced density matrix will represent a state in which, an up-spin and a down-spin will be equally probable at each site.
But, in a more efficient way, we can start from a pure state $|i\rangle$, obtain a state $|\Phi(i)\rangle$ by imaginary time evolution and thus perform a random walk over these

states to obtain the observables as statistical averages.

## 6.2 Minimally Entangled Typical Thermal States

One can choose an initial state $|i\rangle$ from any orthonormal basis. But, to minimize the computational cost, the best choice would be the individual configurations of the Fock Space, also referred to as the Classical Product States (CPS). These states have zero entanglement and the thermal states produced from these CPS would naturally have the minimal entanglement entropy, compared to being evolved from some other basis, thus making the algorithm more efficient. Threfore, these thermal states are called *Minimally Entangled Typical Thermal States*(METTS)[1,2].

The METTS $|\Phi(i)\rangle$ are referred to as 'typical' because the ensemble of these states can reconstruct the canonical distribution function

$$\sum_i \mathcal{P}_i |\Phi(i)\rangle\langle\Phi(i)| = e^{-\beta H} \tag{6.4}$$

Also, considering the way they are constructed, at high temperatures ($\beta \to 0$), $\mathcal{P}_i$ become 1 and thus we get a complete set of equally probable states, which basically is the CPS. At lower temperatures, they are superposed states which spontaneously break symmetries of the Hamiltonians, very similar to systems with frustration or distant neighbour couplings or long range dipolar interactions.

## 6.3 Imaginary Time Evolution

To generate the METTS $|\Phi(i)\rangle = \frac{1}{\sqrt{\mathcal{P}_i}} e^{-\beta H/2}|i\rangle$ at a finite temperature $\beta$, we perform evolution in imaginary time, $\beta = i\tau$. For smaller chains, time evolution methods, such as, $4^{th}$ order Runge Kutta Method (RK4) or Krylov[3] space method can be used. The former, which is a straight forward 4th order expansion method

and does not take into account the unitarity of the exponential time evolving term, is the most efficient method in this case. The unitarity is not an issue here, since the operator is real and we get time evolution accuracy to 4th order in imaginary time.

For larger chains, the imaginary time evolution can be performed using Matrix Product State time evolution methods, such as TEBD [4–8](discussed in Chaper 2). It is a fast and efficient method to obtain the METTS. Although, it works for systems with only nearest-neighbor interactions, swap gates [2] can always be used for additional couplings, like next or further neighbor couplings.
For better accuracy and efficient inclusion of longer range interactions, methods like MPO-W$^{\text{II}}$ [9] and Time Dependent Variational Principle (TDVP) [10,12] can be used.

## 6.4 Collapsing a METTS into CPS

As mentioned in the previous section, the expectation values of the desired observables are obtained by performing a random walk through the set of METTS. The METTS generated by imaginary time evolution of the CPS should be followed by collapsing it into another CPS for the next iteration.

### 6.4.1 Collapsing a METTS for spin-$\frac{1}{2}$

The METTS generated by imaginary time evolution of the CPS should be followed by collapsing it into another CPS for the next iteration. For instance, consider a spin-$\frac{1}{2}$ system and suppose we have obtained a METTS starting from a random single configuration. If one wants to collapse the z-component of spin of a METTS $|\Phi\rangle$ at the $i^{th}$ site, the probability of the spin to be $|\uparrow\rangle_i$ would be $p(\uparrow) = \frac{1}{2} + \langle S_i^z \rangle$, and the probability for the other spin configuration, $|\downarrow\rangle_i$ would be $p(\downarrow) = \frac{1}{2} - \langle S_i^z \rangle$.

Note that, this is done randomly for a single spin configuration. This can be generalized. For a spin to be $|\uparrow_n\rangle_i$ or $|\downarrow_n\rangle_i$ along the $n^{th}$ axis, the probabilities would be $p(\uparrow_n) = \frac{1}{2} + \hat{n}.\langle\vec{S}_i\rangle$ or $p(\downarrow_n) = \frac{1}{2} - \hat{n}.\langle\vec{S}_i\rangle$ respectively.

Similarly for a spin-1 site, there will be 3 possibilities: $|-1\rangle_i$, $|0\rangle_i$, $|-1\rangle_i$. In this case, the probabilities would be

$$\begin{aligned} p(\text{-1}) &= -\frac{1}{2}\hat{n}.\langle\vec{S}_i\rangle + \frac{1}{2}(\hat{n}.\langle\vec{S}_i\rangle)^2 \\ p(0) &= 1 - (\hat{n}.\langle\vec{S}_i\rangle)^2 \\ p(1) &= \frac{1}{2}\hat{n}.\langle\vec{S}_i\rangle + \frac{1}{2}(\hat{n}.\langle\vec{S}_i\rangle)^2 \end{aligned} \tag{6.5}$$

In fact, in similar manner, the generalization can be adopted for any spin-S.

### 6.4.2 Collapsing a METTS for a general system with $d$ degrees of freedom at each site

Suppose a Hilbert space for each site of a general systems (spin, fermionic, bosonic etc.) have dimension $d$ with basis states $\{|\tau\rangle_i\}$, $\tau = 1, ..., d_i$. We define the projection operator $\hat{P}_i(\tau) = |\tau\rangle_i\langle\tau|_i$. Then the probability of $i^{th}$ site to be in the state $|\tau\rangle_i$ would be $p(\tau) = \langle\Phi|\hat{P}_i(\tau)|\Phi\rangle$. Hence, the collapse at the $i^{th}$ site is done according to the projection

$$|\Phi\rangle \longrightarrow [p(\tau)]^{-1/2}\hat{P}_i(\tau)|\Phi\rangle \tag{6.6}$$

### 6.4.3 Choice of the CPS Basis

The basis for collapsing a METTS into a CPS should be wisely chosen, so that the ergodicity is ensured, i.e. for a spin Hamiltonian which commutes with $\hat{S}^Z$ (i.e. $\hat{S}^z$ conserved), the system should explore all of the $\hat{S}^z$ sectors in the thermal steps. Collapsing only along the $z$-axis at every thermal step is simpler to implement in

programs, but it would not achieve ergodicity.

A solution would be to take a maximally entangled basis with respect to $\hat{S}^z$ at each site. In that case, it would still be a product state, but the ergodicity would be achieved in a much fewer number of thermal steps.

For spin-$\frac{1}{2}$, such a basis is the $\hat{S}^x$ basis. The basis states of $\hat{S}^x$ are equal superposition of two z-component of spin-1/2, $|\uparrow\rangle$ and $|\downarrow\rangle$. Hence, the information about the spin at every site for the CPS in the previous step would be completely removed, thus minimizing the autocorrelation time. For spin-1 the maximally entangled basis is:

$$\begin{aligned}
|\tau_1\rangle &= -\frac{1}{\sqrt{3}}\left(e^{i2\pi/3}|1\rangle - |0\rangle - e^{-i2\pi/3}|\text{-}1\rangle\right) \\
|\tau_2\rangle &= -\frac{1}{\sqrt{3}}\left(|1\rangle - |0\rangle - |\text{-}1\rangle\right) \\
|\tau_3\rangle &= -\frac{1}{\sqrt{3}}\left(e^{-i2\pi/3}|1\rangle - |0\rangle - e^{i2\pi/3}|\text{-}1\rangle\right)
\end{aligned} \tag{6.7}$$

### 6.4.4 Algorithm

The algorithm for producing a METTS for a spin-$\frac{1}{2}$/spin-1 alternating chain and obtaining quantities at finite temperature is as follows:

1. Choose a CPS $|i\rangle$, or a single configuration.

2. Evolve $|i\rangle$ in imaginary time to obtain the METTS $e^{-\beta\mathcal{H}/2}|i\rangle$ and calculate the desired quantities.

3. Obtain a new CPS with the probability $P(i \to i') = \langle i'|\phi(i)\rangle$. In the case of an alternating spin-$\frac{1}{2}$/spin-1 chain, calculate the probablities of the spins at each site along the maximally entangled basis (Sec 6.4.3) and return to Step 2.

### 6.4.5 Parallelization

It is easy to parallelize the algorithm to obtain different points in the expectation values versus temperature plot, as the generation of METTS at different temperatures can be treated as independent random walks. Although, the Markovian random walk is a sequential process, i.e., the CPS for any iteration can only be obtained by collapsing a METTS obtained by the previous iteration. In recent years, there have been efforts to achieve parallelization with such random walks [11], which, if implemented, can improve the computational efficiency for calculating the finite temperature properties of large systems.

## 6.5 Results: METTS for an alternating spin-$\frac{1}{2}$-spin-1 chain

We have developed Python code for generating METTS to perform finite temperature calculations for the Heisenberg model of alternating spin-$\frac{1}{2}$/spin-1 one dimensional lattice. We have performed the calculations for 8 and 10 sites, to compare with the exact diagonalization results.

To test our METTS results, we have computed magnetic susceptibility as a function of temperature for two systems: (a) nearest neighbor coupling $J_1 = 1.0$ and next nearest neighbor coupling $J_2 = 0$ and (b) $J_1 = 1.0$ and $J_2 = 0.4$. The magnetic susceptibility can be written as the fluctuation of magnetization term as follows.

$$\chi = \frac{\overline{\left\langle \left(\sum_i \hat{S}_i^z\right)^2 \right\rangle} - \left(\overline{\left\langle \sum_i \hat{S}_i^z \right\rangle}\right)^2}{T} \tag{6.8}$$

The above quantities are calculated within METTS with averaging over 140 thermal steps for each temperature point. For imaginary time evolution, the TEBD method has been adopted involving $4^{\text{th}}$-order Trotter-Suzuki method with

imaginary time steps $\Delta\beta = 0.1J_1$. It has been shown by Pati *et al.*[13] for a spin-1-Spin-1/2 ferrimagnetic chain with nearest neighbor antiferromagnetic coupling that there occurs a minimum in the plot of the susceptibility multiplied by temperature $\chi T$ versus $T$ at $T = 0.5J/k_b$. This is due to the fact that in such a ferrimagnetic chain, the lowest excitation has a spin which is lesser than the ground state spin and the next higher state has spin which is higher than the ground state spin. The ground state appears in a spin state, which is the addition of spin in each dimer with number of dimers. For a $N$ sites system, the ground state is in $S^z_{tot} = N/4$, as each spin dimer contributes $S^z = 1/2$. The lowest excited state has a spin of $S^z_{tot} = N/4 - 1$, while next higher state has a spin of $S^z_{tot} = N/4 + 1$. This occurs as from the spin-wave theory, there are two excitation modes, while the lowest one is antiferromagnetic mode, the higher one is a ferromagnetic mode. In fact, due to such anomalous behavior, as the temperature is raised, the lowest excitation, which has lesser spin (magnetization) contributes to susceptibility, whose magnitude reduces. However, as the temperature is raised further, the spin excitation has higher magnetization value and the susceptibility rises as expected.

This anomalous behavior of susceptibility becomes more prominent, if one plots susceptibility multiplied by the temperature versus temperature. This way, the absolute magnitude of magnetization fluctuation can be obtained, as can be seen in the above equation for susceptibility.

We have carried out susceptibility calculations within METTS and compared the same obtained from exact diagonalization (with all spin states) method. As can be seen, the plot of susceptibility $\chi$ versus temperature $T$ obtained from METTS compare fairly well with the same from exact diagonalization (Fig. 6.1a, 6.1b) throughout the temperature range considered. However, when we compare the plot of $\chi T$ versus $T$ with the same from exact diagonaliation, we find that the graphs are qualitatively similar, except that the $\chi T$ minimum is slightly shifted

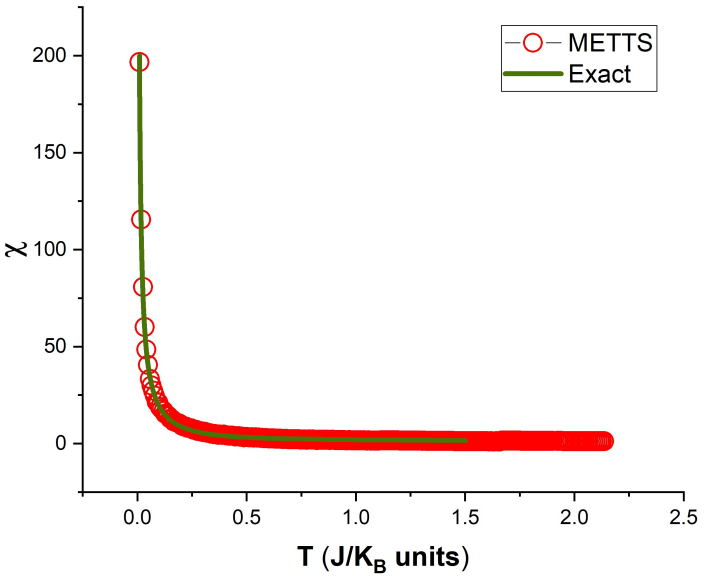


(a)

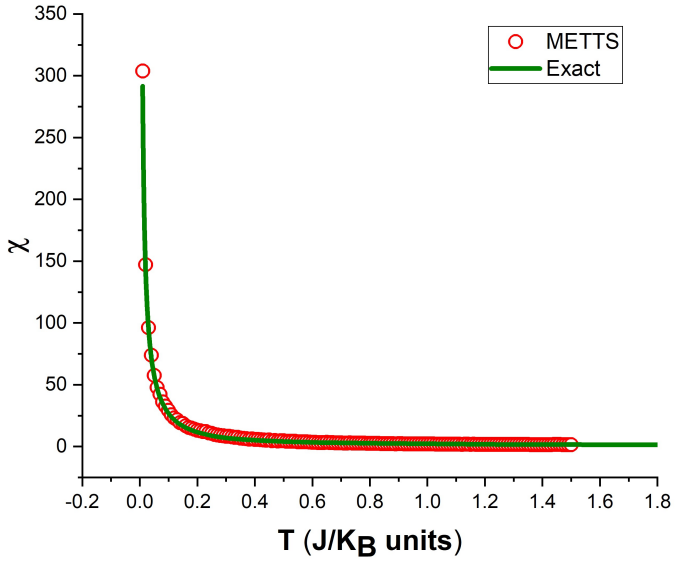


(b)

Figure 6.1: Plot of Susceptibility $\chi$ versus temperature $T$ for an alternating spin-$\frac{1}{2}$/spin-1 chain of length (a) 8 sites and (b) 10 sites with nearest-neighbor Heisenberg interaction using METTS and exact diagonalization

in case of METTS. This is due to the fact that statistical error is enhanced by multiplying $\chi$ with $T$.

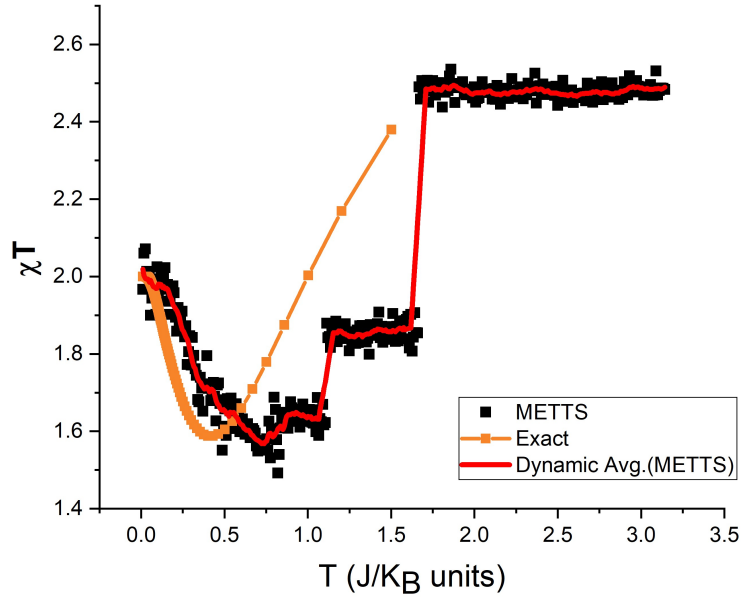


(a)

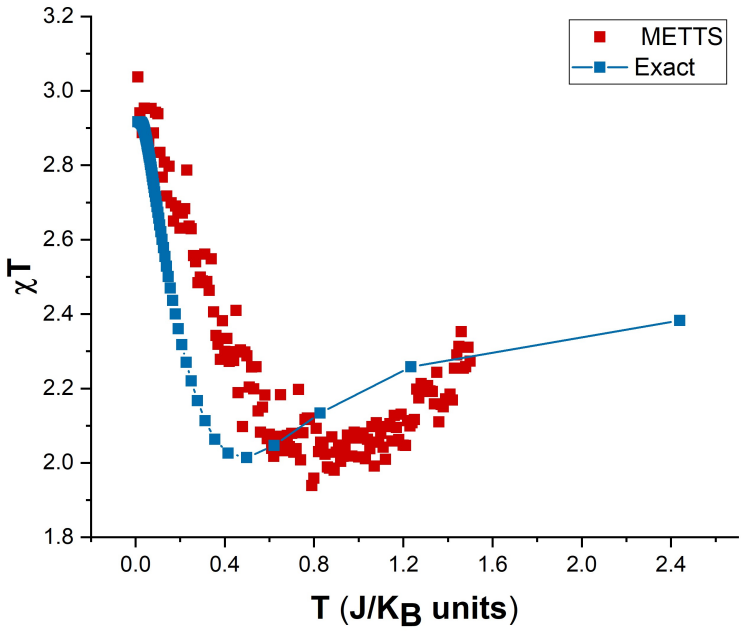


(b)

Figure 6.2: Plot of $\chi T$ vs. $T$ for an alternating spin-$\frac{1}{2}$/spin-1 chain of length (a) 8 sites and (b) 10 sites with nearest-neighbor interaction using METTS and exact diagonalization.

For next nearest neighbor frustration $J_2/J_1 = 0.4$, the plot of $\chi$ vs $T$ matches qualitatively with exact results (Fig.6.3).

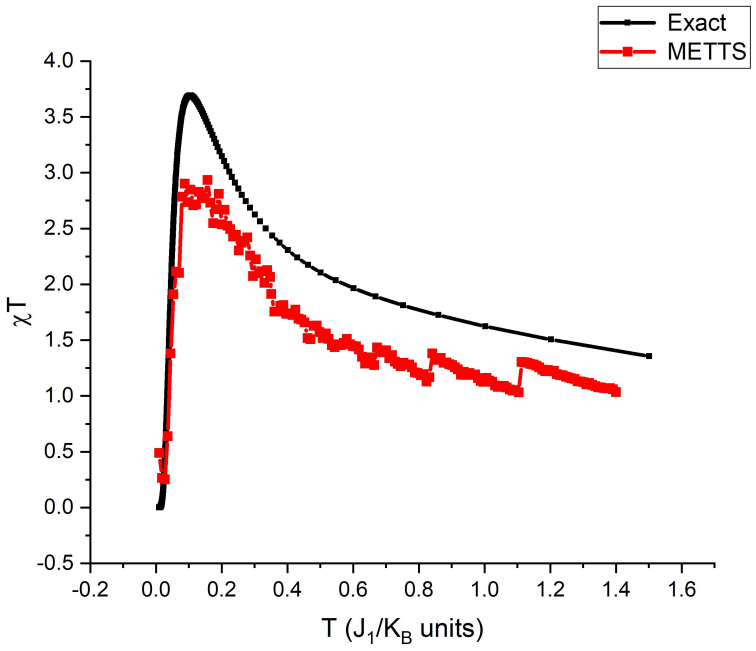


Figure 6.3: Plot of Susceptibility $\chi$ versus temperature $T$ for a 8-site long alternating spin-$\frac{1}{2}$/spin-1 chain with next-neighbor frustration $J_2/J_1 = 0.4$ using METTS and exact diagonalization.

## 6.6 Conclusion

To conclude, in this chapter, we have developed the Minimally Entangled Typical Thermal States for quantum spin models with two different spins in the dimer. We also have parallelized the code and it runs efficiently. As a test case, we have verified that the METTS code works well for ferrimagnetic systems and the signature of their characteristic magnetic properties has almost been quantitatively reproduced. Further works using this code is ongoing.

# References

[1] White, S. R, Phys. Rev. Lett., **102**, 190601, (2009).

[2] Stoudenmire, E.M. and White, S.R., New J. Phys., **12**, 055026, (2010).

[3] Lanczos, C., J. Res. Nat'l Bur. Std. **45**, 255–282 (1950).

[4] Vidal, G., Phys. Rev. Lett., **91**, 147902, (2003).

[5] G. Vidal, Phys. Rev. Lett., **93** 04050 (2004).

[6] Vidal, G., Phys. Rev. Lett., **98**, 7, 070201 (2007).

[7] Orús, R. and Vidal, G., Phys. Rev. B., **78**, 155117 (2008).

[8] White, S.R. and Feiguin, A.E., Phys. Rev. Lett., **93**, 076401 , (2004).

[9] Zaletel, M. P., Mong, R.S.K., Karrasch, C. Moore, J.E. and Pollmann, F., Phys. Rev. B **91** 165112 (2015).

[10] Daley, A.J., Kollath, C., Schollwöck, U., Vidal, G., J. Stat. Mech:Theory and Experiment, P04005 (2004).

[11] Calderhead, B. Proc. Natl. Acad. Sci. USA **111**, 17408–17413 (2014).

[12] Paeckel , S., Köhler, T., Swoboda, A., Manmana, S.R., Schollwöck, U., and Hubig, C., Ann. Phys., **411**, 167998 (2019).

[13] Pati, S. K. , Ramasesha, S. and Sen, D., Phys. Rev. B **55**, 8894 (1997).

# 7

# Summary and Outlook

CHAPTER 2:

In this chapter, I have elaborated the Matrix Product State (MPS) formalism and how it can be represented using tensor network schematic diagrams. Step by step, I have described how to construct MPS, their normalization, calculation of expectation values and correlations. DMRG is a variational energy minimization procedure in the light of the MPS. I have described the DMRG algorithm and necessary schematics to support that. Finally, I have described the TEBD method, which is a fast and efficient algorithm to obtain real and imaginary time dependent properties of the 1-dimensional quantum many-body systems with nearest neighbor interactions. I have developed the DMRG and TEBD algorithms for bosonic and fermionic systems in both Python and Julia. I have also used the TenPy package with is an open source MPS package in Python. The scope of future work is to implement these methods for dissipative bosonic as well as fermionic chains to study the dynamics of their decoherence in the presence of heat baths.

CHAPTER 3:

In this chapter, I have studied the ground state properties of an alternating spin-$\frac{1}{2}$/spin-1 Heisenberg chain with nearest-neighbor antiferromagnetic interaction and

next-nearest neighbor frustration along with z-component of the Dzyaloshinskii-Moriya (DM) interaction ($D^z$). In the first part, I have given a detailed derivation of the Linear Spin Wave Theory (LSWT) analysis. It has been shown earlier, that, with only nearest-neighbor interactions, the ferrimagnetic configuration is a stable one preserving the magnetization of each dimer, despite quantum fluctuations. But this state is unstable when the DM interaction $D^z$ is present, as evident from the negative energies in the dispersion relation and thus LSWT fails. The magnetization and correlation functions calculated from LSWT are also also inconclusive about the ordering of the spins. In contrast, the Density Matrix Renormalization Group (DMRG), being a non-perturbative computational technique, captures this instability well. We have shown that even a small strength of the DM interaction introduces strong quantum fluctuations and make the spin at each site as well as the whole chain zero. Also a long range order is developed in the XY-plane, as seen from the correlation functions. Next-nearest neighbor frustration also destroys the ferrimagnetic order but introduces a spiral order, as seen from the structure factor. Both next-nearest neighbor interaction and $D^z$ destroy this spiral order, and also any kind of short range order.

Investigating how stable the classical ferrimagnetic state is, in 2-dimensional lattices (square, triangular, kagome, etc.) in presence of the above interactions can be a direction towards further work.

CHAPTER 4:

In this chapter, we have investigated the origin of dynamical second order magnetoelectric (ME) susceptibilities in quantum many-body systems with broken SU(2) symmetry in the form of spin-orbit coupling (SOC) or spin-phonon coupling (SPC). We have carried out the calculations with 6 fermionic lattice sites, with alternate 3 of the sites which have L=$\frac{1}{2}$. Such lattices can be formed in dipolar optical systems with variation of a few laser beams with varying widths and

depths. Computationally, we have performed an exact diagonalization and calculated the ME susceptibilities with 200 lowest energy eigenstates obtained by the Lanczos algorithm. The variation of Hubbard term and spin-orbit coupling terms has been analyzed. While the former localizes the charges, the latter delocalizes the spin. Few low intensity peaks of ME susceptibility at some values of frequency have been observed for both large U and large SOC values, due to resonances in states with majorly spin and charge degrees of freedom. We also found that due to resonance in both the spin and charge, high intensity ME peaks (corresponding to both electric and magnetic field induced resonances) appear when the Hubbard term and the SOC (SPC) term become almost similar in strengths.

CHAPTER 5:

In this chapter we have performed quench dynamics of a Charge Density Wave (CDW) state with an Extended Hubbard Hamiltonian with Su-Schrieffer-Heeger term (UV-SSH model). We have considered the Hubbard $U$ and the nearest neighbor Coulomb repulsion $V$ to be of similar strength. Using the Krylov subspace based time evolution method, we have studied the long-time dynamics. We found that that the modulation in hopping introduces Bond-Order Wave (BOW) characteristics in the system, as evident from the increase of the bond-order-parameter (or staggered kinetic energy expectation value). Interestingly, we observed that, for a 12-site fermionic chain with parameters $U/t = 2V/t = 8.0$ and SSH coupling strength $\lambda/t = 1.0$, oscillations of the bond order starts after a long time, which is an indication of prethermalization. The dynamics of the bipartite charge fluctuations also shows such oscillations. Though these oscillations are present for 12 sites, they are absent for a 10-site chain for the same value of $U$ and $V$. This means they will occur for a different value of $U$ and $V$ for the same chain. Thus the onsite as well as nearest neighbor interactions also play a role here.

These observations pose a lot of questions here:

1. Why do these oscillations occur at longer times? Does the system become nearly integrable at some limit of $U$, $V$ and $\lambda$ ?

2. Do these oscillations occur in the thermodynamic limit ?

To answer these questions, further analysis and computation for larger chains is needed, which is the scope for further investigation.

CHAPTER 6:

In the Chapter 6, I have developed the Minimally Entangled Typical Thermal States (METTS) algorithm to calculate the finite temperature properties of quantum mechanical systems. In this method, we have generated the METTS by imaginary time evolution using the TEBD algorithm and performed a random walk on these METTS to calculate the thermal averages of physical quantities. we have tested our code to calculate the magnetic susceptibilities at different temperatures for an alternating spin-$\frac{1}{2}$-spin-1 with nearest-neighbor as well next-nearest-neighbor antiferromagnetic interactions. We have found that the susceptibilities were a good match quantitatively with that obtained from exact diagonalization, for nearest-neighbor interactions while there was a qualitative match in case of next-nearest neighbor frustration.

Implementation of this method to understand the finite temperature properties of larger quantum chains is our plan for future work.

# A Brief Outline of Other Works

In the course of my PhD, I have carried out a variety of works using the computational quantum many-body methods mentioned in the previous chapters. I am briefly mentioning a few of them below.

## Time scale of the superexchange mechanism

The Kramers-Anderson superexchange is a mechanism by which two magnetic transition metal cations containing unpaired electrons in their $d$-orbitals can exchange their spins by coupling through a filled $p$-orbital of a non-magnetic anion in between the two magnetic ions. To understand the time scale and also the mechanism of superexcahnge, we have set up a simple model of 3 sites and 4 electrons governed by the Hubbard Hamiltonian. The middle site represents the non-magnetic $p$-orbital and the two sites on each side represent the magnetic cations. The middle site was given a large negative on-site energy to ensure that the non-magnetic anion is always doubly occupied. After the development of the Lanczos time evolution method, we have performed the long-time simulations of this model. We found that, the expectation value of the double occupancy remains the same as the initial value with small fluctuations(Fig. 7.1a). This reveals that

effectively there is no electron transfer, as most of the antiferromagnetic systems are charge insulators. However, the spin densities of the left and the right sites (Fig. 7.1b) show large sustained oscillations from $\langle S^z \rangle = 0.5$ to $\langle S^z \rangle = -0.5$ and vice-versa. In the x-axis, the time scale is given and it appears that the magnetic exchange is quite fast. Thus, macroscopically, it seems that the electron on one d-orbital exchanges the spin density of the electron in the other d-orbital through filled p-orbital, electron density of which does not get affected. This also proves that since the electrons are indistinguishable, they virtually exchange their spins through the filled p-orbital and so the magnetic exchange energy appears in 2nd order degenerate perturbation theory, which is too small compared to the hopping amplitude or the on-site Coulomb interaction term.

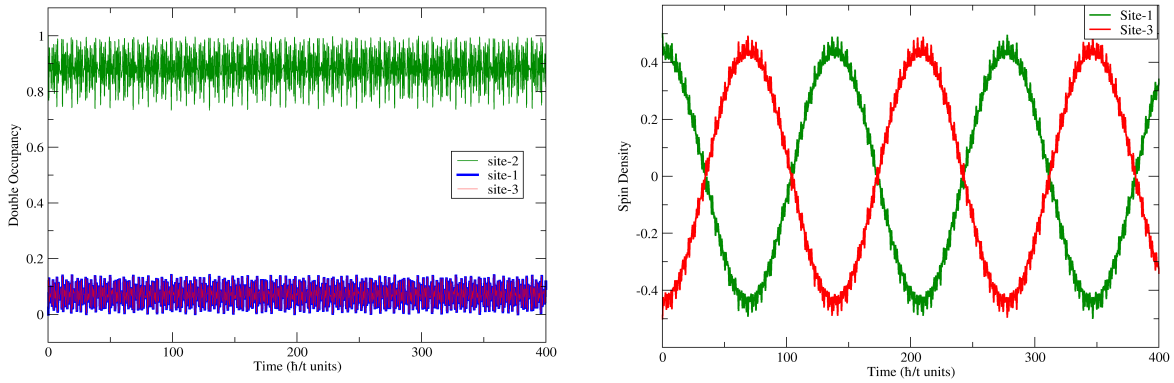


(a) (b)

Figure 7.1: Time evolution of (a) double occupancies of the sites, and (b) Spin densities of sites 1 and 3 for U/t = 5.0

## Dissipative Dynamics of Alternating spin-$\frac{1}{2}$/spin-1 Chain: Reversal of Magnetization

It has been observed experimentally that, in certain ferrimagnets, magnetization reversal occurs when cooled to lower temperatures in the presence of an external field. To understand the underlying mechanism, we have considered an alternating spin-$\frac{1}{2}$/spin-1 chain with nearest-neighbor Heisenberg interactions, and studied the dissipative dynamics of this chain. Assuming that there is a weak interaction between the chain and some external bath, we have considered the Gorini–Kossakowski–Sudarshan–Lindblad (GKSL) equation, given by

$$\frac{d\rho}{dt} = -\frac{i}{\hbar}\left[\hat{H}, \rho\right] + \gamma \sum_i \left( L_i \rho L_i^\dagger + \frac{1}{2}\left\{ L_i^\dagger L_i, \rho \right\} \right)$$

We have studied the dynamics of a chain of length 10 sites, with two Lindblad dissipators at the ends of the chain $L_1 = (S^-)_{\frac{1}{2}}$ for the spin-$\frac{1}{2}$ site and $L_2 = (S^-)_1$ for the spin-1 site.

In Chapter 3 and 5 of this thesis, we have studied the same model (with additional interaction terms). However, this model has a ground state spin, which is classical and has ferrimagnetic ordering with each dimer having total spin $\frac{1}{2}$.

We have considered an initial state in which the spin-1 site has z-component $S^z = 1.0$ and the spin-$\frac{1}{2}$ site has $S^z = -0.5$. So the total spin of the dimer, initially, is $S^z_{dimer} = 0.5$. In Fig. 7.2a, the spin densities or the expectation values ($\langle S^z \rangle$) have been plotted with time for sites 1, 2, 3 and 4 (note that, the 1$^{\text{st}}$ site is a spin-1 site). We find that the spin densities for sites 1 and 3 decrease from 1.0 to about $-0.4$ and those for sites 2 and 4 increase from $-0.5$ to about $-0.1$. Interestingly, the spin densities of the dimers, 1-2 and 3-4 (Fig. 7.2b) change from the initial value 0.5 to a stable final value of $-0.5$. This shows a clear signature of reversal of sign of the dimer magnetization. So, the system reverses the direction

of ferrimagnetic ordering with time.

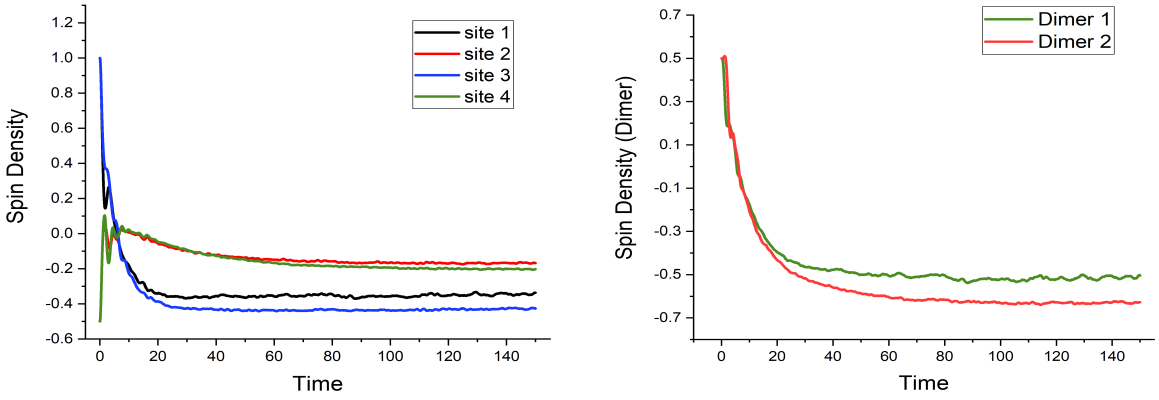


(a) (b)

Figure 7.2: Lindblad evolution of (a) the spin densities of sites 1, 2, 3 and 4 and (b) the spin densities of the 1st and 2nd dimers for an alternating spin-$\frac{1}{2}$/spin-1 chain

Currently we are trying to understand the reason behind this observation, and also we are developing codes to incorporate the Lindblad equation in the Matrix Product State formalism using Matrix Product Density Operators (MPDOs) and study these systems in a large system size limit with more complex Hamiltonians.

## Thermalization of the one dimensional Nagaoka Ferromagnet

We have studied the dynamics of the Nagaoka ferromagnet in one dimension. Although the Nagaoka's theorem states that a system with $N$ sites and $N-1$ electrons in 2 or more dimensions and in infinite Hubbard energy limit, the ground state is a single ferromagnetic configuration. It was shown by Hal Tasaki that, in one dimension also, the ground state is a superposition of all ferromagnetic configurations, suggesting that it is a ferromagnet.

We have started from a single random configuration of a 1 dimensional chain of 12 sites and 11 electrons and have studied the thermalization of this state with time governed by the Hubbard Hamiltonian.